ANALYSIS OF THE STUDY OF MATERIAL BEHAVIOR AT IMPACT RATES OF STRAIN

By

Oishik Sen

A THESIS

Submitted to
Michigan State University
in partial fulfillment of the requirements
for the degree of

MASTER OF SCIENCE

Mechanical Engineering

2010

ABSTRACT

ANALYSIS OF THE STUDY OF MATERIAL BEHAVIOR
AT IMPACT RATES OF STRAIN

By

Oishik Sen

Despite the practice of using cylindrical specimens in a Split-Hopkinson Pressure Bar experiment, the use of non-cylindrical prismatic specimens is convenient when testing extra-soft materials. A part of the current research aims to show the feasibility of using non-cylindrical specimens in a Kolsky Bar. For this, experiments were conducted with different model cross-sections at a nearly constant strain-rate in the Split Hopkinson Pressure Bar. The findings suggest the use of a suitable characteristic cross-section dimension of the specimen to determine the critical slenderness ratio while selecting a non-cylindrical prismatic specimen. The second part of the investigation aims to use the SHPB to find out the strength of an adhesive-bonded single lap joint. The current research focuses on extending existing models to predict the strength of adhesive joints by introducing a term for strain acceleration, in order to explain the drastic effect of overlap area of the joints on the dynamic strength of joints. Reasonably good agreement was found between the experiments and the mathematical predictions at moderately high loading rates. The third part of the research comprises of developing a Split-Hopkinson Tension Bar. The design proposed here comprises of an incidence bar which is 10 feet in length. An end of the incidence bar is coupled to a flange, whose diameter is greater than diameter than the incidence bar. An annular projectile is allowed to impinge on the flange, thereby generating a tensile pulse in the incidence bar. With this, the dynamic stress-strain properties of Copper were obtained.

Acknowledgements

The author would like to express his sincere gratitude to Dr. Srinivasan Arjun Tekalur for his constant patience, guidance, support and suggestions in course of the research work and for introducing the author to the beautiful experimental technique of the Split Hopkinson Pressure Bar. Had it not been for his encouragement and enthusiasm and regular supervision, even a fraction of the current work would not have been achieved.

The author expresses his gratitude to Dr. Gary Cloud, Michigan State University, Dr. Arun Shukla, University of Rhode Island, Dr. M.J. Forrestal, Sandia National Laboratories, Dr. W. Chen, Purdue University, Dr. V. Parameswaran, Indian Institute of Technology, Kanpur Dr. S. Hong and Anthony, Michigan State University for their valuable suggestions and help in various parts of the current research..

The author would also like to thank Dr. Parimal Maity for his guidance. In addition to this, the author thanks Michelle Raetz, Wei Zhang and Abhishek Dutta and Clarence Jilek for producing a conducive environment in the laboratory. The author acknowledges the support and help of Gail Berry, Mike McLean, Dan and Todd for their help throughout the research work.

The author thanks his friends Nirmal and Avishek who have always been an epitome of hard-work to the author. The author is grateful to Mrs. Milly Mukherjee and Dr. M. Ameen for their encouragement and previous guidance. Last but not the least, the author would also like to thank his parents who had always been a source of support and encouragements to the author and for helping him choose the right path in his life.

TABLE OF CONTENTS

LIST OF TABLES

LIST OF FIGURES

LIST OF SYMBOLS

$A_0,\ A_b$	Area of the Cross-section of the Incidence/ Transmission Bar
$A_s / A / S$	Area of the Cross-section of the Specimen
a	Radius of the Specimen
a_o	Average acceleration of the cross-section of the outer adherend
$\hat{a}_o$	Exact acceleration of the cross-section of the outer adherend
a_i	Average acceleration of the cross-section of the inner adherend
$\hat{a}_i$	Exact acceleration of the cross-section of the inner adherend
c	Velocity of propagation of a longitudinal wave in the Adherend
c_s	Velocity of propagation of a longitudinal wave in the Specimen
c_0	Velocity of propagation of a longitudinal wave in the Incidence/Transmission bar
d	Diameter of the Specimen

d_{ij}	Rate of Deformation Tensor
E_0, E_b	Modulus of Elasticity of the Incidence/Transmission Bar
E	Modulus of Elasticity of the Adherends
$\{\mathbf{f}^e\}$	Element load vector
$\{\mathbf{f}\}$	Global load vector
$F(t)$	Force applied at Outer and Inner adherends
G	Shear modulus of Adherends
G_a	Shear Modulus of Adhesive
J	Polar Moment of Inertia of the Specimen Cross-section
K	Kinetic Energy of the Specimen
$\left[\mathbf{K}^e\right]$	Element stiffness matrix
$[\mathbf{K}]$	Global stiffness matrix
L_s / h / l	Length of the Specimen
$\left[\mathbf{M}^e\right]$	Element mass matrix
$[\mathbf{M}]$	Global mass matrix
N_j^e	First order Lagrange Interpolation function at node j

P_1	Force at the specimen-incidence bar interface
P_2	Force at the specimen-transmission bar interface
p_{inc}	Mean traction acting at the face of the specimen in contact with the incidence bar
p_{ml}	Traction at the specimen-transmission bar interface
r	Radius of the Split Cylinder Sample
T	Equilibrium Time
T_0	Axial Stress-resultant in the Outer Adherend
T_i	Axial Stress-resultant in the Inner Adherend
t_f	Time of failure of the adhesive joint
t_0	Thickness of the outer adherend
t_i	Thickness of the inner adherend
t_a	Thickness of the adhesive layer
u	Axial velocity acting on the specimen's end
u_1	Axial displacements at the specimen-incidence bar interface
u_2	Axial displacements at the specimen-transmission bar interface

u_0	Horizontal displacements of the outer adherend
u_i	Horizontal displacements of the inner adherend
u_{io}	Horizontal displacements at the interface of the adhesive layer and the outer adherend
u_{ia}	Horizontal displacements at the interface of the adhesive layer and the inner adherend
u_{avg}	Average displacement along the cross-section of the adherend
V	Volume of the Specimen
v_i	Particle Velocity of the Specimen in the *i* direction
W	Internal Energy of the Specimen/ Weighting function
x, y, z	Material Coordinates of the Specimen
x_l	Length of Overlap
$D()/Dt$	Material Derivative
α	Material parameter depending on the material properties of the adhesive and adherend as well as structural properties of the adhesive joint
σ_1	Stress at the specimen-incidence bar interface
σ_2	Stress at the specimen-transmission bar interface
σ_s / σ_D	Specimen Stress

σ_{ij}	Cauchy Stress Tensor
τ_a	Shear Stress at the Adhesive-adherend interface
τ_0	Shear Stress in the Outer Adherend
τ_i	Shear Stress in the Inner Adherend
τ_s	Shear Strength of the Adhesive Joint
ε_1	Strain at the specimen-incidence bar interface
ε_2	Strain at the specimen-transmission bar interface
ε_s / ε	Specimen Strain
ε_{xo}	Axial strain in the outer adherend
ε_{xi}	Axial strain in the inner adherend
ε_i	Incident Strain
ε_t	Strain in the Transmission Bar
ε_r	Reflected Strain
$\hat{\gamma}_a$	Approximate shear strain in the adhesive
γ_o	Shear Strain in the Outer Adherend
γ_i	Shear Strain in the Inner Adherend

γ_a	Shear Strain of the Adhesive
γ_j^e	Approximate nodal shear strain
$\{\hat{\gamma}^e\}$	Element shear-strain vector
$\{\hat{\gamma}\}$	Global shear-strain vector
ρ	Density of the Specimen/ Split Cylinder Sample
ρ_0	Density of the Material of the Incidence/Transmission Bar
ψ	Transmission coefficient

CHAPTER 1

THE SPLIT HOPKINSON PRESSURE BAR

1.1 INTRODUCTION

Materials and structures are often subjected to dynamic loading. Examples of dynamic loading are forces applied to a body when it falls on the ground, collision of two vehicles, impact of a structure by a high velocity bullet, vigorous shaking of buildings during an earthquake, impact of ship by an iceberg etc. **[1.1]** From the mechanics point of view, there are three main consequences of a dynamic loading **[1.2]**.

(i) Stress waves or shock waves are propagated inside a body

(ii) The material undergoes large inelastic deformation

(iii) As an end consequence of impact, the modes of vibration within a body may be excited and the body can start "shaking" or vibrating vigorously

The material properties and behavior of solids are vigorously affected by the type of loading. There is a general trend among most solids to exhibit increased flow stress at higher rates of loading, while the toughness of the body decreases **[1.3]**. The term "strain-rate" is often used to define how quickly the material deforms under dynamic loading. Strain rate, $\dot{\varepsilon}$, is defined as the rate of change of strain with respect to time. At this point, it is helpful to provide some examples of the range of strain-rates encountered in typical dynamic problems. During an asteroid impact with the earth, the peak strain-rate developed is in the order of $10^8 s^{-1}$ **[1.1, 1.2].** For ballistic impact when the velocity of collision is of the order of a few kilometers per second, the typical strain rate developed is $10^5 - 10^6 s^{-1}$. For crash events (like an automobile crash), the typical strain-rate developed is in the order of $10^2 - 10^4 s^{-1}$. However, in practice, for example in the case of ballistic impact and asteroid collision, the peak strain-rates or the ultra-high strain rates (in the

orders of $10^6 s^{-1}$ and more) are sustained by a structure/solid for a very low period of time, and is usually preceded by a relatively longer time of high strain-rate (in the order of $10^3 - 10^4 s^{-1}$). It is in this long regime of high-strain rate that the material undergoes large deformation and therefore it is particularly important to understand the behavior of the material at this range of strain-rate. The Split Hopkinson Pressure Bar (Kolsky Bar) is essentially a loading device that is used to generate a high strain-rate ($10^2 - 10^4 s^{-1}$) loading condition in the specimen whose dynamic properties are desired. In the most commonly adopted experimental method with the Kolsky Bar, the aim is to study the stress-strain relationship of a material at a given temperature under high-strain rate conditions.

1.2 THE SPLIT-HOPKINSON PRESSURE BAR: THEORY

The Kolsky Bar loading device is essentially the same as a Universal Testing System for compression, except for three major differences.

I. The generation of load in the Kolsky Bar is generally not achieved by a hydraulic/pneumatic system, but is usually done by causing an accelerating projectile to impact one end of the set-up. However, in some modifications of the Kolsky Bar, often one of the bars is subjected to a static load. This bar is held by a clamp at some point along its length and then the clamp is suddenly released causing the load to propagate towards the specimen. **[1.4]**

II. The bars are not as stiff as the static load-frames. **[1.5]**

III. There is no "closed-loop" control system, i.e. the attainment of desired experimental conditions is achieved through a series of trial tests, **[1.5]** before embarking on the final experiments. This is because the testing conditions are dependent on the sample response.

The basic idea of the Kolsky Bar is that the specimen is deformed between two bars, which are used as force transducers and are excited above their resonant frequency. The main advantage of this set-up is that it can successfully decouple inertia effects and high strain-rate effects, which are generally coupled when materials are subjected to dynamic loading. Figure 1.1 shows the schematic of a Kolsky Bar.

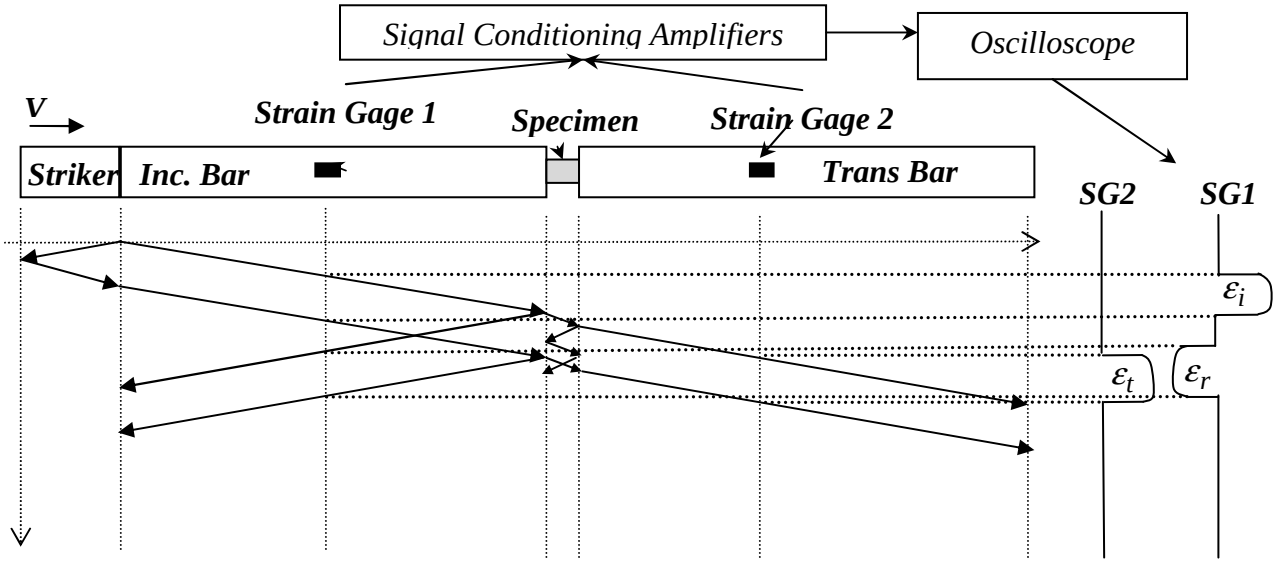

Figure 1.1 Schematic Representation of the Split Hopkinson Pressure Bar

The SHPB technique comprises a specimen, whose material properties are to be tested, sandwiched between two cylindrical bars called the incidence bar and the transmission bar. The cross-sectional geometry of these two bars is, in general, the same and they are made of the same material. An axial impact on the incident bar is caused by firing an air gun, which in turn generates a travelling compressive wave in the incident bar. Typically, the material and the cross-section of the specimen is not the same as that of the incidence bar. Hence, due to the mismatch of mechanical impedance of these two, when the travelling wave hits the specimen, a

part of it is reflected back into the striker bar and a part of it is transmitted through the specimen. The transmitted wave impinges on the transmission bar after travelling through the specimen and travels forth as a travelling wave, while a part of it is reflected back into the specimen. If the specimen is short enough compared to the length of the stress pulse, then it is assumed that stress equilibrium is achieved due to several reflections within the specimen in a time much shorter than the duration of the test.

For a thin, longitudinal bar the equation of motion for the axial displacement, *u*, is given by **[1.6]**

$$\frac{\partial^2 u}{\partial x^2} = \frac{1}{{c_0}^2}\frac{\partial^2 u}{\partial t^2} \tag{1.1}$$

where c_0 is the velocity of a longitudinal wave in the material of the bar and is given by

$$c_0 = \sqrt{\frac{E_0}{\rho_0}} \tag{1.2}$$

where E_0 and ρ_0 represent the Modulus of Elasticity and density of the material of the incidence/ transmission bar.

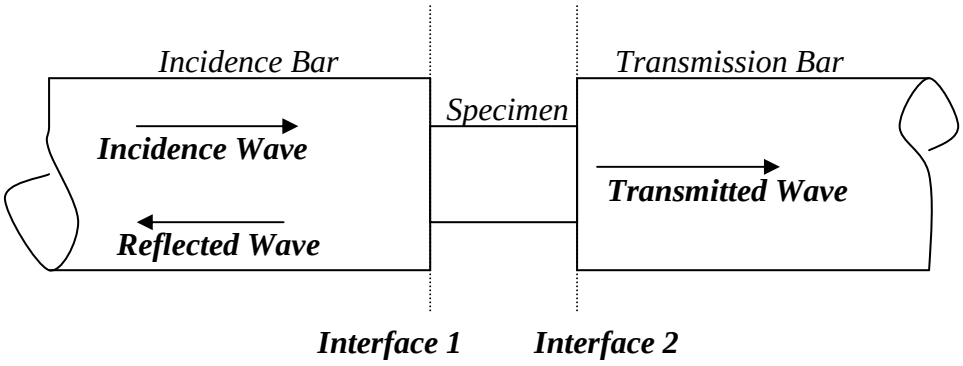

Figure 1.2. Schematic of the Specimen-Bar Interfaces

The solution to Equation (1.1) is given by the classical D' Alembert's rule to obtain the displacement as

$$u = f(x - c_0 t) + g(x + c_0 t) \tag{1.3}$$

Here the functions *f* and *g* are arbitrary functions to be determined by initial conditions of the problem. The stress, σ, strain, ε, and particle velocity, *v* can be determined from (1.3) as follows:

$$\varepsilon = \frac{\partial u}{\partial x} = \frac{\partial f}{\partial x} + \frac{\partial g}{\partial x} = f' + g' \tag{1.4}$$

$$\sigma = E_0 \left(f' + g' \right) \tag{1.5}$$

$$\dot{u} = \frac{\partial u}{\partial t} = -c_0 f' + c_0 g' = c_0 \left(-f' + g' \right) \tag{1.6}$$

Let the subscript *i* denote the parameters related to the incidence pulse, *r* the parameters related to the reflected pulse and *t* the parameters those related to the transmitted pulse. Further, let the subscripts 1 and 2 denote parameters related to interfaces 1 and 2, as denoted in figure 2.1. Thus, the displacements, stresses and strains at interfaces 1 and 2 may be developed as follows.

$$u_1 = f_1 \left(x - c_0 t \right) + g \left(x + c_0 t \right) = u_i + u_r \tag{1.7}$$

$$u_2 = f_2 \left(x - c_0 t \right) = u_t \tag{1.8}$$

$$\varepsilon_1 = f_1' + g_1' = u_i' + u_r' = \varepsilon_i + \varepsilon_r \tag{1.9}$$

$$\varepsilon_2 = f_2' = u_t' = \varepsilon_t \tag{1.10}$$

$$\sigma_1 = E_0 \left(\varepsilon_i + \varepsilon_r \right) \tag{1.11}$$

$$\sigma_2 = E_0 \varepsilon_t \tag{1.12}$$

$$\dot{u}_1 = c_0 \left(-\varepsilon_i + \varepsilon_r \right) \tag{1.13}$$

$$\dot{u}_2 = -c_0 \varepsilon_t \tag{1.14}$$

The average stress, σ_s in the specimen arises from the assumption that the force acting on the specimen is the average force from interfaces 1 and 2. Thus,

$$\sigma_s = \frac{\sigma_1 A_0 + \sigma_2 A_0}{2A_s} = \frac{E_0 A_0}{2A_s}\left(\varepsilon_i + \varepsilon_r + \varepsilon_t\right) \tag{1.15}$$

where A_0 and A_s are the area of cross-section of the incidence/transmission bar and the specimen respectively. The strain-rate in the specimen, $\dot{\varepsilon}_s$, is proportional to the relative velocity of interfaces 1 and 2. This is therefore given by

$$\dot{\varepsilon}_s = \frac{\dot{u}_2 - \dot{u}_1}{l_s} = \frac{c_0}{l_s}\left(-\varepsilon_t + \varepsilon_i - \varepsilon_r\right) \tag{1.16}$$

In Equation (1.16), l_s denotes the length of the specimen. The specimen strain, ε_s , can thus be obtained as

$$\varepsilon_s = \int_{\tau=0}^{t} \dot{\varepsilon}_s d\tau \tag{1.17}$$

If the specimen deforms uniformly, then

$$\varepsilon_i + \varepsilon_r \cong \varepsilon_t \tag{1.18}$$

Under these conditions, equations (1.15) and (1.16) modify as

$$\sigma_s = \frac{E_b A_b}{A_s}\varepsilon_t \tag{1.19}$$

$$\dot{\varepsilon}_s = -\frac{2c_0}{l_s}\varepsilon_r \tag{1.20}$$

Figure 1.3 shows representative incidence, reflected and transmitted pulses for a dynamic experiment of Aluminum 6061-T6 specimen, and the corresponding stress-strain relationship for the same.

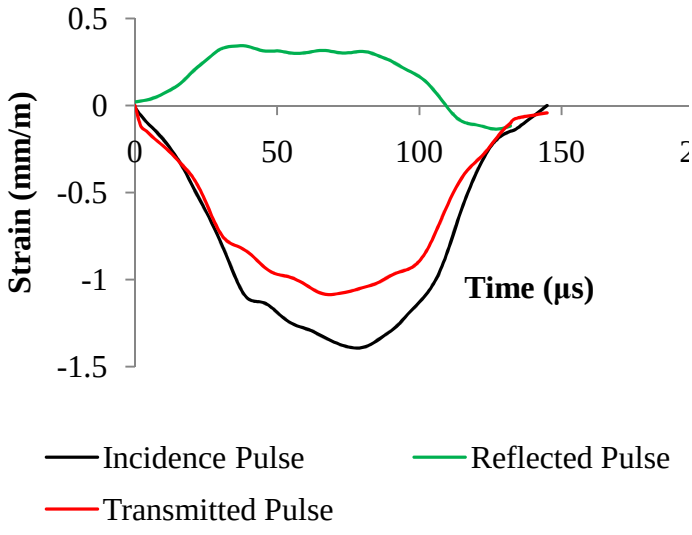

(a)

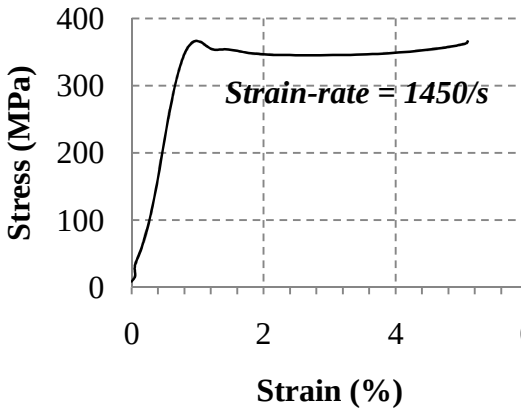

(b)

Figure 1.3 Representative curves in a Kolsky Bar Experiment with Al6061-T6 specimen (a) Profile of the pulses as measured by strain gages (b) Dynamic Stress-strain Curve

For interpretation of the references to color in this and all other figures, the reader is referred to the electronic version of this thesis.

Equations (1.1) through (1.20) follow from Shukla and Dally **[1.1]**.

1.3 The Split Hopkinson Pressure Bar: Discussions

In order to attain a representative dynamic stress-strain curve of the specimen, and to enable post-impact observations, the following requirements must be fulfilled in a Kolsky Bar experiment **[1.5]**

(i) The specimen must deform at the desired strain-rate. This requirement means that the rise time of the incidence pulse must be kept as small as possible in comparison to the entire length of the pulse. Ideally, for the impact of two elastic bodies, a rectangular pulse is generated in the second body. However, in reality it is almost impossible to obtain a pulse with a zero rise-time. Therefore, the condition is usually achieved by using a long projectile and adequate pulse shaping techniques. In fact, it can be shown from one-dimensional elastodynamic theory **[1.6]** that if the length of the projectile, whose density is ρ_0,is l_0, and the velocity of the projectile at the time of impacting the incidence bar is *V*, the peak amplitude of the strain-pulse developed in the incidence bar is given by

$$\varepsilon_i\big|_{\max} = \frac{\rho_0 c_0 V}{2E_0} \tag{1.21}$$

while the duration of the total pulse t_{inc}, is given by

$$t_{inc} = \frac{2l_0}{c_0} \tag{1.22}$$

If t_{inc} is comparable to the rise time of the incidence pulse, then the regime of peak strain is considerably low. The results from such an experiment do not present a representative behavior of the material as the peak strain-rate, because prior to achieving the peak strain-rate the material has already been plastically deformed. If the length of the projectile is long, then the numerator in the right hand side of Equation (1.22) is considerably large, thus increasing the total duration of the pulse. The rise time, in such pulses, are negligible compared to the overall length of the pulse.

The technique of pulse shaping comprises placing a thin sheet of “buffer” material (like Copper, Rubber, Paper, Polycarbonate etc) between the incidence bar and the striker. As the soft

material undergoes large deformation at impact, the material generally being of low mechanical impedance than the incidence bar, causes a delay in the over-all pulse length due to several internal successive reflections of the pulse within it. This reduces the amplitude of the incidence pulse and considerably elongates the length of the pulse.

The topic of achieving desired test conditions by the pulse-shaping technique has been an active field of research. In a study by Frew *et. al.* **[1.7]** an analytical model for the response of a pulse shaper had been established for an elastic-plastic material. The recommendation was to use a "dual" pulse shaper, the striker end of which was manufactured by annealed copper and the incidence bar end of the same was manufactured by mild steel. In order to generate dynamic hysteresis loops, a similar technique was adopted by Song and Chen **[1.8].** In a research by Vecchio and Jiang **[1.9]**, a comparison was made between a pulse-shaped SHPB experiment and a non-pulse-shaped SHPB experiment. It was found that after pulse shaping, a large zone of constant strain-rate was maintained for both high work-hardening materials as well as for low work-hardening materials. For testing brittle materials, Frew *et. al.* **[1.10]** used a thin disc of annealed copper as pulse shaping material to ensure the attainment of constant strain-rate prior to material failure. For testing shape-memory alloys, a similar pulse-shaping was used by Nemat-Nasser *et. al.* **[1.11]** except that he used a copper tube, instead of a copper disc. In a study on the dynamic strength of adhesive lap joints Srivastava *et. al.* **[1.12]** used a rubber pulse shaper for the experiments.

(ii) Deformation in the specimen is nearly uniform. This means that the strain in the specimen is homogenous and the average value of the strain obtained in Equation (1.20) and (1.17) defines the behavior of the entire specimen. If the specimen deformation is non-uniform, for example due to wave-propagation effect, then the average value of the specimen will no

longer reflect the deformation history of the entire specimen. It is usually a practice in a Kolsky Bar experiment to measure the specimen stress from force equilibrium considerations at interface 2 and the specimen strain and strain-rate from interface 1. It is then assumed that the stresses and strain so obtained are the same at each point, and the stresses at one instant of time from interface 1 correspond to the value of strain at the same instant of time at interface 2. This can only be assumed if the specimen deformation is uniform. This is generally achieved by keeping the length of the specimen small.

(iii) Stress in the specimen is uniform. This requires that there is negligible wave-propagation effect in the specimen. This requirement amounts to effectively neglecting the effect of axial inertia on the specimen. This is achieved by choosing the specimen length to be much shorter than the total length of the incidence pulse.

Conditions (i) and (ii) have called for thorough research for the past few decades. Both conditions boil down to ensuring that the force at both ends of the specimen is uniform. This condition is generally not met in the first few microseconds of an experiment. However, as the incident stress-wave on the specimen undergoes successive reflections, the stress builds up in the specimen and a quasi-static condition is achieved. Based on an elastodynamic analysis, attempts have been made to quantify the equilibrium time in the specimen. Davies and Hunter **[1.13]** showed that at least three internal transits of the incident wave are needed for achieving stress-equilibrium in the specimen. Similar conclusions have been drawn by Follansbee *et. al.* **[1.14],** Chen **[1.15]** and Wu and Gorham **[1.16].** A more conservative estimate was provided by Subhash and Ravichandran **[1.17]** who proposed that at least eight internal reflections of the incidence wave is necessary for stress equilibrium. In a thorough analysis by Yang and Shim **[1.18]**, it was demonstrated that a pulse with a finite rise time takes lesser time to be equilibrated than a

rectangular pulse. However, the conclusions have been based on the assumption that the specimen remains elastic till equilibrium is achieved.

(iv) Specimen is loaded once by a well-defined loading history. This requires that the specimen is not subjected to a train of pulses. If the incidence and the transmission bar are very short compared to the travel time of the pulses along the incidence and transmission bars, then before the first incidence pulse is reflected back on the specimen, another pulse impinges on the specimen. The specimen is then subjected to successive loads and the stress and strain history on the specimen cannot be obtained. Generally, by choosing the length of the incidence and transmission bars equal to 1m and by choosing a small striker bar (long enough to satisfy condition i) this condition is satisfied. In practice, a striker of length below 250 mm is found to give satisfactory results.

In addition to the above mentioned requirements, there are also a number of assumptions that have to be satisfied for Equations (1.17) through (1.20) to hold.

(i) The Hopkinson Bars remain linear elastic. This not only allows the use of bonded-resistance strain-gages to measure the strains in the incidence and transmission bars repeatedly, but also allows the use of the elastodynamic theory to estimate the stress and strain in the specimen. The bars are therefore generally made of metals with high yield strength like maraging steel or high yield-strength aluminum (Alloy 7075, for example). This also limits the input velocity of the striker as follows.

$$V < \frac{2\sigma_y}{c_0} \tag{1.23}$$

where σ_y is the yield-stress of the bar

(ii) The effects of dispersion in the bars are small. This means that the pulses as recorded by the strain-gages are representative of the strains at interfaces 1 and 2. However, from elastodynamic theory, it turns out that the phenomenon of longitudinal wave propagation in a bar has a dispersive effect, in that the wave-length and the frequency of the waves are inter dependant on one-another. Thus, the incident, reflected and transmitted pulses change as they move along the input and output bars. However, Equations (1.1) through (1.20) have been based assuming the condition that the shape of the pulse does not change as they travel along the bars. Two consequences of dispersion are important. First, dispersion inevitably induces superimposed oscillations in the loading of the specimen. Second, shorter stress pulses with sharper rise times cause greater dispersion because of the greater high-frequency content and the wider range. One approach to minimizing the effects of dispersion is to use pulse-shaping materials that are placed between the impacting projectile and input bar .This results in the shaping of the incident wave with a longer rise time and thus lower dispersion.

Davies **[1.19]** used numerical results from the Pochhammer–Chree frequency equations to determine the dispersion of a travelling elastic wave. He found that in the Hopkinson bar test, the wave belong to the first mode of vibration. Lifschitz **[1.20]** developed an algorithm for viscoelastic corrections. Follansbee *et. al.* **[1.21]** repeated the calculations of dispersive wave, originally made by Davies, to analyze split Hopkinson pressure bar results. They showed that the fundamental mode of vibration is excited in the impact test of the SHPB and a dispersion correction was suggested to reduce the magnitude of the oscillations of the stress–strain curves. In a numerical study by Govender *et. al.* **[1.22]**, evidences of higher modes of frequency being excited was shown.

(iii) Effects of radial inertia are negligibly small. The compression loading is accompanied by radial expansion of the specimen. This radial expansion is opposed by a radial inertial effect which increases by decreasing pulse length and increasing pulse amplitude. A detailed discussion of radial inertia in samples in a Kolsky Bar Experiment is given in Chapter 2 of the report.

(iv) The effects of end conditions are neglected. This effectively boils down to stating that the frictional coefficients at interfaces 1 and 2 are negligibly small. Indeed, Equation (1.1) through (1.20) are based on a one-dimensional analysis. The effects of friction at the ends cause a state of non-uniform triaxial state in the specimen. Friction constraints the edges of the specimen to expand freely and results in an over-reading of the yield stress. In a study by Bertholf and Karnes **[1.23]** the choice of critical specimen dimensions so that the frictional restraints are minimized as well as axial equilibrium and minimal inertial stress is attained are discussed. In addition, the most widely adopted practice is to lubricate interfaces 1 and 2 so that the effects of friction are minimized. Lubricants are shown to be more effective in a high strain-rate experiment than in a static experiment, simply because the lubricant has a lower time to fail. Molybdenum Disulfide, Graphite, Petroleum Jelly, Teflon are the common forms of lubricant generally adopted. A report of different lubricants and their effectiveness in reducing the co-efficient of friction has been widely studied **[1.16, 1.22, 1.24, 1.25, 1.26].** In addition to effective lubrication, the specimen dimensions also play an important role in ensuring minimal frictional restraints. Gorham **[1.16]** pointed out that larger specimens deformed at the same strain rate involve longer radial displacement at higher velocities than in the case of small specimens. Lubricant breakdown is more likely under large displacements and loss of lubricant by jetting is enhanced at high velocities This may subject the larger specimens to velocity-dependent frictional restraints, which can contribute to a *prima facie* strain rate sensitivity of the material.

1.4 The Split Hopkinson Pressure Bar: Modifications

The Split Hopkinson Pressure Bar technique has been developed since its inception for testing different types of materials. As the design of an experiment in a Kolsky Bar is widely dependant on the material response, there is a lack of "closed-loop" control for *a priori* experimental design. In this section a more-or-less generalized technique for different types of materials and testing conditions are presented.

(i) Brittle Materials.

Brittle materials have the general characteristic that they have a linear elastic stress-strain profile and have very little plastic deformation. The only reliable data obtained in case of brittle materials from a Kolsky Bar experiment is their failure stress. These materials fail at low values of strains and can fail prematurely from high stress concentrations. It is therefore imperative to ensure that the materials are in a state of equilibrated stress and deformation before their failure. Pulse shaping is critical to these types of materials. A special case of brittle materials is ceramics. In addition to the problems described above, ceramics being sufficiently hard, can indent the bar surfaces, thus causing considerable stress-concentrations along the circumference of the specimen end faces. In a research by Subhash and Ravichandran **[1.27]**, the use of impedance-matched tungsten-carbide insert was recommended at the specimen-bar interfaces. The inserts are generally confined by a steel ring of slightly smaller thickness than the inserts to ensure maximum impedance match. However, the use of inserts can lead to repeated loading on the specimen, therefore the use of sabot mass is recommended as it immediately produces a tensile pulse following the initial compressive pulse in the incidence bar. This causes the separation of the bar-specimen interface immediately as the tensile pulse reaches the specimen. Figure 1.4 shows the recommendations for a brittle material suggested by Subhash **[1.27]**

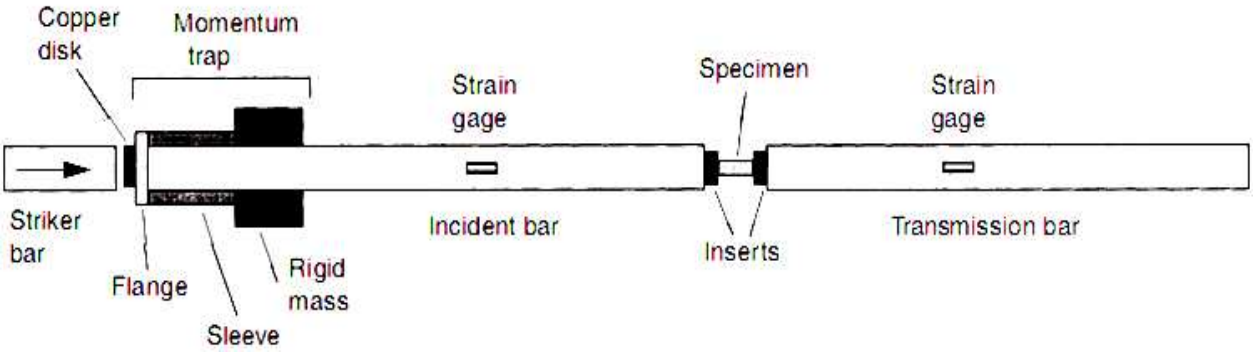

Figure 1.4. Modification for brittle materials in a Kolsky Bar **[1.27]**.

A detailed research on the effect of sabot mass and momentum trap has been conducted by researchers **[1.28, 1.29, 1.30]**, while a research on the pulse shaping techniques and limiting strain-rates [**1.7, 1.17, 1.27]** indicate that a ramp loading generated by a copper pulse shaper is ideally suited for testing brittle materials.

(ii) Low impedance materials

Low impedance materials like polymers, rubbers, foams are particularly difficult to test because of the following reasons

- Attainment of axial equilibrium takes a long time in these
- The transmitted signal is very low

Several modifications have been suggested for this. Chen **[1.31]** used a hollow transmission bar for measuring the forces, the hollow transmission bar, having a reduced area, has lower mechanical impedance and thus the signals are considerably amplified in the same. Chen **[1.32]** also used quartz-crystal transducers at the specimen-bar interfaces to enable direct measurement of forces in the specimen. However, in a study by Weerasooriya**[1.33],** the quartz crystal transducer at the incidence face was found to be highly sensitive to acceleration, thereby posing a problem for accurate determination of the incidence force, unless the reading are post-corrected

for transducer acceleration. In a recent study by Hiermaier and Meenken, **[1.34]**, the use of Polyvinyl Denoflouride (PVDF) thin film sensors at the incidence and transmission interfaces has been demonstrated. The use of viscoelastic pressure bars, with correction for attenuation and dispersion have also been recommended **[1.35, 1.36, 1.37, 1.38, 1.39].** The use of viscoelastic bars poses the added difficulty of post-correction of the strain signals in the incidence and transmission bar. Several post-correction algorithms have been proposed and most of these require a precise knowledge of the material properties of the polymer used for accurate post-correction of solutions. In a recent study by Johnson *et. al.* **[1.40]** an excellent comparison of the testing techniques for soft materials has been provided. The use of a viscoelastic bar reduces the level of noise and high-frequency oscillations in a Kolsky Bar, while it severely brings down the strain-rate. A hollow aluminum transmission bar, on the other hand, enables higher strain-rate testing and the analysis is also easier, but the level of noise is relatively higher in this.

1.5 Description of the current research work

The current research does not focus on characterization of a particular material using a Split Hopkinson Bar, rather focuses on some theoretical aspects of the Hopkinson Bar experimental techniques.

Chapter 2 proposes a standard for adopting non-cylindrical specimens in a Split Hopkinson Pressure Bar. Despite the practice of using cylindrical specimens in a Split-Hopkinson Pressure Bar (Kolsky Bar) experiment, the use of non-cylindrical prismatic specimens is not uncommon. This is convenient when testing extra-soft materials like brain-tissues, muscles or samples which are brittle and cannot be machined to an exact cylindrical shape like bone-samples. The use of a non-cylindrical sample with a flat surface also renders the specimen amenable to a 2-D image

correlation algorithm. This part of the current research aims to show the feasibility of using non-cylindrical specimens in a Kolsky Bar. For this, experiments were conducted with a model material of different model cross-sections at a nearly constant strain-rate in the Split Hopkinson Pressure Bar. The findings suggest the use of a suitable characteristic cross-section dimension of the specimen to determine the critical slenderness ratio while selecting a non-cylindrical prismatic specimen. It has been shown that if the specimen design is governed by the suggested slenderness criterion, then there is no effect of specimen length or cross-sectional shape on the stress-strain curve of the material. Through the use of a computational code, the research also shows the effect of non-uniform axial stress-distribution along the cross-section of the specimen, resulting due to specimen geometry. On quantification of the stress non-uniformity along the cross-section of the specimen, the findings indicate that the magnitude of the non-uniformity is both small and temporary.

Chapter 3 addresses the issue of the drastic effects of over-lap area in adhesive bonded lap joints for determination of the dynamic strength of the same. For this, experiments were conducted at different loading rates, for identical metallic adherends bonded by a two-part epoxy adhesive. Four different types of specimens were adopted, all with a given adhesive thickness. The length of overlap and the out-of-plane thickness of the adherends were varied, resulting in four different area of overlap. It was found that the average strength, as predicted by the Kolsky Bar, increases with a decrease of overlap area. An elastodynamic model for the shear strain of the adhesive-bonded single lap joint was developed to investigate this drastic effect of overlap area on the average strength of the joint. The mathematical model was found to be dependent on both the material properties of the adherend and adhesive, as well as the structural properties of the joint, viz. the out-of-plane thickness and the thickness of the adhesive layer. A combined

experimental-numerical technique was used to predict the strain distribution over the length of the bond in the adhesive. It was found that the edges of the adhesive were subjected to maximum strain, while a large part of the adhesive was found to exhibit zero shear strain. For a given out-of-plane thickness of the adhesive/adherends, reducing the overlap length slightly increased the peak strain in the adhesive joint, however, the total length of non-zero strain at the time of failure remained the same. But, if the out-of-plane thickness is reduced for a given overlap length, the maximum strain is decreased, along with a larger increase of the length of adhesive with non-zero strain. The cumulative effect of averaging the strain over the entire overlap area was decreased shear-strain for an increased overlap area. The Kolsky Bar was identified to predict conservative estimate of the shear-strength of an adhesive bonded lap joint, under high rates of loading.

Chapter 4 addresses a design of a new Tensile Hopkinson Bar at the Composite Vehicle Research Center. The design proposed here comprises of an incidence bar which is 10 feet in length. An end of the incidence bar is coupled to a flange, whose diameter is greater than diameter than the incidence bar. An annular projectile with its inner diameter equal to the diameter of the incidence bar and outer diameter equal to the flange is allowed to impinge on the flange, thereby generating a compressive pulse in the same, which traverses the entire length of the flange and is reflected from the free end as a tensile pulse. This pulse is used for loading the specimen. Choice of a proper flange length, the use of a momentum-trap and are found to be crucial for the proper functioning of the Split Hopkinson Tensile Bar. Copper was selected as the model material and its dynamic tensile properties were determined using the Split Hopkinson Tensile Bar.

1.6 Conclusion

This chapter was aimed at developing the theoretical background of the Split Hopkinson Pressure Bar technique. The technique of the Split Hopkinson Pressure bar was described. The equations for calculation of specimen stress, strain-rate and strain were derived. Different assumptions involved in the Kolsky Bar experimental technique was addressed along with relevant review of literature of the same. Issues related to characterization of some types of materials were addressed along with relevant review of literature of the same. Finally, the chapter concluded with a brief abstract of the scope of the current research work.

CHAPTER 2

ON THE USE OF NON-CYLINDRICAL SPECIMENS IN A KOLSKY BAR

2.1 INTRODUCTION

The Split-Hopkinson Pressure Bar (SHPB) is a standard apparatus for measuring the mechanical response of materials at high strain-rates. The SHPB technique comprises a specimen, whose material properties are to be tested, sandwiched between two cylindrical bars called the incidence bar and the transmission bar. The cross-sectional geometry of these two bars is, in general, the same and they are made of the same material. An axial impact on the incident bar is caused by firing an air gun, which in turn generates a travelling compressive wave in the incident bar. Typically, the material and the cross-section of the specimen is not the same as that of the incidence bar. Hence, due to the mismatch of mechanical impedance of these two, when the travelling wave hits the specimen, a part of it is reflected back into the striker bar and a part of it is transmitted through the specimen. The transmitted wave impinges on the transmission bar after travelling through the specimen and travels forth as a travelling wave, while a part of it is reflected back into the specimen. If the specimen is short enough compared to the length of the stress pulse, then it is assumed that stress equilibrium is achieved due to several reflections within the specimen in a time much shorter than the duration of the test. Based on one-dimensional calculations **[2.1]**, it has been established that the amplitude of the transmitted pulse is a measure of stress in the specimen and the amplitude of the reflected pulse is useful in calculating the strain rate in the specimen. The equations for stress σ_s , strain rate $\dot{\varepsilon}_s$ and strain ε_s in the specimen of cross-sectional area A_s and length L_s deforming homogenously are given by:

$$\sigma_s(t) = \frac{A_0 E_0 \varepsilon_t(t)}{A_s} \tag{2.1}$$

$$\dot{\varepsilon}_s = -\frac{2c_0 \varepsilon_r(t)}{L_s} \tag{2.2}$$

$$\varepsilon_s(t) = \int_0^t \dot{\varepsilon}_s(\tau) d\tau \tag{2.3}$$

where, A_0 and E_0 refer to the area of the cross-section and modulus of elasticity of the incidence bar respectively, ε is the axial strain; while the subscripts *t*, and *r* refer to the waves as recorded as a transmitted wave in the transmission bar and reflected wave in the incident bar respectively; c_0 is the velocity of propagation of a longitudinal wave in the bar of mass density ρ_0

$$c_0 = \sqrt{E_0 / \rho_0} \tag{2.4}$$

Generally, the specimen whose material-properties are desired is cylindrical. However, cases when non-circular specimens are chosen are not uncommon. This is particularly convenient when working with specimens which are difficult to be machined into an exact cylindrical shape like muscles **[2.2]**, bones **[2.3],** and have been commonly used for testing graphite epoxy composites **[2.4]**, carbon-epoxy laminated composites **[2.5],** graphite epoxy-composite laminates **[2.6]**, RCC Materials **[2.7]**. Figure 2.1 shows some examples of specimens where an exact cylindrical shape was difficult to prepare.

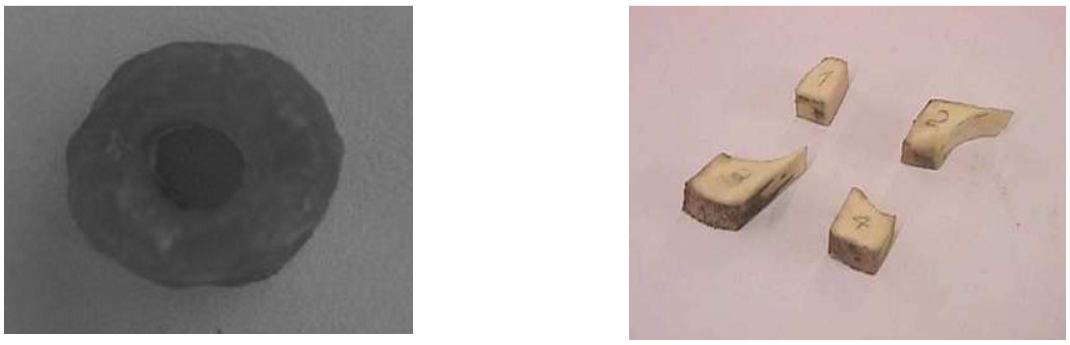

(a) (b)

Figure 2.1: Examples of cases where machining cylindrical specimens are difficult

(a) Porcine Muscle **[2.2]** (b) bovine cortical bone **[2.3]**

With advancements in optical methods for full-field strain calculations, the combination of image-correlation techniques for specimen strain calculations, combined with impact loads generated with a Kolsky Bar has been widely practiced and adopted **[2.8,2.9]**. Usually, if the specimen is cylindrical, as is typically adopted, then a 3-D image correlation algorithm is adopted. In a recent study by Schmidt and Tyson **[2.10]** the relative convenience of 2-D image correlation over 3-D image correlation has been reported. If a 2-D image correlation is to be adopted, then there is a necessity of a least one flat face on the specimen, which causes one to deviate from cylindrical to non-cylindrical specimens. In a study by Siviour **[2.11]**, the use of cuboidal specimens in a compression Hopkinson Bar has been demonstrated.

In a cylindrical specimen, the specimen design is governed by choice of an appropriate slenderness ratio (which is the ratio of the length to diameter of the sample). In such specimens, the critical value of the slenderness ratio has been researched **[2.12, 2.13]**. However, in a non-cylindrical specimen such a slenderness-ratio has not been defined. Recent studies on the effect of specific cross-sectional shapes of specimens on the dynamic stress-strain curve in a Hopkinson Bar Experiment have been carried out by Eyassu and Vinson **[2.4]** and Pankow *et. al.* **[2.14]** and the results indicate that the shape of the cross-section does not affect the dynamic stress-strain curve of the material drastically. In the current investigation, a general design criterion for any non-cylindrical samples is proposed by suggesting an appropriate cross-sectional dimension and a slenderness ratio for a specimen with arbitrary cross-sectional geometry. Furthermore, a model for radial inertia for non-cylindrical specimen has been proposed by extending the existing model of Samanta **[2.15]** for cylindrical specimen. With the use of a model material and model geometry of specimen cross-section, the effect of cross-

sectional shapes of a prismatic specimen has been studied when the design of specimen is carried out based on the recommendations suggested in the current investigation.

2.2 Design of Specimen

In a Hopkinson Bar Experiment for material characterization, there exist several important factors which guide the design of a specimen. The major considerations in designing a specimen of appropriate dimension are:

- The effect of friction at the interface between the bars and the sample
- The effects of lateral inertia in the sample and,
- The necessity to ensure the condition that the specimen is subjected to uniform stresses throughout its length.

In the current investigation, Aluminum 6061 alloy has been chosen as the model material for studying the effect of cross-sectional shapes. The model cross-sectional shapes of specimens adopted are rectangular, square, and hexagonal; and are all compared against specimens with circular cross-sections. Table 1 summarizes the specimens adopted in the current investigation.

Table 2.1. Description of Specimens Adopted in the Current Investigation

Cross-section of the Specimen	Length of the Specimen	Nomenclature
Hexagon (Hex1) Edge Size: 6 mm	5.5 mm	Hex1short
	8 mm	Hex1long
Hexagon (Hex2) Edge Size: 4.5 mm	4.5 mm	Hex2short
	6 mm	Hex2long
Rectangle (Rec1) Edge Sizes: 6 mm x 6mm	3.5 mm	Rec1short
	5 mm	Rec1long
Rectangle (Rec 2) Edge Size: 6.5 mm x 12.7 mm	6 mm	Rec2short
	8 mm	Rec2long
Circle (Circ1) Diameter: 12.7 mm	6.4 mm	Circ1short
	9 mm	Circ1long
Circle (Circ 2) Diameter: 11 mm	5.5 mm	Circ2short
	8.3 mm	Circ2long

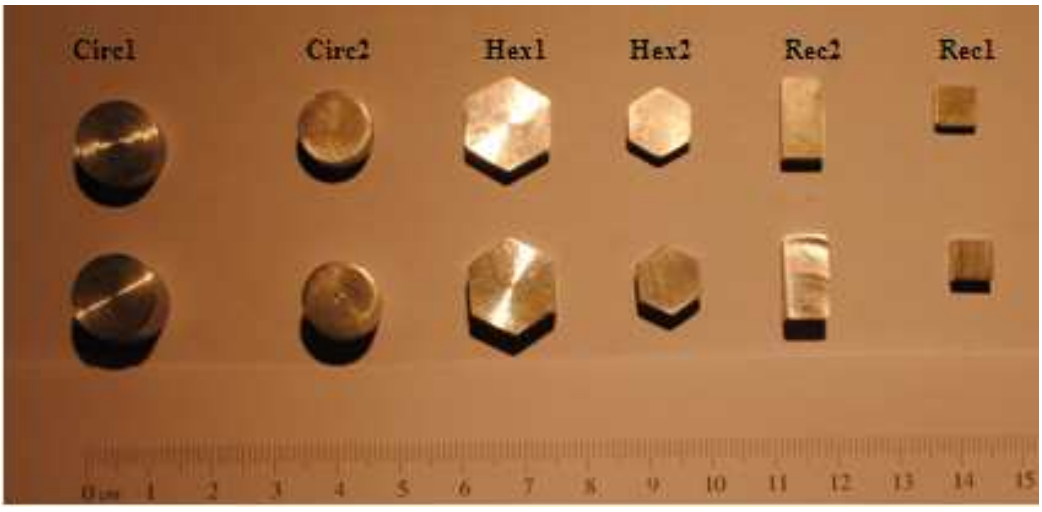

Figure 2.2 Specimens adopted in the current investigation

A major assumption involved in the calculations of the dynamic stress-strain behavior of a specimen is that the specimen can be approximated as a one-dimensional object, in which at any given cross-section, the stress is the same, i.e., the radial distribution of stress is uniform. However, as a specimen is subjected to a compressive wave, due to Poisson's effect, the cross-section of the specimen tends to expand, which is resisted by an inertial effect. For specimens with circular cross-section, the stress arising due to radial inertia has been widely studied and researched. Details of these can be found in Kolsky [**2.1**], Davies and Hunter [**2.16**], Samanta [**2.15**], Gorham [**2.17,2.18**], Forrestal *et. al.*[**2.19**], Song *et. al.* [**2.20**], Warren and Forrestal [**2.21**] and an excellent account of the same is given in a book chapter by Ramesh [**2.13**]. In the current investigation, we propose a model for radial inertia for non-circular specimens, following the approach of Samanta by the use of material coordinates for the specimen. The detailed derivation and discussion regarding the same can be found in the appendix A of the paper. Here, however, we present the final result in equation (2.5).

$$\sigma_D = -p_{ml} - \rho\left(\frac{J}{4A} - \frac{h^2}{6}\right)\ddot{\varepsilon} + \rho\left(\frac{J}{8A} + \frac{h^2}{6}\right)\dot{\varepsilon}^2 \tag{2.5}$$

Here σ_D denotes the stress in the specimen, p_{ml} is the traction at the specimen-transmission bar interface, ρ is the density of the specimen, J and A refer to the polar moment of inertia and area of the cross-section of the specimen, and h is the length of the specimen. For a material of high flow stress, the effect of inertia is negligibly small, and as has been shown in the appendix, is smaller by orders of magnitude for aluminum specimens. It can be significant for materials of low yield strength, as has also been reported in literature **[2.13, 2.21].**

In a typical Kolsky Bar experiment, stresses and strains are measured from the signals produced in the strain gages mounted on the transmitter bar and the incidence bar respectively. It

is assumed that the stress and strain are uniform throughout the length of the specimen. This in turn, results in an assumption that neglects the effects of axial inertia in the specimen and this holds good only if the specimen is short enough so as to attain axial equilibrium due to several succesive reflections of the stress wave generated in the specimen in a time much shorter than the entire duration of the test **[2.22, 2.23, 2.24, 2.25, 2.26].** From an elastodynamic analysis for composite materials, Subhash and Ravichandran **[2.23, 2.24]** showed that approximatly eight internal reflections of a stress-wave in the specimen are needed for axial equilibrium, and provided the following equation for equilibrium time, *T*:

$$T = 8\frac{l_s}{c_s} \tag{2.6}$$

where l_s is the length of the specimen and c_s is the velocity of sound-wave in the specimen. This shows that longer the length of the specimen, longer is the time when the assumption of stress uniformity throughout the specimen holds. This implies that a shorter specimen is better in terms of stress-uniformity throughout the length of the sample, however, shorter the sample, greater are the effects of interfacial friction. In the case of cylindrical specimens, the critical slenderness ratio, based on the considerations of inertia, axial uniformity of stresses and interfacial friction has been researched widely and for a sample of diameter *d* and length *l* an accepted value of slenderness ratio **[2.14]** is

$$\frac{l}{d} = 0.5 \tag{2.7}$$

A less restrictive slenderness ratio is **[2.15]** is given by

$$\frac{l}{d} \leq 1 \tag{2.8}$$

Unlike in a cylindrical specimen, where the diameter is chosen to be the characteristic cross-sectional dimension, in a non-cylindrical specimen, the characteristic cross-sectional dimension needs to be arrived at. This arises from the derivation of inertial stresses in the sample, where if J is the polar-moment of inertia of the cross-section of the sample and A is the area of the cross-section, then the characteristic cross-sectional dimension $\sqrt{J/A}$ replaces the terms involving diameter (d) in the inertial stress terms. Thus, the more general term, $\sqrt{J/A}$ (which is equivalent to $d/2\sqrt{2}$ for a cylinder), forms the appropriate characteristic cross-sectional dimension for a specimen of arbitrary cross-section. The critical slenderness ratio of a specimen of arbitrary cross-section therefore becomes

$$\frac{l}{\sqrt{\frac{J}{A}}} = 1.4 \tag{2.9a}$$

$$\frac{l}{\sqrt{\frac{J}{A}}} \leq 2.8 \tag{2.9b}$$

this can be combined to give

$$1.4 \leq \frac{l}{\sqrt{\frac{J}{A}}} \leq 2.8 \tag{2.10}$$

On substitution of the value for $\sqrt{J/A}$ for a circle, Equations (2.9)-(2.10) reduce to Equations (2.7) - (2.8); however, Equations (2.9)-(2.10) is valid for a prismatic specimen with any cross-sectional shape, whereas Equations (2.7)-(2.8) are valid for specimens with circular cross-sections alone.

To check if the length of the specimen of a given cross-section affects the dynamic stress-strain curve, two different lengths of the specimen were adopted, subjected to the restrictions

imposed by Equation (2.9) and (2.10). Table 2.2 summarizes the value of slenderness ratio for each of the samples chosen.

Table 2.2: Slenderness ratio of the specimens adopted

Sample Name	**Slenderness ratio** $l/\left(\sqrt{J/A}\right)$
Hex1long	2
Hex1short	1.4
Hex2long	2.1
Hex2short	1.5
Rec1long	2
Rec1short	1.4
Rec2long	1.9
Rec2short	1.5
Circ1long	2
Circ1short	1.4
Circ2long	2.1
Circ2short	1.4

A major cause of erroneous results in a typical Hopkinson Bar experiment is interfacial friction. Friction at the interface of the specimen-incidence bar and the specimen-transmitter bar causes the ends to be constrained against free expansion and creates a state of non-uniform triaxial stress in the specimen. Analysis and minimization of friction in Hopkinson Bar experiments has been an active field of research **[2.27, 2.28, 2.29, 2.30]**. Interfacial friction is highly dependent on the material to be tested. In the current investigation, the methods of

reducing interfacial friction for metallic specimens, as suggested by Hartley *et. al.* **[2.30]** are adopted and are briefly summarized. The rationale behind each of the following steps is beyond the scope of current discussion and only the key points are summarized.

(i) The ends of the incidence and transmission bar were polished using a 600-grit SiC paper.

(ii) The specimens were polished in a random fashion using a 1200-grit SiC paper

(iii) A thin layer of Molybdenum Disulfide lubricant was applied at the ends of the bar, to avoid heavy lubrication.

(iv) While sandwiching the sample, it was ensured that the sample is free to slide.

Having adopted the above mentioned measures to minimize the effects of inertia (due to the choice of the model material), non-uniform stress-distribution in the specimen (by appropriate choice of specimen length) and interfacial friction (by suitable lubrication methods and choosing appropriate specimen slenderness ratio), the samples were tested at nearly constant strain-rates to study the effect of specimen geometry. To ensure that all the samples were subjected to almost the same strain-rates, irrespective of the different length of each sample, different projectile lengths (ranging from 203.2 mm and 101.6 mm) were adopted and different pulse shapers were used for pulse-shaping. The strain-rate adopted was in the range of 1100-1400/s. The specimens were sandwiched between two high-strength steel bars, each of which was 1.8288 m (6 ft) long and 15.875 mm (5/8 inch) in diameter. The responses were measured with electrical resistance strain gages, bonded to the middle of the incident and transmitter bars, connected to Vishay Signal Conditioning Amplifiers (Model 2310B); and the response from the strain gages were recorded on a LeCroy digital oscilloscope (Model 354A). Equations (1) through (3) were then used to obtain the time-resolved stress and strain history in the specimen.

2.3 Results and Discussions

2.3.1 Effect of Specimen Length

The first effect of specimen length that was investigated was the condition of force equilibrium on both ends of the specimen. It was found that good equilibrium exists at both the end faces. The variation of axial forces with time on both ends of the specimen, Rec2long, is plotted in Figure 2.3.

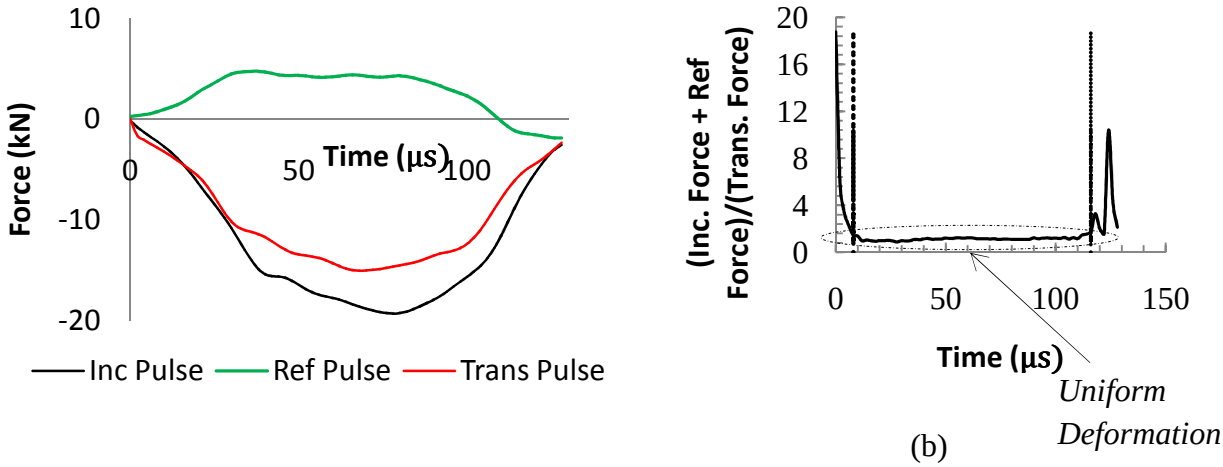

Figure 2.3. Check for axial equilibration of the Specimen (a) The pulses measured from the strain-gage readings (b) Plot of Ratio of Forces at the Incidence Face over Transmitter Face

The specimen was found to attain axial equilibrium in approximately 10 microseconds for a pulse that was over 100 microseconds in duration. Table 2.3 summarizes the equilibrium time as measured from strain-gage data in the specimens.

Table 2.3: Axial Equilibrium time in Specimens

Specimen	**Equilibrium Time as Measured from Strain-Gages (μs)**	**Equilibrium Time predicted from Equation (6) (μs)** *(Approximated at First Decimal Place)*
Hex1long	10	12
Hex1short	6	8
Hex2long	8	9
Hex2short	6	7
Rec1long	6	7
Rec1short	4	5
Rec2long	10	12
Rec2short	8	9
Circ1long	12	14
Circ1short	8	10
Circ2long	10	12
Circ2short	8	8

Dynamic stress-strain curves of each type of specimen are shown in Figure 2.4. It was found that except for the initial rising part of the curve (which is generally not of much concern in a Hopkinson Bar experiment due to effects of varying strain-rate), there is no drastic effect of specimen length of a given cross-section on the dynamic stress-strain curve of the specimen (at least after a strain of 0.01) and the stresses are within 4% of each other.

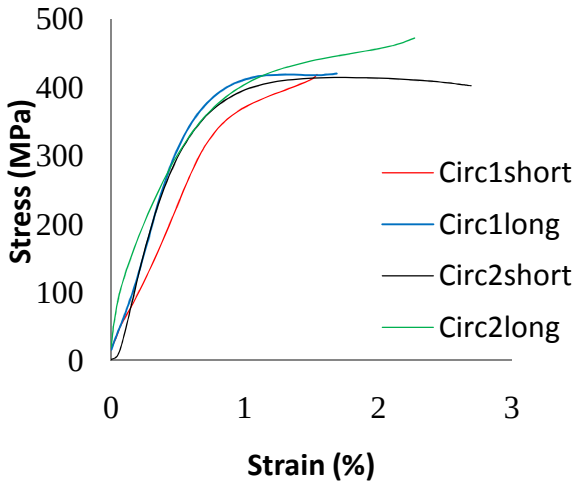

(a)

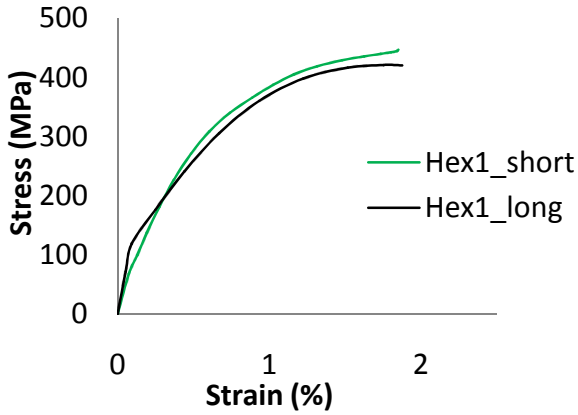

(b)

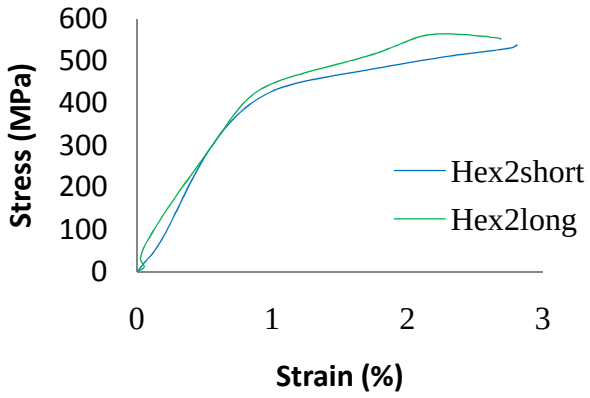

(c)

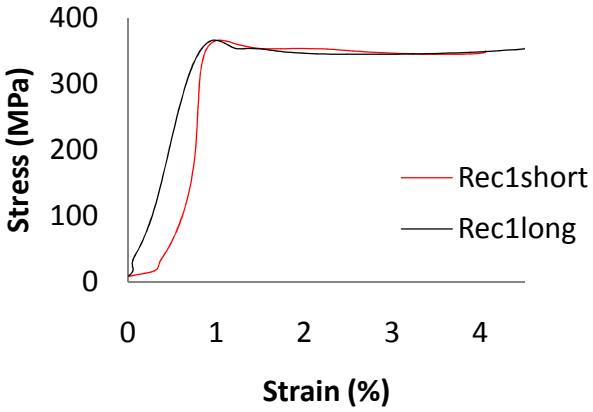

(d)

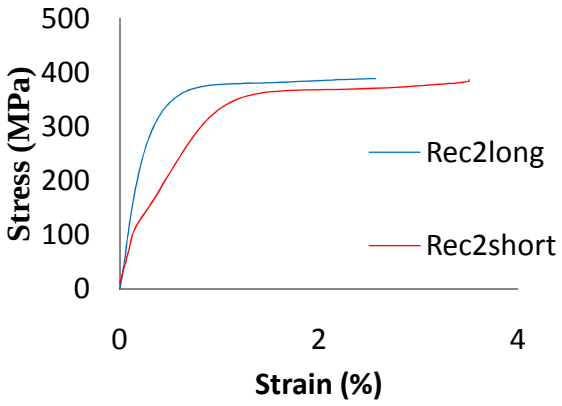

(e)

Figure 2.4. Effect of Change of Length of (a) Circ1&Circ2 (b) Hex1 (c) Hex2 (d) Rec1 (e) Rec2

2.3.2 Effect of Specimen Cross-Section

The influence of specimen cross-sectional shape is now studied to see the effects of deviating from a cylindrical to a non-cylindrical specimen. A comparison of the stress-strain curves of specimens with non-circular cross-sections to those with circular cross-sections is shown in Figure 2.5.

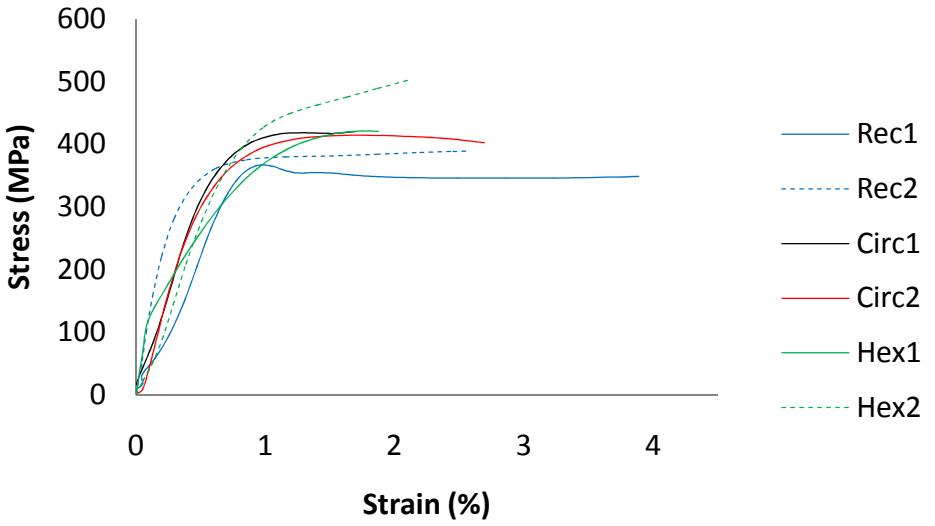

(a)

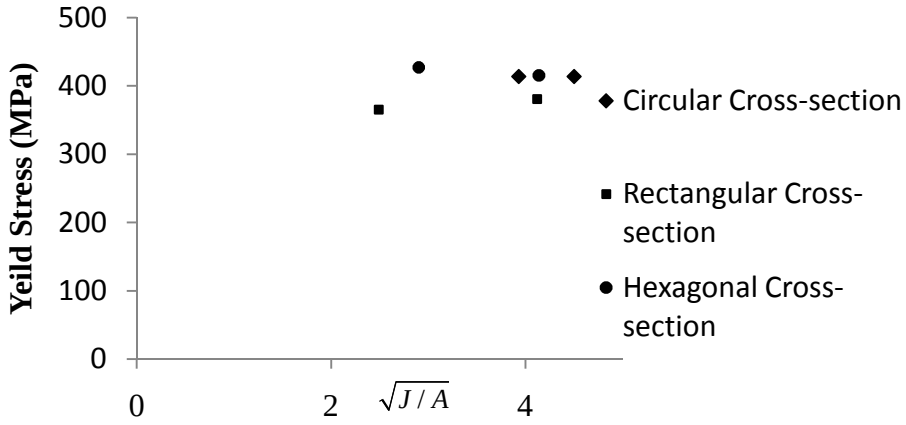

(b)

Figure 2.5. Comparison of Stress-strain Curves of Specimens of Different Cross-sectional Shapes (a) The Stress-strain Curves (b) Comparison of Yield Stress

From Figure 2.5, it can be seen that the rectangular samples slightly underestimate the yield stress in the sample, however, the deviation of yield stress of a rectangular specimen from a cylindrical one remains within 10%. The specimen geometry is thus found not to affect the dynamic characteristic curves drastically, provided the specimen slenderness ratio is guided by Equations (2.9) and (2.10), and interfacial friction is properly taken into consideration. In the ensuing section of the investigation, the assumption of stress-uniformity along the cross-section of the specimen has been investigated.

2.4 Analysis of Stress-Uniformity along the Cross-section of the Specimen

A Hopkinson Bar experiment rests on the fundamental assumption that the stress in a specimen is uniaxially uniform **[2.16]**. While this assumption is quite trivial when using cylindrical specimens in combination with cylindrical bars, this may become a concern when experiments are performed using non-cylindrical specimens in combination with round bars. This section of the investigation is aimed at studying and quantifying the effects of sharp edges in the specimen on the assumption that the specimen stress is uniaxially uniform based on numerical studies using a commercial Finite Element Software ABAQUS 6.8. An explicit analysis is performed with the use of 8-noded linear brick elements with reduced integration and hour-glass control (C3D8R). The effect of friction has been neglected at the specimen-bar interfaces and frictionless tangential contact conditions are used at the specimen-bar interfaces. In the current modeling, four types of specimen were chosen: a cylindrical sample with diameter 4mm, a hexagonal sample with edge size 4.5mm, a rectangular sample with edge size 4mm x 12mm, and a square sample with edge size 10 mm. A trapezoidal load was given in the form of distributed pressure at one face of the incidence bar. Figure 6 shows a typical model of the entire assembly and the load given at the incidence face.

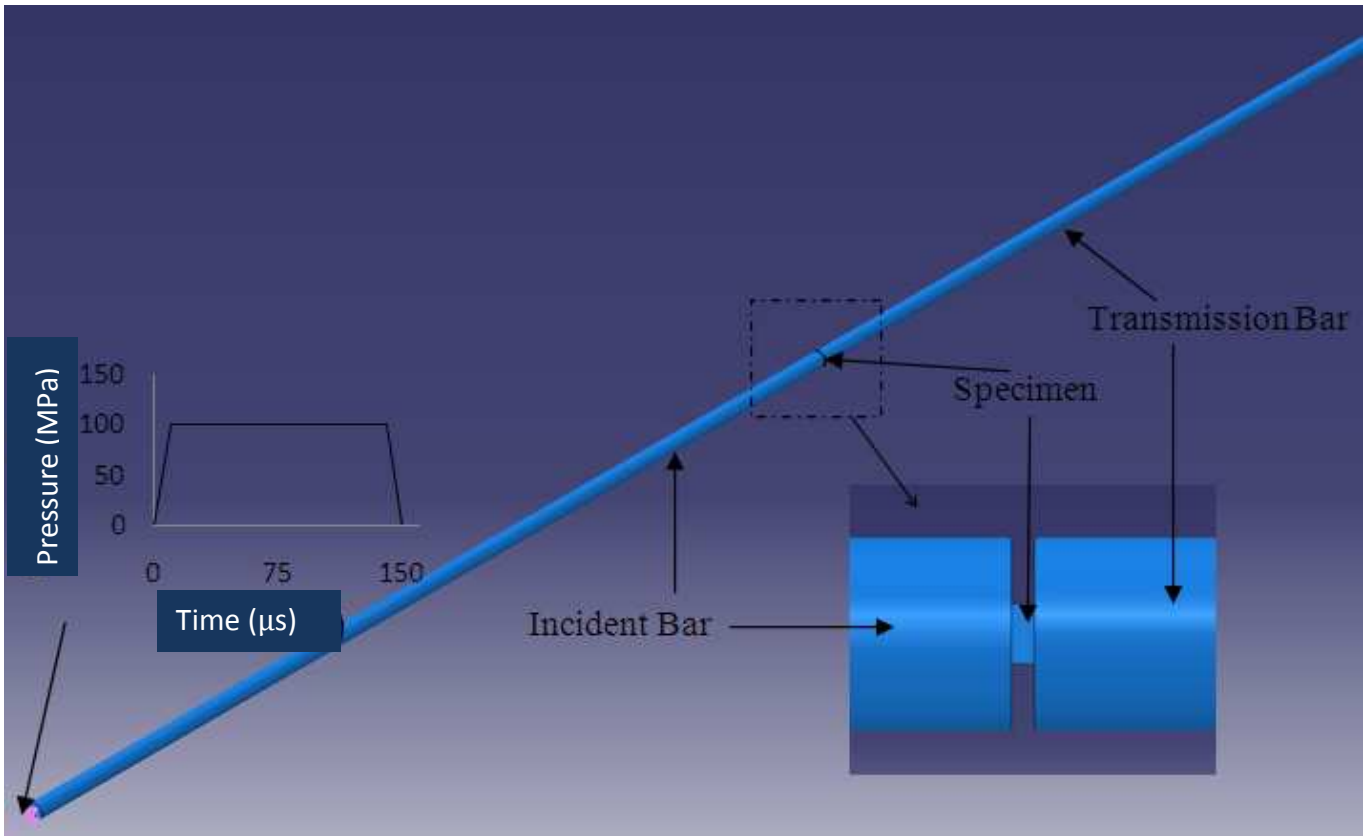

Figure 2.6 A Model of the SHPB Assembly Developed in ABAQUS

The axial stress was calculated at the centroid of each element at the incidence face. It was osbserved that there is a variation of stresses in the specimen owing to stress concentration at the sharp edges when using non-circular specimens. In a study by Pankow *et.al.* **[2.14]**, it was shown that the non-uniformity of stresses along the specimen cross-section due to the presence of sharp edges is small in magnitude. If the standard deviation of the stresses of all the elements in the cross-section of the specimen is calculated to quantify the amount of variation of stress along the specimen cross-section, it can is found that not only is this value small (within 10% of the flow stress of the material), but also the variation of stresses in the specimen is temporal and diminishes with time. In Figure 2.7, the axial stress-distribution in the incidence-face 8 microseconds after the incidence wave has reached the specimen is shown.

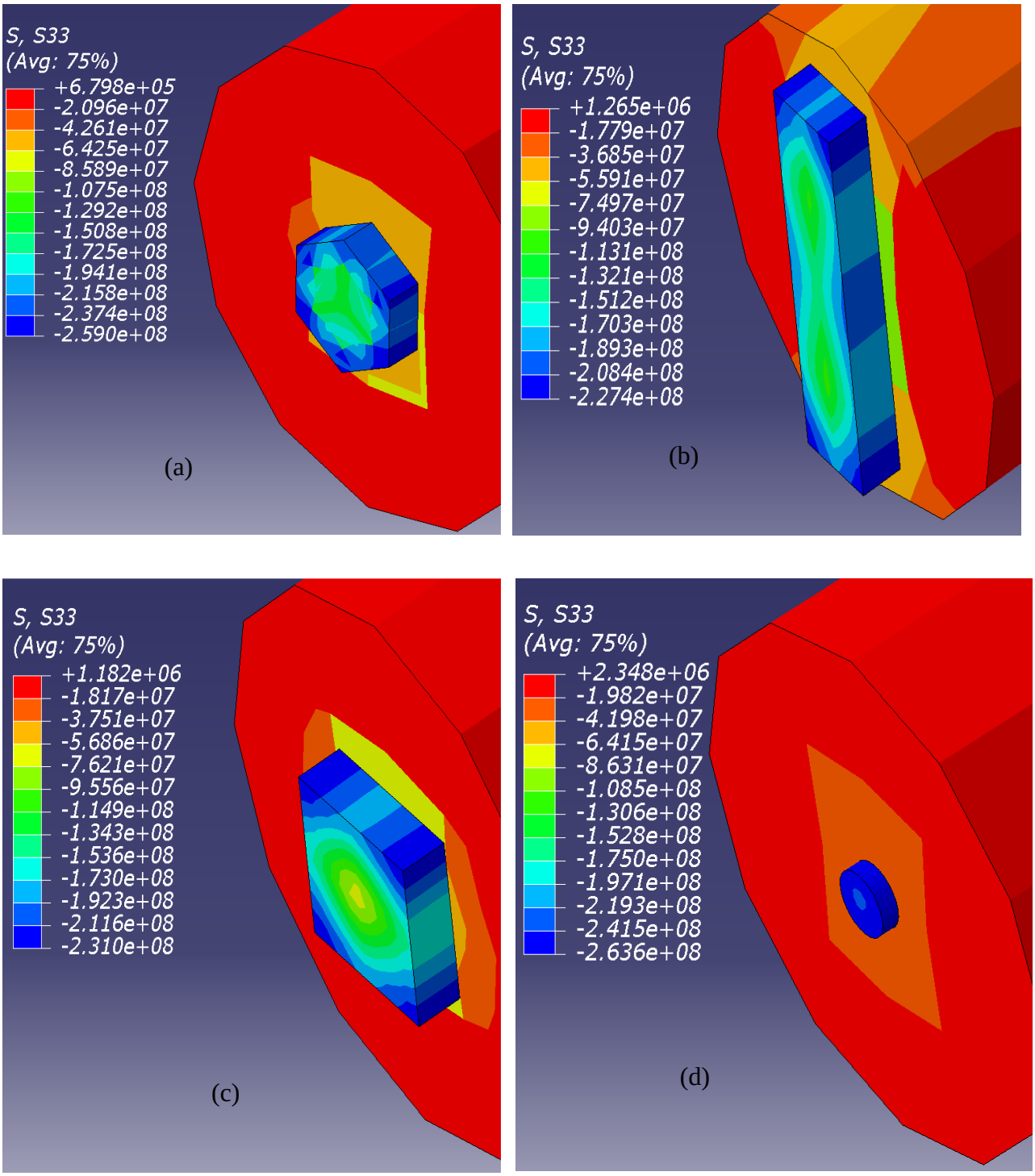

Figure 2.7. Axial Stress Distribution in the Specimen with Cross-Section of (a) Hexagon, (b) Rectangle, (c) Square, and (d) Circular 8 microseconds after the incident wave has reached the sample

Thus, the condition of uniaxially uniform specimen stress is satisfied not instantly but after a certain time. It was further observed that in the case of non-cylindrical specimen, the time for the stress-uniformity along the sample cross-section (referred to as the lateral equilibrium time) is dependant on the specimen cross-section's J / A value. This relationship is plotted in Figure 2.8

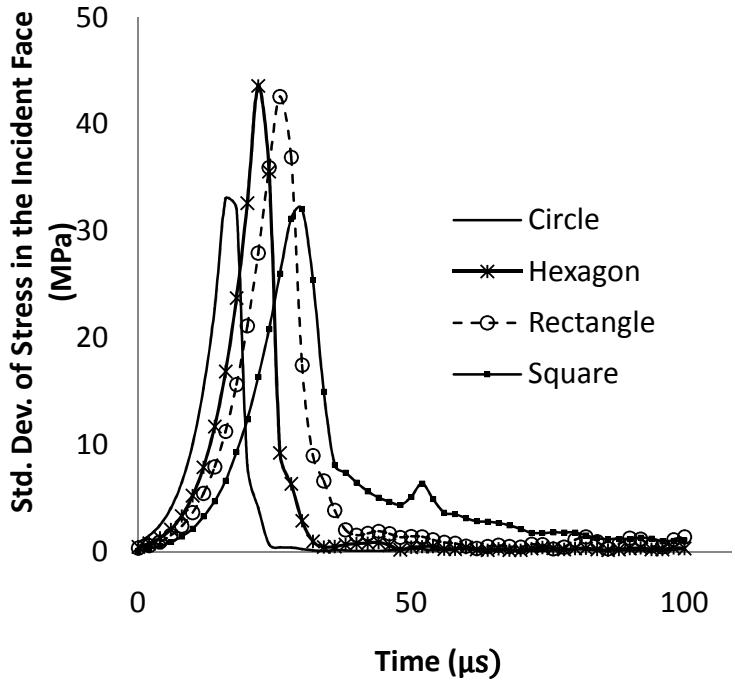

(a)

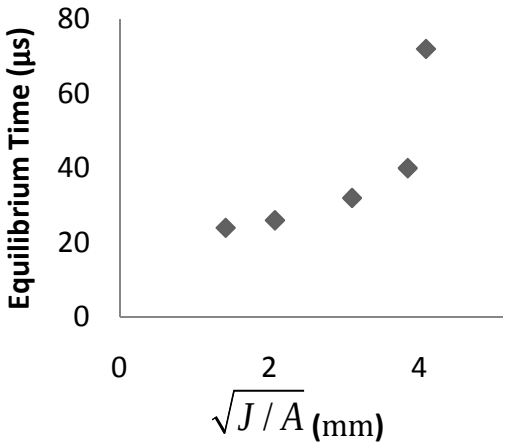

(b)

Figure 2.8 (a) Standard Deviation of Stresses in the Incident Face of the Specimen for Different Types of Specimens and, (b) Lateral Equilibrium Time v/s Specimen Cross-section Property in a Kolsky Bar Experiment

The above shows that the time for lateral equilibrium of stresses in a specimen increases with an increase of the specimen's J / A value of the cross-section. The higher the J / A value, the more is the time needed for the specimen to attain lateral equilibrium.

2.5 Conclusion

In the current investigation, the feasability of using non-cylindrical specimens in a Split-Hopkinson Pressure Bar was discussed. A general characteristic specimen cross-sectional dimension, $\sqrt{J/A}$, was shown to be a prudent choice and a critical slenderness ratio was established as an extension of the slenderness ratio established for cylindrical specimens. It was shown that if the specimen slenderness ratio is as dictated by the established criterion, there is negligible effect of specimen cross-section or length on the dynamic stress-strain curve. It was also shown that in a specimen with sharp edges, the effects of stress-concentration is temporary and diminishes with time.

CHAPTER 3

ON THE DETERMINATION OF DYNAMIC STRENGTH OF SINGLE LAP JOINTS USING THE SPLIT HOPKINSON PRESSURE BAR

3.1 INTRODUCTION

The use of adhesive bonded lap joints has gained increasing attraction due to their increasing use in aerospace structures, civil engineering applications, automotive industries, marine applications. These joints are easy to manufacture, cost-effective and compared to bolted joints, suffer lesser stress-concentration. An excellent summary of the relative advantages of adhesive bonded lap joints over other methods of structural joining is given in a recent publication by Osnes and McGeorge **[3.1]**.

Due to the variety of loads that a structural joint may be subjected to in different applications, the understanding and determination of the dynamic strength of adhesive bonded lap joints has been an active field of study. A dynamic wave propagation study on adhesive bonded lap joints has been conducted by Zachary and Burger **[3.2]** using photoelastic analysis. The failure of lap joints under transverse impact has been studied by Park and Kim **[3.3]**, where the total damage energy was estimated by firing a projectile onto the center of the target using a gas gun. A computational analysis of the process, together with experimental investigation suggested the existence of threshold energy after which sudden failure was observed. Their investigation focused on simulating a joint subjected to ice impact. A study of transverse impact of adhesive joints using a computational model by Vaidyaa *et. al.* **[3.4]** revealed that under transverse impact due to excessive deflection of the bonded area, failure occurred from the edges. The failure was attributed to peeling of the adhesive bond from the ends. In similar wave-propagation studies was by Higuchi *et. al.* **[3.5,3.6]**, the effect of Young's Modulus of the adherends, overlap length and adherend thickness on the maximum stress of the adhesive was investigated. The study of adhesive failure due to in-plane loading under low velocity impact has been studied by Rao *et.*

al.**[3.7]** In their study, a finite element modal analysis was used to predict the vibration frequencies of the adhesive layer. In a study of adhesive bonded joints using an instrumented impact pendulum, Goglio and Rosetto **[3.8]** reported the increase in strength of adhesives under impact loading. In a wave-propagation study by Sato and Ikegami **[3.9]**, the impact behaviour of lap joints and scarf joints under impact load was studied by proposing a viscoelastic model for the cured adhesive. Their study reflected that there was considerable stress-concentration at the edges.

The determination of the impact strength of adhesive bonded lap joints is described in ASTM D-950 03 **[3.10]**. The standard recommends the use of a pendulum impact test for the determination of the same. A critical analysis of this was performed by Adams and Harris **[3.11]** and it was concluded that such a method was more suitable for giving only a comparative estimate.

For determining the impact strength of adhesive bonded lap joints, a commonly used loading device is the Split Hopkinson Pressure Bar (Kolsky Bar). For determining the strength of adhesive lap-joints using a Kolsky Bar, the specimen is designed such that the one-dimensional axial forces in the incidence bar give a pure shear force to the adhesive-bonded test assembly. It is further assumed that the only compliance in the test-assembly is due to the adhesive bond between the substrates and force is transmitted onto the transmission bar only as long as the adhesive bond does not fail. A variety of different specimen designs have been adopted by various researchers for determination of the strength of adhesive bonded joints. Srivastava *et. al.* **[3.12]** used a split cylinder lap joint specimen to investigate the dynamic strength of adhesive bonded lap joints. Yokoyama and Shimizu **[3.13]** determined the strength of an adhesive bonded lap joint using a pin and collar specimen. Yokoyama and Nakai **[3.14]** used a hat-shaped

specimen sandwiched between an incidence bar and a hollow transmission bar, where the diameter of the transmission bar was larger than that of the incidence bar. For elevated temperature tests on adhesive-bonded single lap joints, Adamvalli and Parameswaran **[3.15]** used two short plates which were bonded by adhesive and the test-assembly was sandwiched between the incidence and transmission bar. The maximum force, as calculated from the strain gage on the transmission bar, was used to estimate the failure strength of the adhesive joint at different temperatures. Similar specimen and test method was used by Chen and Li **[3.16]** to study the strength degradation of adhesive bonded single lap joints with temperature, using a tensile Split Hopkinson Bar. Raykhere *et. al.* **[3.17]** used a torsional Split Hopkinson Bar to study the impact strength of adhesive butt joint.

Closed form solutions for adhesive bonded lap joints under quasi-static loading was first developed in a classical work by Volkersen **[3.18],** which have been extended subsequently by Goland and Reissner **[3.19]** and de Bruyne **[3.20]** to include peel effects, Hart-Smith to include the effects of inelastic adhesive deformation **[3.21]**, Tsai *et. al* **[3.22]** to include the effects of shear deformation of the adherend, Osnes and McGeorge **[3.1]** to combine the effects of both inelastic deformation of the adhesive and shear deformation of adherends and by Chataigner *et. al.* **[3.23]** to propose a non-linear failure criterion for adhesive bonded double lap joints. Other detailed studies on this have been conducted by various researchers [**3.24-3.46]**, however, the research has been limited to quasi-static cases.

In a research by Srivastava *et. al.*, **[3.47]** the effect of the bonding length and thickness on the strength of adhesive bonded lap joint has been reported using the split cylinder lap joint. The aim of the current research is to investigate and report the drastic effect of the bonding area on the dynamic strength of adhesive bonded lap joints using the split cylinder lap joint specimen for

experiments in a Split Hopkinson Pressure Bar and develop a mathematical rationale for the same. In a Kolsky Bar experiment, an adhesive bonded lap joint is subjected to different rates of loading. In the current research, the proposed model of Osnes and McGeorge has been extended to include the effects of strain acceleration as well as out-of-plane adherend thickness in a single lap joint, thereby enabling direct comparison of the proposed model with the experimental results obtained from a Kolsky Bar. The theory can easily be extended to the case of a double lap joint.

3.2 Dynamic Experiments

3.2.1 Description of Samples and Experimental Procedure

The split cylinder sample suggested by Srivastava *et. al.* [**3.12**] comprises two cylinders which were cut along the longitudinal axis of symmetry. The cut faces were used for bonding the specimens with a thin layer of Loctite Fixmaster® High Performance Epoxy (99393), which is a two-part epoxy adhesive with a mix-ratio of 1:1. The shear modulus of the adhesive being not provided by the manufacturer, an estimate of the shear modulus of the same was obtained from 5 different two-part epoxy adhesives of the same family and was estimated to be 1200 MPa. The bonding faces of adherends were polished using a 600 SiC grit, followed by 1300 SiC grit, cleaned with a phosphoric acid surface cleaner, followed by neutralizing with ammonia water. The surface cleaner and the neutralizer were obtained from Vishay Micro-measurements. The bonded assembly was then cured at room temperature for 24 hours before performing experiments. The process resulted in near uniform adhesive layer with a thickness of 0.5 mm.

Two types of split cylinder specimens were taken in the current investigation, one having a diameter (d) exactly equal to the diameter of the incidence and transmission bars (15.9 mm) and the other having a slightly smaller diameter (12.7 mm). In each case, two different overlap length (xl) were adopted, one being 10 mm and the other being 15 mm. A small gap was left at either

ends of the overlap length to ensure load transfer through adhesives only. In addition, for each of the sample, a small flange was left for proper centering in order to minimize the effects of bending and associated peel stress. The flange was of the same diameter as the split cylinder, without the axial cut. The material for the adherend was same as that of the Hopkinson Bars. (Aluminum Alloy 7075). Over 50 experiments were conducted to ensure that the results had a well-defined error bar. Figure 3.1 shows a diagram of the specimen adopted.

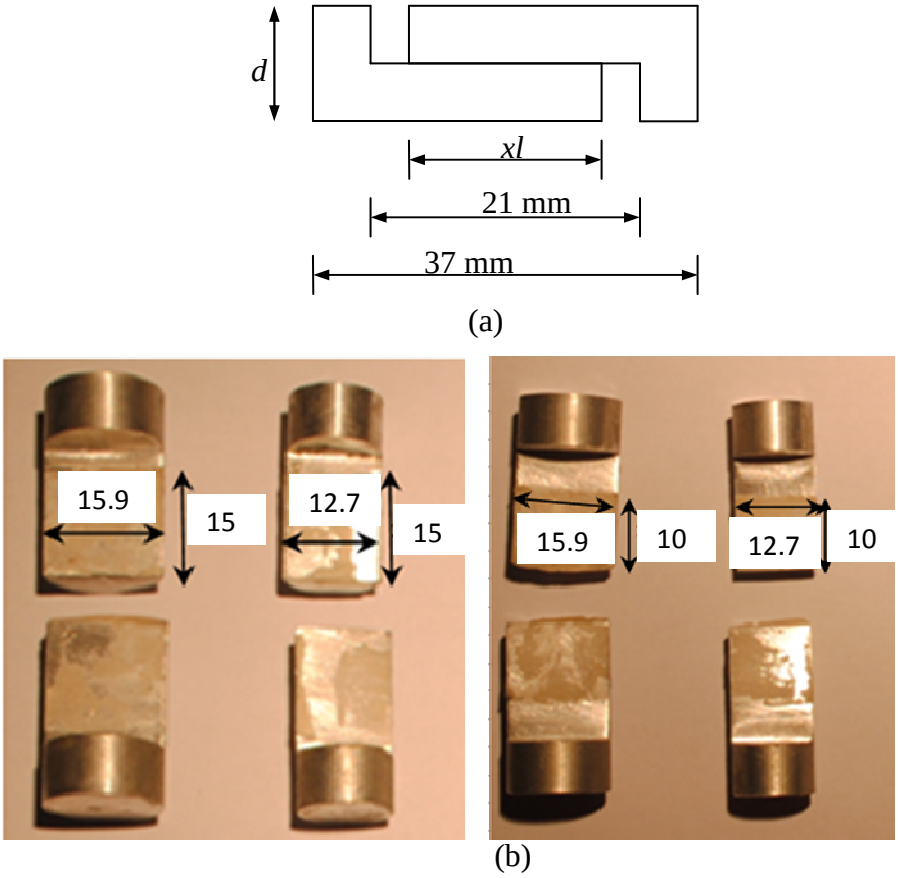

Figure 3.1 (a) Schematic representation of the specimen adopted in the current experiment

(b) Specimens adopted in the current experiment

Table 3.1. Details of the specimen adopted

Name	Overlap Length (x_l) (mm)	Diameter *(d)*(mm)	Overlap Area (A), (mm^2)
1	15	15.9	238.5
2	10	15.9	159
3	15	12.7	190.5
4	10	12.7	127

Both quasi-static and dynamic experiments were performed for the samples adopted. The quasi-static experiments were performed using an MTS-810 Material Testing System with a cross-head speed of 0.5mm/s. The maximum load to failure was recorded, and then divided by the over-lap area to estimate the shear strength of the joint. For the dynamic experiments using the Split Hopkinson Pressure Bar, the specimens were sandwiched between two high strength Aluminum (Alloy 7075) bars, each of which was 1.8 m (6 ft) long and 15.9 mm (5/8 inch) in diameter. The responses were measured with electrical resistance strain gages, bonded to the middle of the incident and transmitter bars, connected to Vishay Signal Conditioning Amplifiers (Model 2310B); and the response from the strain gages were recorded on a LeCroy digital oscilloscope (Model 354A). To ensure that the samples were subjected to different loading-rates, different projectile lengths (ranging from 203.2 mm and 76.2 mm) were adopted and different pulse shapers were used for pulse-shaping. The following section discusses the calculation of joint-strength from the SHPB technique.

3.2.2 Calculation of Joint Strength

The SHPB technique comprises a specimen, which in this case comprises two adherends with a thin layer of adhesive between them, sandwiched between two cylindrical bars called the incidence bar and the transmission bar. The cross-sectional geometry of these two bars is, in

general, the same and they are made of the same material. An axial impact on the incident bar is caused by firing an air gun, which in turn generates a travelling compressive wave in the incident bar. The material and the cross-section of the specimen is not the same as that of the incidence bar, partially due to the presence of the thin layer of adhesive between the adherend, and partially due to area mismatch between the adherend and the incidence bar. Hence, due to the mismatch of mechanical impedance of these two, when the travelling wave hits the specimen, a part of it is reflected back into the striker bar and a part of it is transmitted through the specimen. The transmitted wave impinges on the transmission bar after travelling through the specimen and travels forth as a travelling wave, while a part of it is reflected back into the specimen. If the specimen is short enough compared to the length of the stress pulse, then it is assumed that stress equilibrium is achieved due to several reflections within the specimen in a time much shorter than the duration of the test. If $\varepsilon_i, \varepsilon_r, \varepsilon_t$ denote the incidence, reflected and transmitted strain waves respectively, $\sigma_1(t), \sigma_2(t)$ denote the stresses at the specimen-incidence bar and the specimen transmission bar respectively, $P_1(t), P_2(t)$ denote the forces at the specimen-incidence bar and the specimen transmission bar respectively, A_b, E_b be the cross-sectional area and Modulus of Elasticity of the transmission/incidence bar respectively and A_{ls} be the bonded area of the adhesive lap joint, then the following relations hold **[3.12]**:

$$P_1(t) = A_b \sigma_1(t) = A_b E_b \{\varepsilon_i(t) + \varepsilon_r(t)\} \tag{3.1}$$

$$P_2(t) = A_b \sigma_2(t) = A_b E_b \varepsilon_t(t) \tag{3.2}$$

$$\tau_s = \frac{P_2(t)_{\max}}{A_{ls}} \tag{3.3}$$

where τ_s is the shear strength of the joint and $P_2(t)_{\max}$ is the maximum transmitted load through the adhesive lap joint. In the current investigation, the loading-rate, $\dot{P}$, is calculated from the slope of the transmitted force, i.e.

$$\dot{P} = \frac{dP_2(t)}{dt} \tag{3.4}$$

Figure 3.2 shows a representative plot of the incidence, reflected and transmission pulses obtained from the experiments.

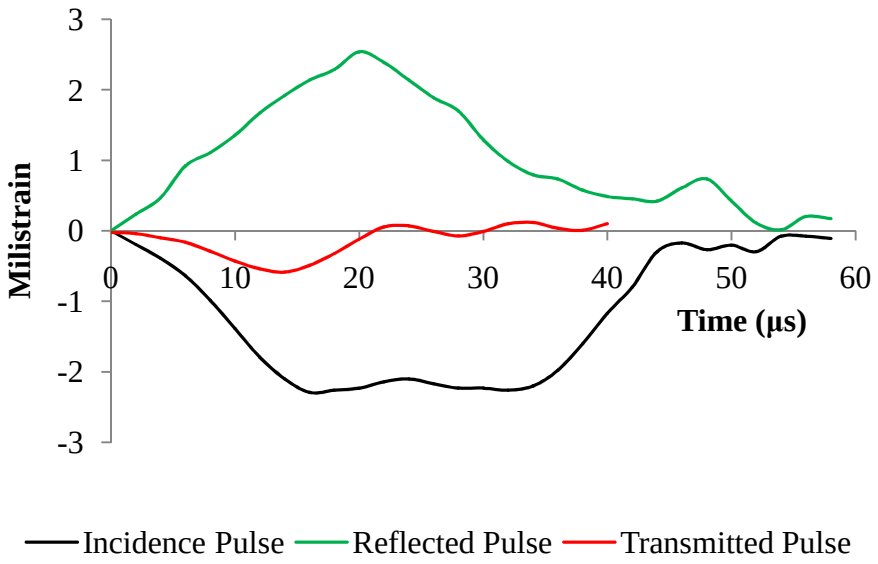

Figure 3.2: Typical Pulses obtained in the Kolsky Bar Experiment

3.3Analytical Model for Shear Strain in Single Lap-Joints

3.3.1 Governing Equation

This section aims at deriving a mathematical model for estimating the strength of an adhesive-bonded single lap shear joint, by extending the recently proposed model for adhesive-bonded double lap joints of **Osnes and McGeorge [3.1]** to include the effects of shear strain acceleration of the adhesive and out-of-plane thickness of the adherend. The adhesive is idealized to execute brittle, elastic behavior, as has been experimentally indentified to be the

typical behavior at high loading rates **[3.2]**. The current analysis rests on the "shear lag" theory of Volkersen **[3.18,3.23]**. The assumptions involved are as follows

- The adherends are linear elastic
- The axial stress is constant throughout the adherend thickness
- Shear stress is constant throughout the adhesive thickness
- Peeling stresses are negligible.

Figure 3.3 shows the schematic representation of the assembly of the adhesive bonded single lap joint.

For the split cylinder samples adopted in the current investigation, the out-of-plane adherend thickness is not constant. The equations of motion for the outer and inner adherend may therefore be written as follows.

For the outer adherend,

$$\left(T_0+\partial T_o\right)-T_0+2\tau_a r\partial x=\rho\left(\frac{\pi}{2}r^2\partial x\right)a_o \tag{3.5a}$$

$$\therefore\frac{\partial T_o}{\partial x}+2\tau_a r=\left(\frac{\pi}{2}r^2\right)a_o \tag{3.5b}$$

For the inner adherend,

$$\left(T_0+\partial T_o\right)-T_0-2\tau_a r\partial x=\rho\left(\frac{\pi}{2}r^2\partial x\right)a_i \tag{3. 6a}$$

$$\therefore\frac{\partial T_i}{\partial x}-2\tau_a r=\left(\frac{\pi}{2}r^2\right)a_i \tag{3. 6b}$$

In the above equations, T_0, T_i represent the axial stress-resultant (positive in tension) of the outer and inner adherend respectively, ρ is the density of the adherends, τ_a is the adhesive

shear stress, a_i, a_0 represent the average acceleration of the cross-section of the inner and outer adherend respectively and r is the radius of the split cylinder specimen adopted.

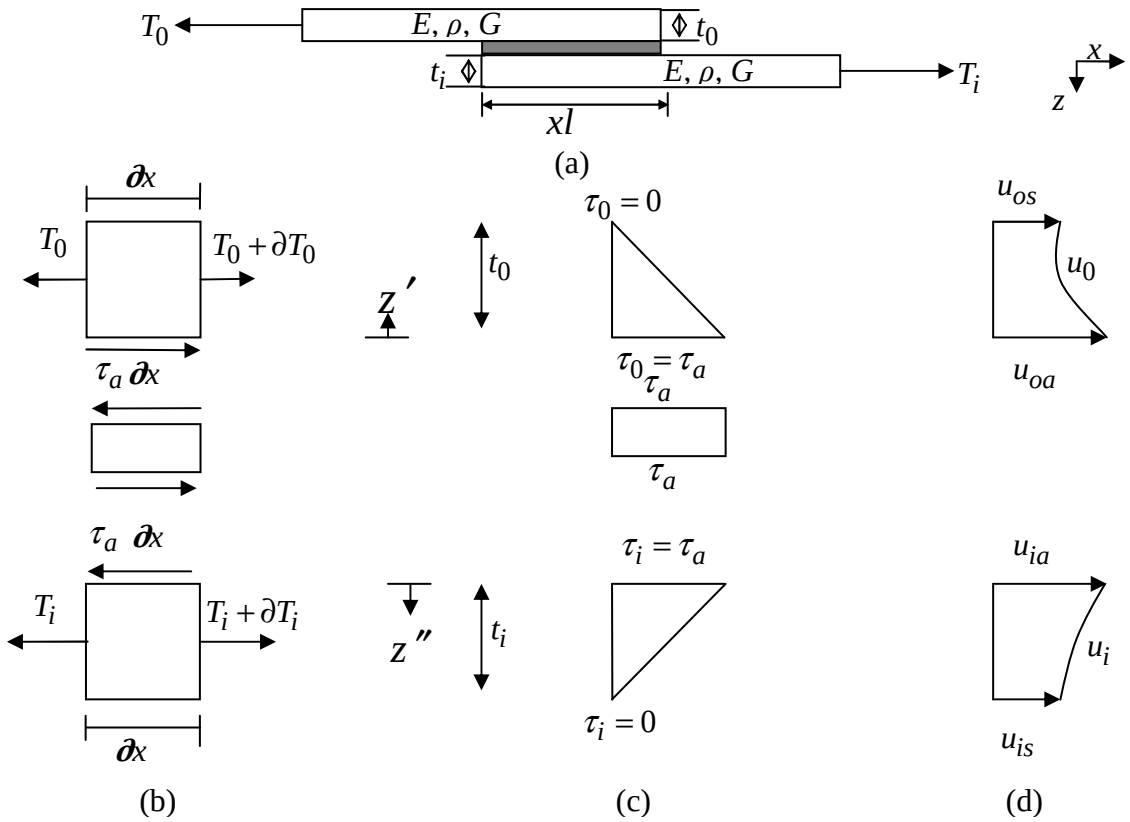

Figure 3.3 (a) Schematic representation of the adhesive bonded lap joint assembly (b) Free-body diagram of the adherends and adhesive layer (c) variation of shear stress in the through-thickness direction of the adherends and (d) displacement profile in the through-thickness direction of the adherends

If $\tau_0(x, y, z')$ and $\tau_i(x, y, z'')$ represent the shear stress in the outer and inner adherends respectively, where z', z'' are local origins as defined by figure 3.3, τ_a is the shear stress at the junction of the adhesive and the adherends, and $t_0(y), t_i(y)$ are the thickness of the outer and inner adherend respectively, then from the assumption of linear variation of shear stress throughout the adherend thickness,

$$\tau_o = \tau_a \left[1 - \frac{z'}{t_o(y)} \right] \tag{3.7a}$$

$$\tau_i = \tau_a \left[1 - \frac{z''}{t_i(y)} \right] \tag{3.7b}$$

Let γ_o, γ_i represent the shear strain in the outer and inner adherends respectively and *G* be the shear modulus of the adherends. Then, Equations 3.7(a) and 3.7(b) can be written as

$$\gamma_o = \frac{\tau_a}{G} \left[1 - \frac{z'}{t_o(y)} \right] \tag{3.8a}$$

$$\gamma_i = \frac{\tau_a}{G} \left[1 - \frac{z''}{t_i(y)} \right] \tag{3.8b}$$

From Equations 3.8(a) and 3.8(b), the equations for horizontal displacements may be written as

$$u_o = u_{oa}(x,t) + \frac{\tau_a}{G t_o(y)} \frac{z'^2}{2} - \frac{\tau_a}{2G} t_o(y) \tag{3.9a}$$

$$u_i = u_{ia}(x,t) + \frac{\tau_a}{G} \left[z'' - \frac{z''^2}{2 t_i(y)} \right] \tag{3.9b}$$

where u_o and u_i are the horizontal displacements of the outer and inner adherends respectively and u_{oa} and u_{ia} are the horizontal displacements at the interface of the adhesive layer and the outer and inner adherend respectively. The axial strain in the outer and inner adherends, $\varepsilon_{xo}, \varepsilon_{xi}$ thus become

$$\varepsilon_{xo}(x, y, z', t) = \frac{\partial u_{oa}}{\partial x} + \frac{z'^2}{2G t_o(y)} \frac{\partial \tau_a}{\partial x} - \frac{t_o(y)}{2G} \frac{\partial \tau_a}{\partial x} \tag{3.10a}$$

$$\varepsilon_{xi}(x,y,z'',t)=\frac{\partial u_{ia}}{\partial x}+\frac{z''}{G}\frac{\partial \tau_a}{\partial x}-\frac{z''^2}{2Gt_i(y)}\frac{\partial \tau_a}{\partial x} \tag{3.10b}$$

Noting that for a split-cylinder sample of radius *r*, $t_o=\sqrt{r^2-y^2}$, $t_i=\sqrt{r^2-y^2}$, the axial stress-resultants T_0 and T_i can be obtained as

$$T_0=E\int_{y=-r}^{r}\int_{\hat{z}'=0}^{z'}\varepsilon_{xo}(x,y,\hat{z}',t)d\hat{z}'dy \tag{3.11a}$$

$$T_i=E\int_{y=-r}^{r}\int_{\hat{z}''=0}^{z''}\varepsilon_{xi}(x,y,\hat{z}'',t)d\hat{z}''dy \tag{3.11b}$$

where *E* is the Modulus of Elasticity of the adherend. Performing the integration in Equation (3.11), and re-arranging the terms,

$$\frac{\partial u_{oa}}{\partial x}=\frac{2T_o}{E\pi r^2}+\frac{2r}{9G\pi}\frac{\partial \tau_a}{\partial x} \tag{3.12a}$$

$$\frac{\partial u_{ia}}{\partial x}=\frac{2T_i}{E\pi r^2}-\frac{2r}{9G\pi}\frac{\partial \tau_a}{\partial x} \tag{3.12b}$$

If the adhesive thickness is denoted by t_a and the shear strain of the adhesive by γ_a then, from the assumption of constant adhesive shear strain throughout the adhesive thickness,

$$\gamma_a=\frac{u_{ia}-u_{oa}}{t_a} \tag{3.13}$$

From Equations (3.12) and (3.13), it is therefore possible to show that

$$\frac{\partial T_i}{\partial x}-\frac{\partial T_o}{\partial x}=\frac{E\pi r^2}{2}\left\{t_a-\frac{4rG_a}{9G\pi}\right\}\frac{\partial^2\gamma_a}{\partial x^2} \tag{3.14}$$

Again, from Equations 3.9(a) and 3.9(b),

$$\hat{a}_o(x,y,z',t)=\frac{\partial^2 u_o}{\partial t^2}=\frac{\partial^2 u_{oa}}{\partial t^2}+\frac{z'^2}{2Gt_o}\frac{\partial^2\tau_a}{\partial t^2}-\frac{t_i}{2G}\frac{\partial^2\tau_a}{\partial t^2} \tag{3.15a}$$

$$\hat{a}_i(x,y,z'',t)=\frac{\partial^2 u_i}{\partial t^2}=\frac{\partial^2 u_{ia}}{\partial t^2}+\frac{z''}{G_i}\frac{\partial^2 \tau_a}{\partial t^2}-\frac{z''^2}{2G_i t_i}\frac{\partial^2 \tau_a}{\partial t^2} \tag{3.15b}$$

where $\hat{a}_o$, $\hat{a}_i$ represent the accelerations of the outer and inner adherends respectively. The average accelerations, a_0 and a_i can then be obtained from Equations (15) as follows

$$a_o(x,t)=\frac{\int_{y=-r}^{r}\int_{\hat{z}'=0}^{z'}\hat{a}_o(x,y,\hat{z}',t)d\hat{z}'dy}{\int_{y=-r}^{r}\int_{\hat{z}'=0}^{z'}d\hat{z}'dy}=\frac{\partial^2 u_{oa}}{\partial t^2}-\frac{2rG_a}{9G\pi}\frac{\partial^2 \gamma_a}{\partial t^2} \tag{3.16}$$

$$a_i(x,t)=\frac{\int_{y=-r}^{r}\int_{\hat{z}''=0}^{z''}\hat{a}_o(x,y,\hat{z}'',t)d\hat{z}''dy}{\int_{y=-r}^{r}\int_{\hat{z}''=0}^{z''}d\hat{z}''dy}=\frac{\partial^2 u_{ia}}{\partial t^2}+\frac{2rG_a}{9G\pi}\frac{\partial^2 \gamma_a}{\partial t^2} \tag{3.17}$$

From Equations (3.13), (3.16) and (17), it is possible to show that

$$a_i-a_o=\left\{t_a-\frac{4rG_a}{9G\pi}\right\}\frac{\partial^2 \gamma_a}{\partial t^2} \tag{3.18}$$

Subtracting Equation 3.6(b) from 3.5(b) and substituting equations (3.14) and (3.18), the governing differential equation of the system is obtained as

$$\frac{\partial^2 \gamma_a}{\partial x^2}-\frac{1}{c^2}\frac{\partial^2 \gamma_a}{\partial t^2}=\frac{1}{\alpha}\gamma_a \tag{3.19}$$

Here, α is a parameter depending on the material properties of the adherends and the adhesive as well on the structural properties of the bonded-lap joint, and is defined by

$$\frac{1}{\alpha}=\frac{72G_aG}{E\left(9G\pi r t_a-4r^2G_a\right)} \tag{3.20}$$

while *c* is the velocity of an elastic stress-wave of the adherend, defined by

$$c = \sqrt{\frac{E}{\rho}} \tag{3.21}$$

The initial conditions of the problem are given as

$$\gamma = 0; \frac{\partial \gamma}{\partial t} = 0 \quad \text{at } t = 0 \tag{3.22}$$

To obtain the boundary conditions of the problem, Equations (3.12) and (3.13) are combined to yield

$$\frac{\partial \gamma}{\partial x}\left\{1 + \frac{4rG_a}{9G\pi}\right\} = \frac{1}{t_a}\left\{\frac{2T_i}{E\pi r^2} - \frac{2T_o}{E\pi r^2}\right\} \tag{3.23}$$

$$\text{At } x = 0 \text{ , } T_i = 0; T_o = -F(t) \tag{3.24a}$$

$$\text{At } x = x_l \text{ , } T_i = -F(t); T_o = 0 \tag{3.24b}$$

Here, *F(t)* is the prescribed loading at the outer and inner adherends, the negative sign indicates that the nature of the load is compressive (as in the Kolsky Bar experiment), and the prescribed loading is taken to be equal at both the ends to ensure that the specimen is in a state of stress-equilibrium with minimal wave-propagation effects. x_l denotes the length of the overlap. Equations (3.23) and (3.24) form the boundary conditions to the governing differential equation, described by Equation (3.19). Equations (3.19), (3.22), (3.23) and (3.24) complete the definition of the current problem.

3.3.2Solution of the Governing Equation and Comparison with Experimental Observations

To solve Equation (3.19), the loading function *F(t)* was determined from the incidence pulse, measured directly from the strain-gage readings on the incidence bar, multiplied by the area of the incidence bar and the modulus of the incidence bar. Thus,

$$F(t) = -\psi A_b E_b \varepsilon_r(t) \tag{3.25}$$

where ψ is the transmission coefficient, taking into account the area mismatch between the incidence bar and the split-cylinder sample. Equation (3.19) was then solved numerically using the Galerkin Weighted-residual method, with the use of linear Lagrange Interpolation Functions for the spatial variation of the shear-strain in the joint and an explicit half-step central difference scheme for obtaining the temporal variation of shear strain in the joint. A user developed computational code was used for the calculation. The detailed derivation is included in the appendix. Once the adhesive shear strain was calculated, the average displacement, u_{avg} along the cross-section of the adherend was calculated by integration equation 3.9(b) along the cross-section of the inner adherend to yield

$$u_{avg} = \left[u_{ia}(x = x_l, t) + \frac{8rG_a}{9G\pi} \gamma_a(x = x_l, t) \right] \tag{3.26}$$

The strain in the adherend at $x = x_l$ was thus obtained as

$$\varepsilon_{xi}\left(x = x_l, t\right) = \frac{\partial u_{avg}}{\partial x} \tag{3.27}$$

From the condition of velocity compatibility of the inner adherend-transmission bar interface, it can be stated that the velocity of the inner adherend, v_{xi} and the velocity of the transmission bar, v_t are equal, i.e.:

$$v_{xi}(x = x_l, t) = v_t \tag{3.28a}$$

$$\therefore c\varepsilon_{xi}\left(x = x_l, t\right) = c_t \varepsilon_t \tag{3.28b}$$

where c_t is the velocity of stress-wave in the transmission bar. From Equation (3.28b), a prediction of the peak value of the strain in the transmission bar is possible .

3.4 **Results and Discussions**

From the readings on the strain-gages at the transmission bar, if the time taken to reach the peak load be taken as the time for the joint to fail, then the temporal variation of the strain in the adhesive till failure can be determined from the mathematical model. Figure 3.4 shows that the shear strain is maximum in the adhesive layer at the edges and that the strain progresses from the edges, straining more and more of the overlap length. Figure (3.5) shows the plot of shear strain distribution at failure for all the four types of specimen adopted at a loading rate of 0.65 kN/μs.

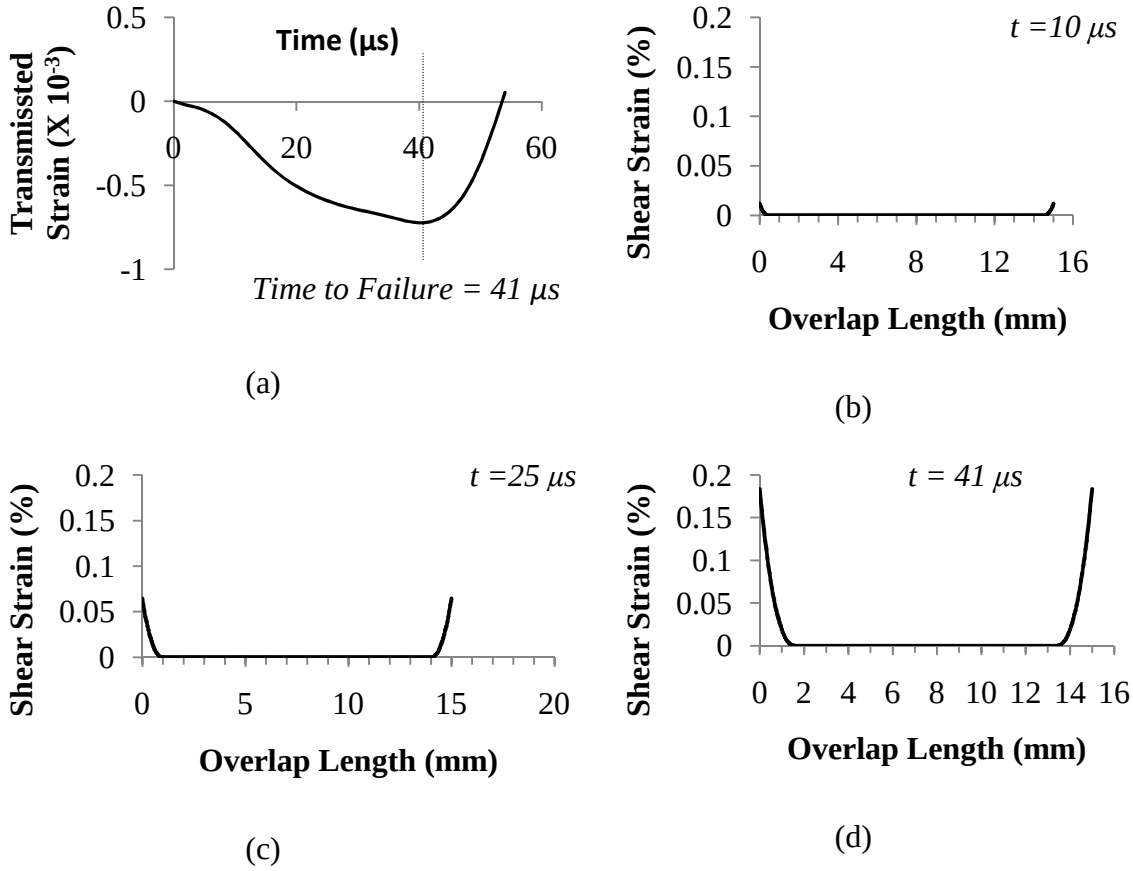

Figure 3.4 (a) Transmitted Pulse as obtained from Strain-gage (b) Shear Strain Distribution along the overlap length at 10 microseconds (c) Shear Strain Distribution along the overlap length at 25 microseconds (d) Shear Strain Distribution along the overlap length at the time of failure for specimen 3 at a loading rate of 0.65 kN/μs

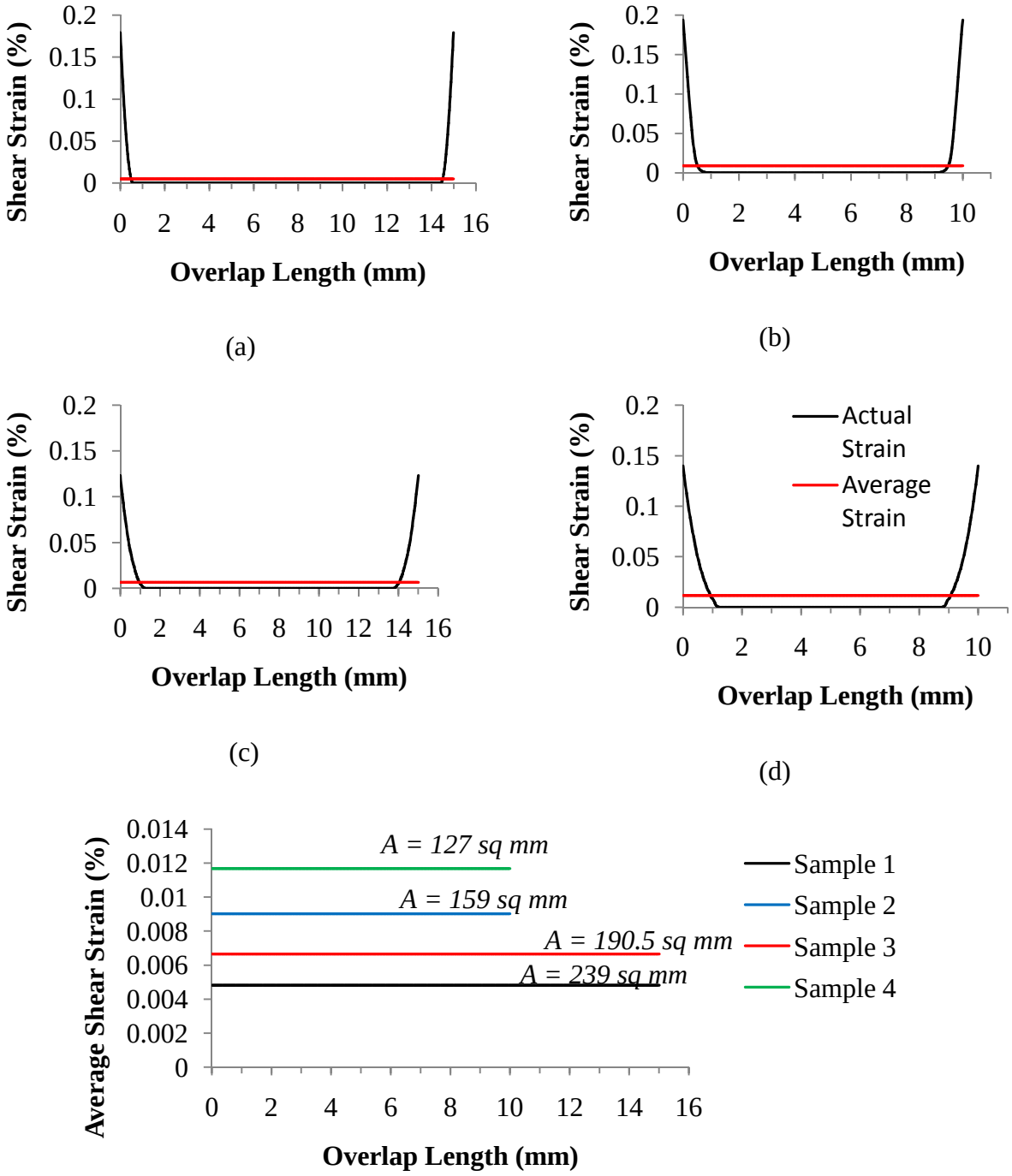

Figure 3.5. Plot of Shear Strain distribution in the adhesive layer over the overlap length for (a) Sample 1 (b) Sample 2 (c) Sample 3 (d) Sample 4 (e) Average Shear Strain at a rate of 0.65 kN/μs

Some immediate conclusions can be drawn from figure 3.5. They are as follows.

(i)Influence of overlap length for a given out-of-plane thickness: By comparing figures 3.5(a) and 3.5(b) or similarly figures 3.5(c) and 3.5(d), it can be seen that reducing the overlap length slightly increases the peak strain in the adhesive joint, however, the total length of non-zero strain at the time of failure remains the same. The effect on averaging the total strain over the entire overlap length results in an increased average value of strain for the case of reduced overlap length, as the fraction of area of non-zero strain over the entire overlap length is higher mainly due to the reduced overlap length in figures 3.5(b) and 3.5(d) in comparison to 3.5(a) and 3.5(c) respectively.

(ii) Influence of out-of-plane thickness for a given over-lap area: In contrast to case (i), if the in-plane thickness is reduced for a given overlap length, the maximum strain is decreased. This is due to the dependence of the term α on the out-of-plane thickness (in this case, the radius of the split cylinder sample) in the governing differential equation of the system as predicted by Equations (3.19) and (3.20). Nevertheless, it can be immediately observed by comparing figures 3.5(a) and 3.5(c) or figures 3.5(b) and 3.5(d), that as the out-of-plane thickness is reduced for a given overlap area, the length of non-zero strain at the time of failure increases considerably. It turns out that the increase in the length of non-zero strain more than compensates for the decrease in peak-strain value, resulting in an increase in the average strain over the overlap length. The net result is lower the out-of-plane thickness for a given overlap length, higher is the average shear-strain over the entire overlap length.

(iii) The net cumulative result of *(i)* and *(ii)* is lower the overlap area, higher is the average strain in the adhesive-bonded lap joint. This can be seen in figure 3.5(e). As in a Kolsky Bar experiment, the average shear strength over the entire bonded assembly is measured from the

readings on the transmission bar, it will be found that a Kolsky Bar experiment predicts the same trend as discussed above, as shown in Figure 3.6 and 3.7.

Figure (3.6) shows the experimental observations of the influence of loading rate on the strength of the adhesive joints. In Figure (3.6) a comparison has also been made to the predicted values of the peak strain in the transmission bar as obtained from Equation 3.28(b), which was then post-processed using equations (3.2) and (3.3) to compare with the experimental predicted value of shear strength of the adhesive joint.

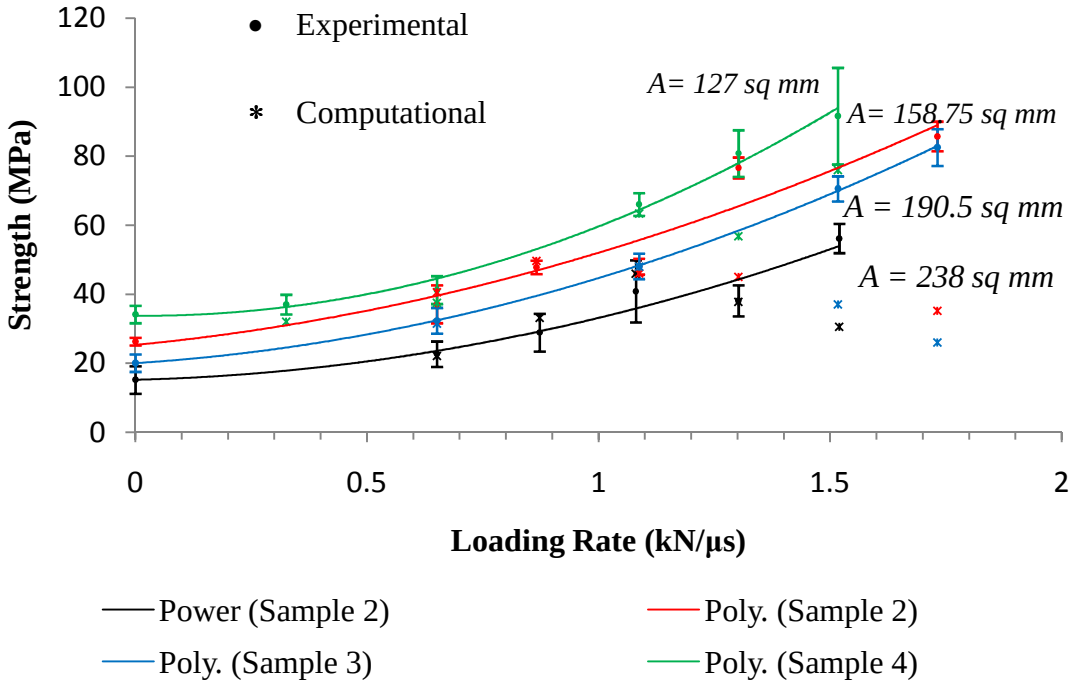

Figure 3.6 Variation of Strength in Adhesive Joint with Loading Rate

From Figure (3.6), it can be seen that for all the four samples adopted, the joint strength increases with loading rate. There is a reasonably good agreement between the experimental observations and the computational values for moderately high loading rates (till a rate of 1 kN/µs). However, at extremely high loading rates, there is considerable deviation from the

predicted response and the experimental observations. It is suspected that the lack of information on the rate-sensitive behavior of the adhesive causes this deviation. In the current analysis, a representative static value of the shear modulus of the adhesive has been adopted for the current analysis. The development of a precise mathematical model incorporating the rate-sensitive plastic behavior of the adhesive is left for future investigations. Nonetheless, the model presented here shows a reasonably accurate agreement with experimental observations for a fair range of loading-rates, and more importantly, it can be used to explain the apparent variation of joint strength with decrease in overlap area. Figure 3.7 shows the experimentally observed trend of over-lap area on the joint-strength at given loading rates.

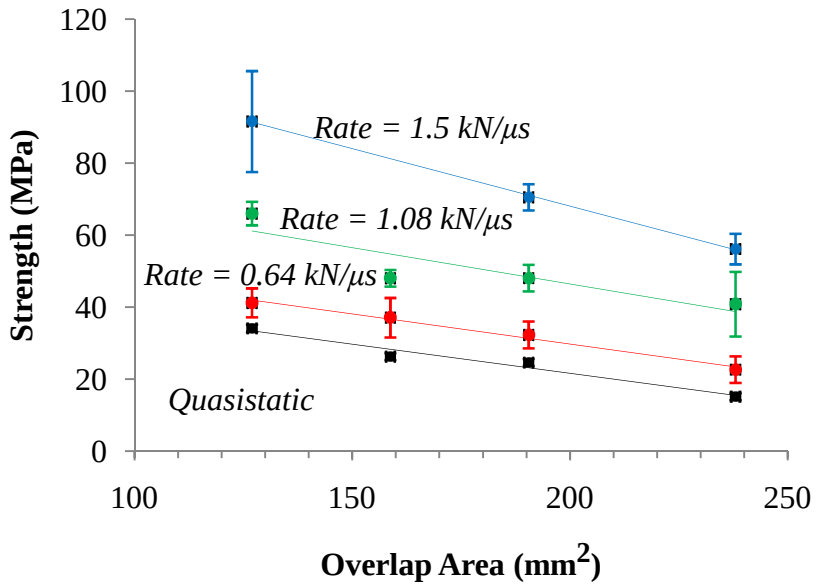

Figure 3.7 Variation of Average Shear Strength of the Adhesive Bonded Lap Joint with Overlap Area

It can be seen from Figure 3.7 that a larger overlap area decreases the shear-strength of the adhesive joint. This is because a Kolsky Bar experiment only predicts the shear stress at failure,

averaged over the entire length of the joint, and a detailed explanation of this has been given in the previous section of the investigation.

Finally, it must be mentioned here that the results were based on a constant thickness of the adhesive layer and for the bonding of similar adherends.

3.5 Conclusion

This part of the current investigation aimed at analyzing the drastic effect of overlap area on the prediction of the dynamic strength of an adhesive bonded single lap joint using a Kolsky Bar. A mathematical model for shear strain in the adhesive joint was developed by extending existing models for double lap joints to include the effect of strain-acceleration of the adhesive and the out-of-plane thickness of the adherend. A combined computational-experimental method was used to predict the shear strain distribution on the adhesive length at the time of failure. It was observed that only a part of the adhesive layer was strained at failure. Further, it was also observed that by changing the in-plane thickness of the adhesive layer for a given over-lap length of the adhesive decreased the maximum shear strain in the adhesive, but simultaneously increased the total length of adhesive that is subjected to non-zero strain- resulting in an increased average strain of the entire adhesive layer. The findings also suggested that decreasing the overlap length for a given out-of-plane thickness of the adhesive layer had no effect on the length of adhesive layer subjected to non-zero strain and the maximum strain in the adhesive changed slightly, as a result of which the average strain of the entire adhesive layer increased considerably. The net effect was found to increase the average adhesive strain by decreasing the overlap area of the adhesive. This was found in agreement with the Kolsky Bar experimental results. It was also found like many earlier researchers that increasing the loading rate increased the adhesive strength considerably. Reasonably good agreements were found between the

theoretical and experimental predictions of the bond strength over a considerable range of loading rate.

As a Kolsky Bar experiment only predicts the average value of the joint strength, it can be said that a Kolsky Bar gives a conservative estimate of the adhesive strength, the peak strength in the adhesive may be higher than that predicted value in a Kolsky Bar. In fact, it is seen that the most conservative estimate is given by selecting the diameter of the adherend to be equal to the bar diameter and by keeping the length of overlap as high as possible, so as not to affect stress-equilibrium on either faces of the joints during the duration of the experiment. A design based on such experimental predictions is inevitably in the conservative limits.

Finally, the mathematical model presented here is valid only after the Kolsky Bar specimen has achieved stress-equilibrium. This has been indirectly incorporated in the current model by including a suitable transmission coefficient in Equation (3.25). Without this, the strain prediction in the transmission bar with the use of Equation (3.28) would not have been possible.

The task of incorporating the rate-dependant behavior of the adhesive into the existing mathematical model is left as a future work. In addition, the extension of the current model to include the case of dissimilar adherends may also be undertaken in future.

CHAPTER 4

Design of a Tensile Hopkinson Bar

4.1 Introduction

Since the introduction of the Split Hopkinson Pressure Bar in the form of two “split” bars acting as transducers by Kolsky [**4.1**], shear and tensile versions of SHPB has been developed as well. The tensile version of SHPB, described in this chapter as the Split Hopkinson Tensile Bar (SHTB), is necessary; as many materials like unidirectional composites behave differently in compression than in tension [**4.2**]. Other examples include ductile materials, metals for example, which are stronger in tension than compression. The design of SHTB is generally different than a conventional SHPB; the reason for this being manifold and are discussed in the subsequent sections of the chapter. In view of these difficulties, various designs that have been previously adopted and described are presented in the current investigation.

Broadly speaking, the design of SHTB is classified into three categories. The first of these involves generating a direct tensile pulse [8] by suddenly releasing stored tensile energy in an incident bar, hitherto loaded statically by a clamping mechanism. The second type of design principle involves the changing of a compressive stress wave to a tensile stress wave by allowing it to reflect from a free end surface. Different designs involving this principle has been developed [**4.2**, **4.3-4.11**]. The third category is one which involves the modification of the compressive Hopkinson Bar (SHPB) in the sense that instead of altering the loading mechanism, the specimen geometry is changed, such that a part of the specimen is in tension, while the remaining is in compression [**4.12-4.13**].

4.2 Requisites of an acceptable design of a SHTB

Before discussing the various designs adopted in a SHTB apparatus, it is imperative to look into some requisites of a good design.

(1) Firstly, it is necessary to ensure that the tensile wave generated has a finite rise time. In fact, more the time needed for the pulse to attain a rise time, the better the progressive tensile properties of the material can be studied. The rise of the wave to its peak value should be smooth as much as possible, so that there is no unloading or load decrement in the specimen; at least till the peak load is attained. This means that the specimen is not subjected to a train of pulses, tensile-tensile or tensile-compressive. Thus, the generated tensile wave should have a trapezoidal profile as much as possible, with a finite, but minimal rise time with respect to the entire duration of the pulse.

(2) A major assumption involved in Hopkinson Bar analysis is that the stress waves measured with strain gages placed at approximately half the length of the incident and transmittance bar is the true representative of the stress-wave at the specimen-bar interface. As a stress wave, when undergoes impedance mismatch in its path of travelling, is partly reflected back and is partly transmitted, and if dispersion effects are neglected, impedance mismatch in a bar of a given (homogenous) material can be caused only due to changes in cross-section (area) of the bar. The condition that the cross-section of the incidence/transmittance bar should be same in the portion between the point of measurement of the incidence and transmission pulses and the interface between the bars and the sample is imperative to ensure that the assumption discussed above is valid. Ensuring validity of the assumption is generally a daunting task, as gripping a tensile specimen requires the incidence/transmission bar to be threaded, which thereby causes changes in the cross-section of the bars and often ‘distorts’ the stress-waves and causes

successive reflections of the pulse in the threaded section. However, if the threaded length of the bar is less than the bar diameter, then the effect of the small changes in cross-section can be neglected [**4.14**].

(3) The testing of brittle materials often requires the use of proper pulse shaping techniques [**4.15, 4.16**]. A pulse shaper increases the rise time of the pulse and in construction, is typically a soft material like paper, copper etc. placed in front of the incidence bar, at the bar-striker interface [**4.17**]. A wave-generating mechanism, that allows pulse shapers to be incorporated in the assembly, is thus desired.

(4) The specimen in the Split Hopkinson Tensile Bar is usually, like any other tensile test, a dog-bone specimen, or a specimen of a changing cross-section along its length. Trends in combining the Split Hopkinson Bar technique with Digital Image Correlation [**4.19**] requires a design that enables the specimen to be viewed during a SHPB/SHTB experiment using a high speed digital camera.

4.3 Review of some of the previous designs of SHTB

In a method devised by Harding et al. [**4.4**], the input bar is made of a hollow tube in which the elastic bar assembly or the specimen weighbar assembly is fitted, as illustrated in Figure 4.1. The uniform elastic bar assembly is shown in Figure 4.1(a) without its surrounding weigh bar tube. This bar is used first in an impact test to determine the input condition. A second identical test is performed with the specimen and the inertia bar fitted into the weighbar tube as shown in Figure 4.1(b). The loading is achieved by firing a striker to impact the weighbar. Any alteration of the transmitted wave shape caused by the changes in cross-section of the tube was neglected. The difference between the yoke velocity and the velocity of the upper end of the specimen, as

obtained from the strain measurements, was used to construct stress–strain curves. The stress at the upper end of the specimen was assumed to be representative of the stress throughout the specimen, i.e. the specimen inertia was neglected. Since the load is applied to the specimen indirectly through the weighbar tube, any eccentricity in the impact will produce flexural stress waves in the weighbar tube. However, due to the slower propagation velocity of flexural waves, there was a sufficiently long time for materials with a definite yield point to reach the upper yield stress before the arrival of flexural wave components. The same method was later modified by introducing an instrumented input bar preceding the specimen and inertia bar and also sliding freely within the weighbar tube. This new version of the split Hopkinson pressure bar was used by Harding and Welsh [**4.5**] for the tensile testing of fiber-reinforced composites.

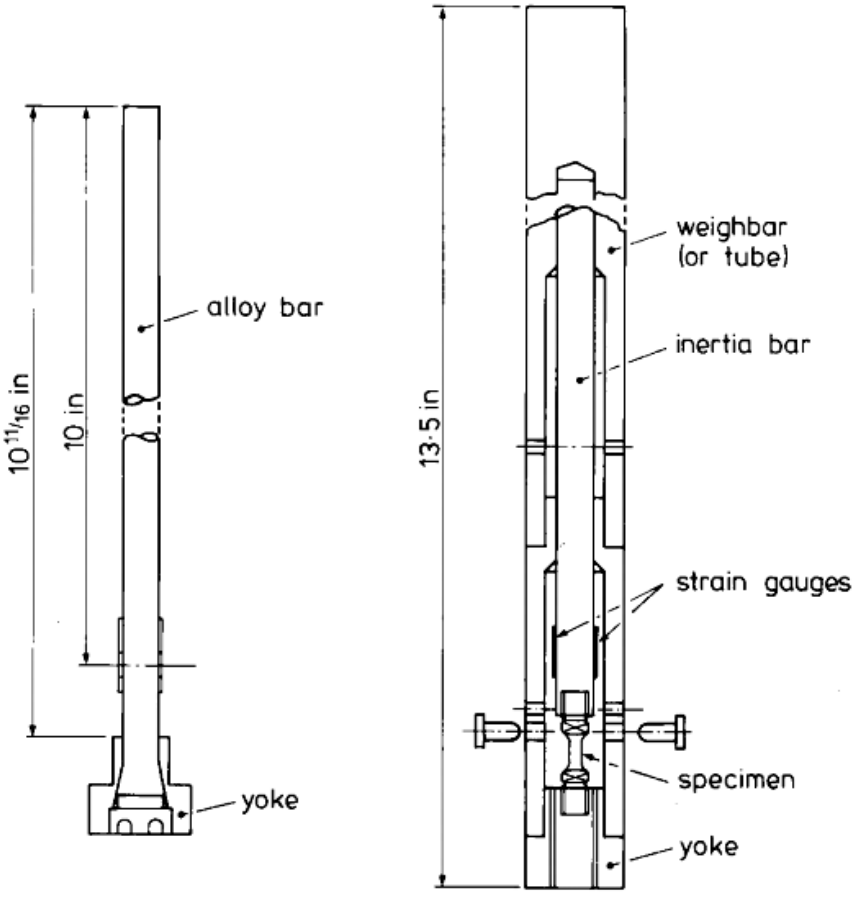

Figure 4.1. Set-up of the SHTB by Harding [**4.5]**

In light of the criteria discussed in the previous section, it can be concluded that pulse shaping is difficult to be achieved using the above configuration.

Hauser *et. al.*[**4.6**] proposed a different design of the tensile Hopkinson bar. In this set up, the specimen is threaded inside two long elastic bars- the incident and the transmitter bar and a tensile wave is generated in the incidence bar by attaching it by means of a transfer-connection to other two long bars which are impacted by a projectile at the end opposite to that, where it is connected to the incidence bars by transfer-connections. Thus, the rise time of the tensile stress in the incidence bar is determined both by the impact velocity of the projectile as well as the dimensions of the transfer connection. The entire assembly is shown in Figure 4.2. The amplified input and output signals from the strain gauges at positions 1 and 2 are used in a one-dimensional stress wave analysis to obtain the stress, strain and strain rate of the tensile loading. Thus, as the striker impacts the long bars, it generates a compressive wave in the same, which are reflected at the free end of the transfer connection as a tensile wave, part of which travels back through the long bars and the remaining passes into the incidence bar, which is used to load the specimen. This apparatus provides the ease of pulse shaping, viewing the specimen is also easy and the tensile pulse, one generated in the incidence bars, does not undergo any abrupt changes in cross-section of the same in its path of travelling (except at the threads which connect the specimen to the incidence bar). The major disadvantage of the design is that it requires very long transfer connections, to avoid overlapping of the compressive wave, first generated by impact, and the tensile wave generated by reflection of the compressive wave at the free end of the transfer connection. In the absence of such considerations, generating a trapezoidal-like pulse is almost next to impossible.

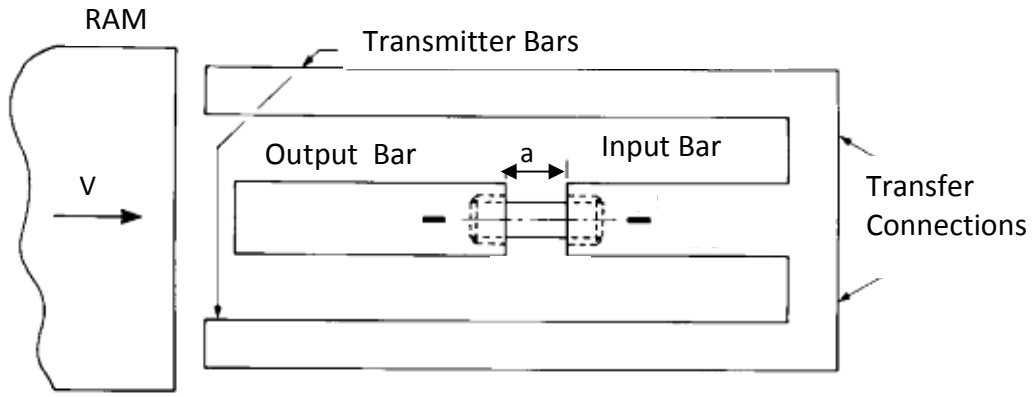

Figure 4.2 Set up by *Hauser et. al.*[**4.6]**

The third set up, discussed here, was proposed by Lindholm and Yeakly [**4.12**] which comprised of the incidence bar and the transmission bars (which was tubular in nature) to be equal cross-section and the specimen was sandwiched in between the two, very much alike to a conventional SHPB. A compressive wave was generated in the incidence bar by impacting it with a projectile fired at a known velocity. The only modification made was that the specimen was altered to a hat-shaped specimen. The actual gauge section of the tensile specimen has four equal arms, each with a length–width ratio of approximately 2:1.The set-up is shown in Figure 4.3. The applied loading and deformation of the specimen are derived from strain-time measurements on the radial surfaces of the two elastic pressure bars using diametrically opposed strain gauges. In this analysis, the internal wave reflection in the specimen is neglected. The technique is not accurate for determining the elastic modulus and may introduce some uncertainty at stresses near the yield strength if this occurs before stress equilibrium is established. In this design, viewing the specimen, pulse shaping and generating nearly trapezoidal pulses, which undergo no abrupt change in the cross-section in the path of its travel, is easy. However, it was found that the specimen strength falls below that of round specimens. After a thorough investigation by Lindholm, it was found that this effect was due to geometry of the specimen, in that the gage section was very thin and there was a possibility of the existence

of a bending stress, since the line of load application in the ‘hat’ specimen is not coincident with the centroid of the gauge section, as is the case in the round tension specimen.

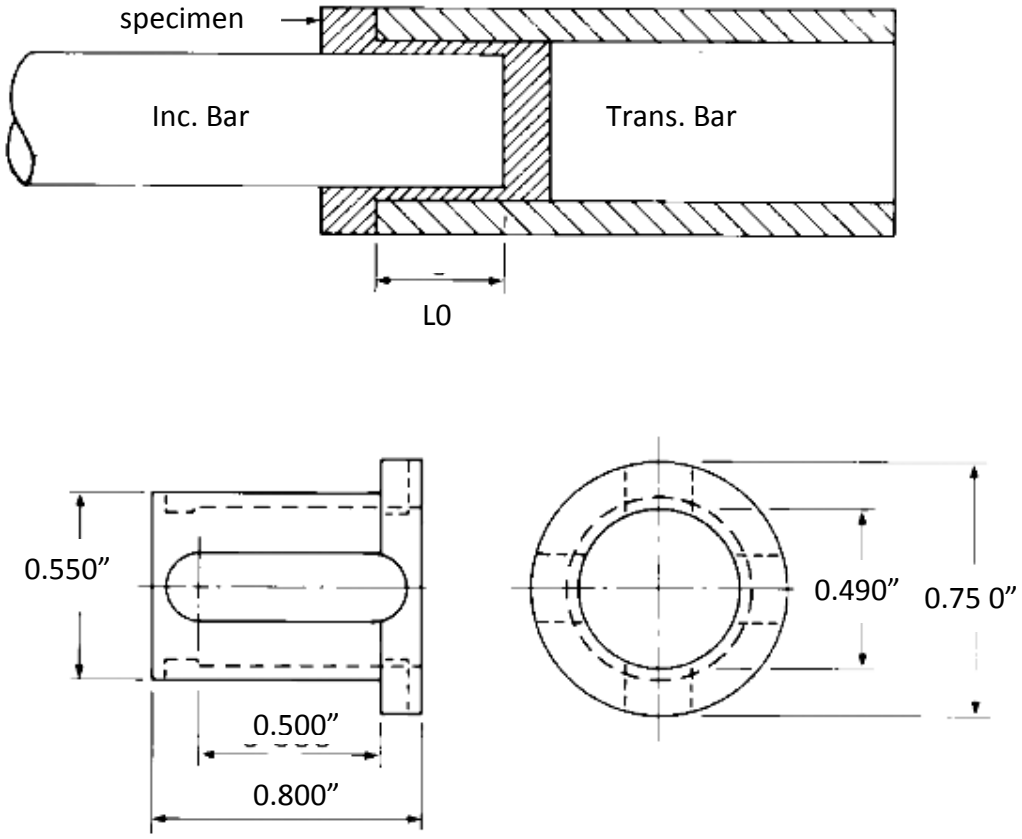

Figure 4.3 Set-up of Lindholm *et. al.*[**4.12]**

A modification of the set-up described by Hauser *et al.*[**4.6]** was adopted by Eskandari and Nemes [**4.2**] for the test of quasi-isotropic laminate made of unidirectional piles of graphite-epoxy composites. This set up uses specimens that are threaded between the incidence and transmission bars (for metals) or are connected to the two using epoxy chambers and two side-bars for transmitting the compressive wave into a side-bar connector, where in it would be reflected as a tensile wave, portion of which would travel back into the side-bar connectors, while the remaining of it would go into the incidence bar, which was used for loading the

specimen. The modification made here was that the projectile, instead of hitting the transmitter bars directly, would hit another side-bar connector, which was connected only to the side-bars. The details of the design are shown in Figure 4.4. In this design, the length of the pulse was affected by the length of the side-bar connectors. The influence of the connector was approximately a two-fold increase in the length of the pulse; and due to the presence of the same, instead of a quasi-rectangular pulse, a quasi-triangular pulse was reported to be generated. Here also, the major disadvantage is that it requires very long side-bar connections, to avoid overlapping of the compressive wave, first generated by impact, and the tensile wave generated by reflection of the compressive wave at the free end of the side-bar connectors.

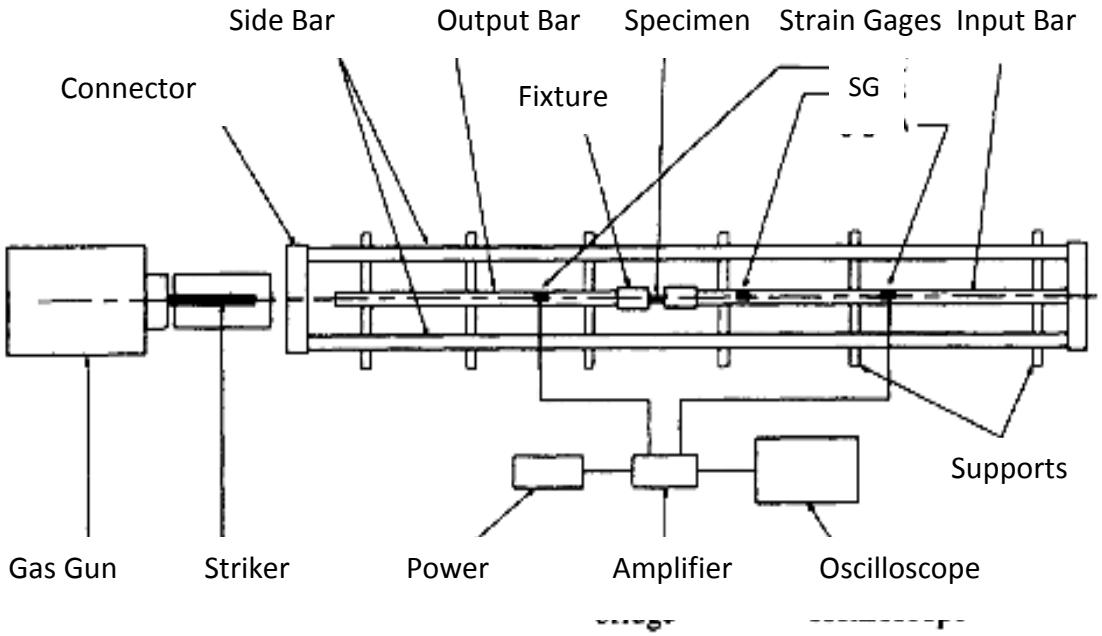

Figure 4.4 Set-up of the SHTB by Eskandari and Nemes **[4.2]**

A test-set up was designed to generate a direct tensile wave that was generated by release of the stored load in a part of the incidence bar by Staab and Gilat [**4.3**] The input and output bars were both 12.7mm diameter 7075-T651 aluminum, the input bar being 3.68m long and the

output bar being 1.83m long. A clamp/load reaction assembly was placed at approximately the midspan location of the input bar. The input load was stored in the bar by initially tightening the clamp and then applying direct tension at the end of the bar through a system of cables, pulleys and a hydraulic pump. When the clamp was released a tensile wave of half the magnitude of the stored force propagated toward the specimen as a loading wave. A release wave propagated in the other direction toward the end of the input bar. A diagram showing the propagation of elastic wave fronts in the apparatus is shown in Figure 4.5. The major disadvantage of the set- up is that there is no control over the profile of the wave generated, in that, pulse shaping technique is impossible.

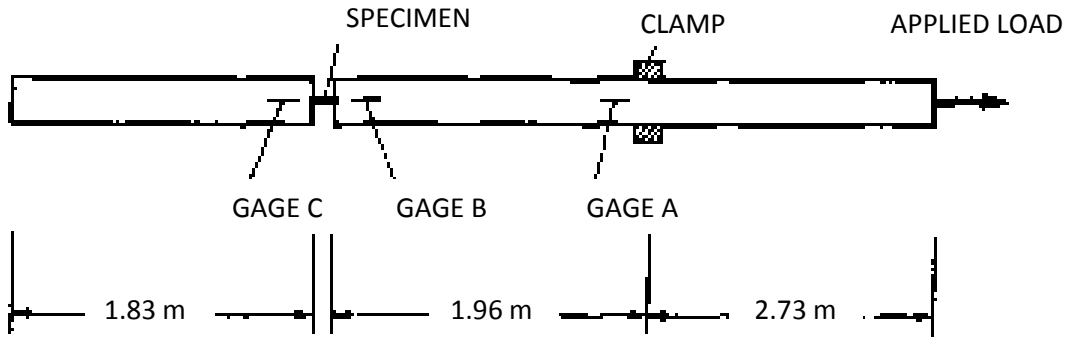

Figure 4.5 A Direct Tensile Split Hopkinson Bar **[4.3]**

A more commonly adopted system is a modification of the conventional SHPB [**4.7-4.9]**. The main differences are that the input bar (bar 1) is twice the length of the transmitter bar (bar 2) and that the specimen is a threaded-end tensile specimen. A collar made of the same material as the pressure bar is placed over the specimen and firmly fitted against the shoulders of the pressure bars. The ratios of the cross-sectional areas of the collar and specimen to the cross-sectional areas of the collar and the specimen to the cross-sectional area of the pressure bars are 3: 4 and 1:2 respectively. When the input bar is struck by a striker that has a maximum length of

less than half that of the transmitter bar, the input compressive wave is transmitted almost entirely through the collar to bar 2, with little effect on the specimen. When this compressive pulse reaches the free end of the transmitter bar, it is reflected as a tensile pulse. This tensile pulse is used to load the specimen, since the collar is unable to sustain any tensile load. The calculation of the specimen stress and strain were done identically as in a conventional SHPB. Figure 4.6 shows the details of the set-up.

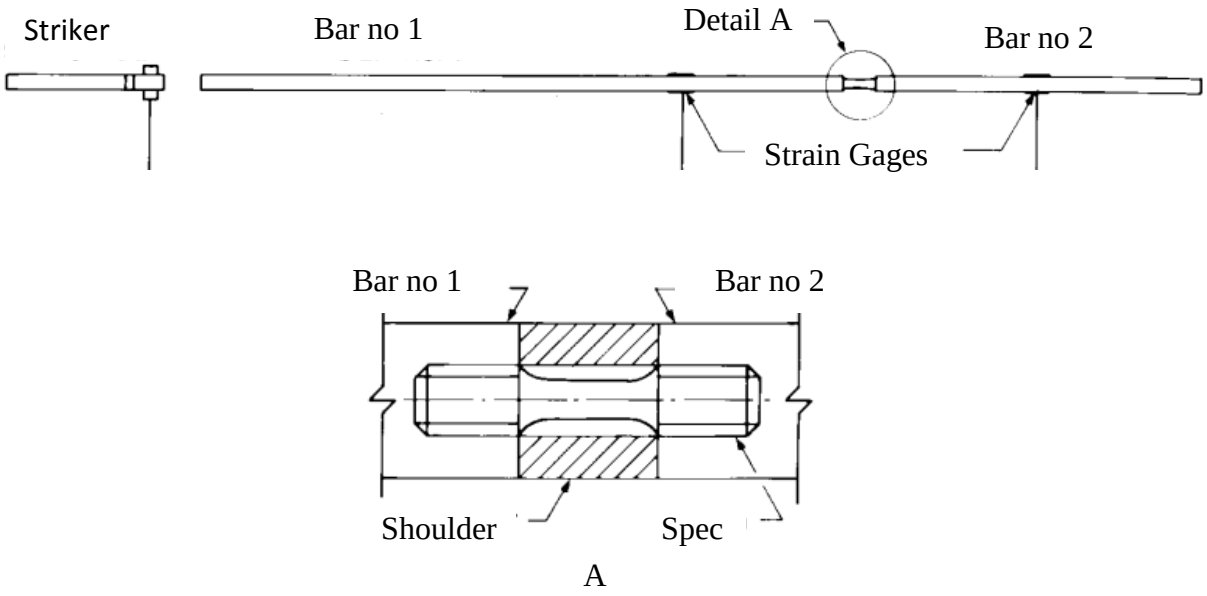

Figure 4.6 A Tensile Hopkinson Bar [**4.9]**

A commonly used set-up of the Tensile Hopkinson Bar involves a tubular striker, which strikes a transfer flange, fixed at the end of the incidence bar [**4.10,4.11**]. The striker strikes the transfer flange and generates a compressive wave there in, which is reflected at the free end of the flange as a tensile pulse and travels through the incidence bar. This is used to load the specimen, which is typically threaded on between the incidence bar and the transmitter bar. The schematic representation of the same is shown in Figure 4.7. The strain gages locate at

approximately the mid-span of the two bars record the stress-history and are used to calculate the stress and strain in the specimen.

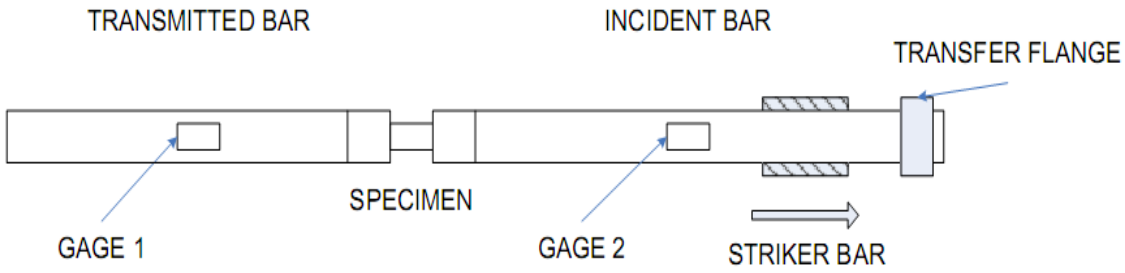

Figure 4.7 A Tensile Hopkinson Bar using a transfer flange [**4.10]**

The last two set-ups described here satisfy most of the requisites of a good design of the Hopkinson bar- the tensile pulse once generated undergoes no changes in cross-section in its path, generation of a clean tensile pulse is relatively easy, and specimen viewing is also easily achievable. The only consideration with the design described in Figure 4.6 is that a part of the initial compressive pulse generated is inevitably taken up by the specimen, while as the collar cannot take up tensile pulse, it has a tendency to collapse onto the specimen, while the latter undergoes tension. In the design described by Figure 4.7, pulse shaping is achieved only indirectly, by placing the pulse shaper on the transfer flange.

Although small, distortion on the tensile pulse once generated is almost inevitable in all the designs discussed here, due to the threaded connection between the elastic bars and the specimens. The use of M-Shaped specimens in a SHPB apparatus has therefore been suggested by Mohr and Gary [**4.13**]. The M-specimen was designed to transform a compressive loading at its boundaries into tensile loading of its two gage sections. The specimen suggested by them and its Finite Element Stress contour is Figure 4.8. Some important considerations to be adopted while designing the specimen was suggested as follows:

(1) Limit plastic deformation to the gage section.

(2) Minimize bending deformation at the gage section

(3) Prevent buckling of the segment at the boundaries as they are relatively thin

Based on the above considerations, is was concluded that the gage section should be as thin and short as possible for optimal specimen performance in terms of field uniformity within the gage section and of maximum strain rate. The disadvantage with the method is that many classes of specimens are difficult to be machined into an M Shaped specimen, examples of which include biological specimens like tissues, muscles, composite fibers like strands of Kevlar® , etc.

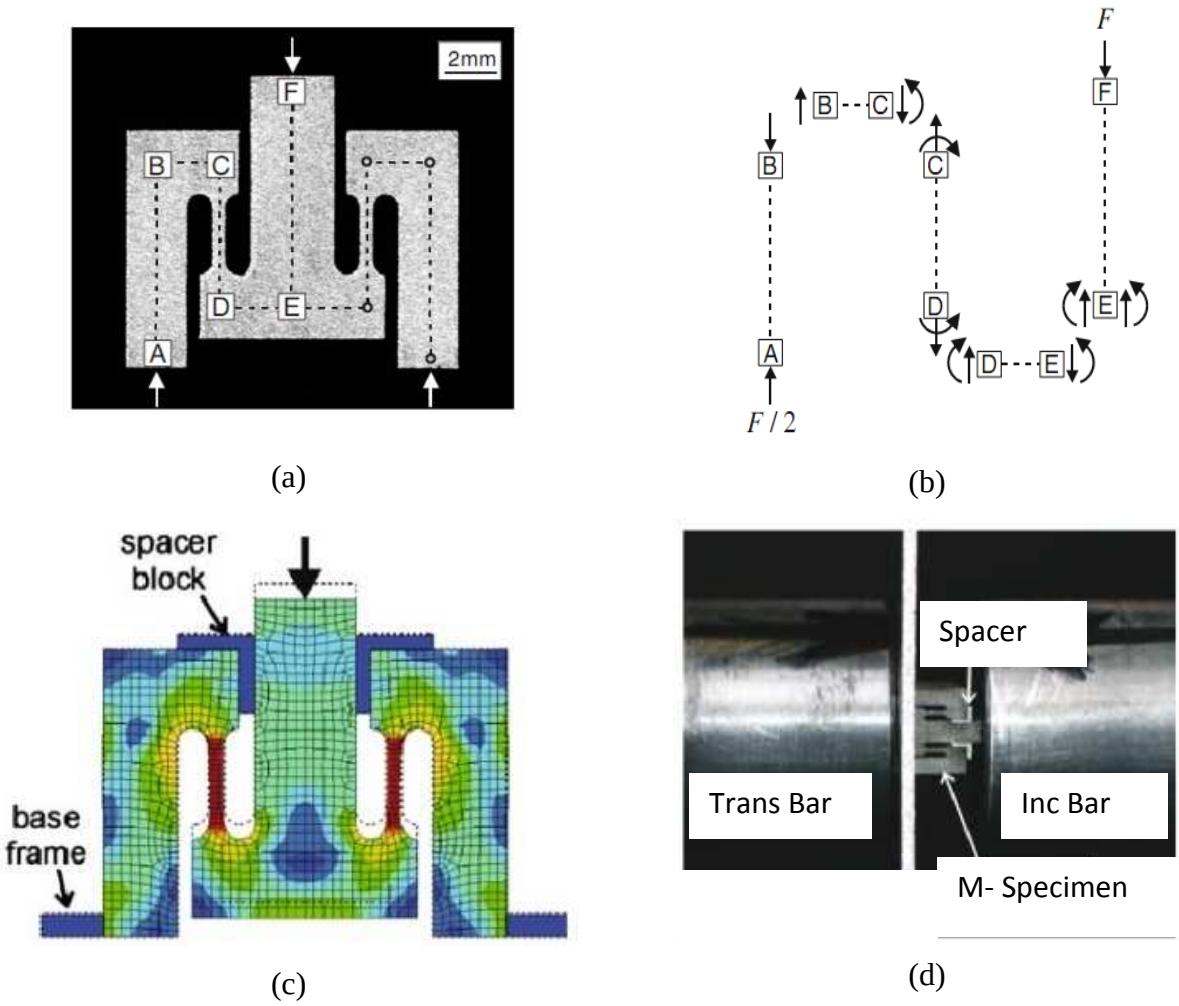

(a) (b) (c) (d)

Figure 4.8 (a) Details of the M Shaped Specimen (b) Structural and (c) Finite Element Analysis of the Specimen (d) The Sandwiched M Shaped Specimen between the Incidence and Transmission Bars **[4.13]**

4.4 The Design of the Split Hopkinson Tension Bar

The tensile bars developed at the Composite Vehicle Research Center employs the use of a transfer flange for generating a tensile pulse. A schematic representation of the bar is shown in Figure 4.9.

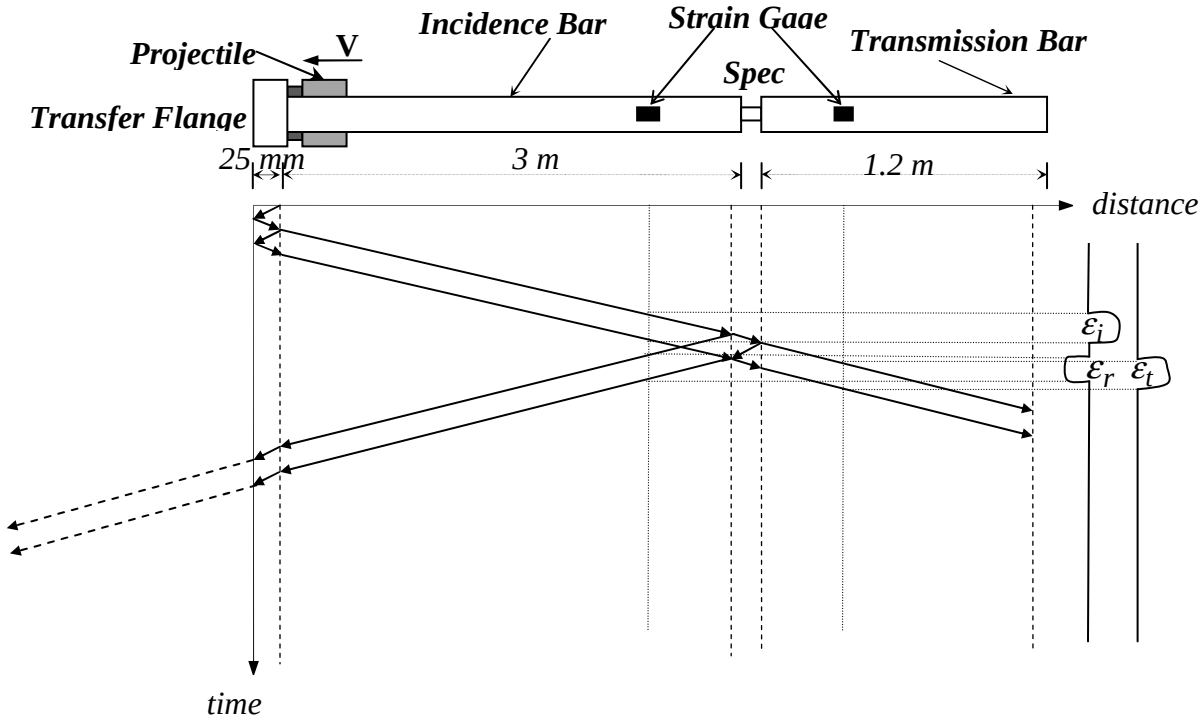

Figure 4.9 Schematic of the Kolsky Bar developed in CVRC

The Kolsky bar developed here rests on the principle that a compressive stress-wave reflects from a free end as a tensile wave. A tubular striker with the outside diameter same as that of the flange impinges on the flange to generate a compressive wave in the same. The compressive wave is reflected at the free end of the flange as a tensile wave and travels through the flange. A part of it is transmitted into the incidence bar and a part of it is reflected as a travelling

compressive wave in the flange itself. A momentum trap is provided at the end of the flange with the diameter exactly the same as the flange. The second compressive wave travels through this momentum trap and after being reflected again as a tensile wave at the free end of the bar, causes separation of the flange and the momentum trap, thus preventing a train of pulses to be incident on the specimen. Bonded-resistance strain gages installed at the incidence and transmission bars allow recording of the pulses therein and the data analysis is exactly the same as that of the Split Hopkinson Pressure Bar. Figure 4.10 shows the Split Hopkinson Tensile Bar developed.

The incidence bar, transmission bar, transfer flange, momentum trap and projectiles are made of high yield strength aluminum (Alloy 7075). The incidence bar and transmission bar are 15.9 mm in diameter and the length of these are 3m and 1.2 m. The momentum trap is a solid aluminum bar of diameter 50.8 mm and 1.8 m long. The flange is also of 50.8 mm diameter and is 50.8 mm thick. Different projectiles of length 127mm, 102 mm, 76mm and 50.8 mm have been prepared each with an outside diameter of 50.8 mm and an inside diameter of 15.8 mm. For attaching specimens, the ends of the incidence and transmission bars were threaded to a standard size of ½-20 threads.

In another variation of the set-up, the incidence bar was threaded into the momentum trap itself, without the flange. This may be regarded as a Kolsky Bar with a long flange, where the flange length is 1.8 m.

(a) (b) (c)

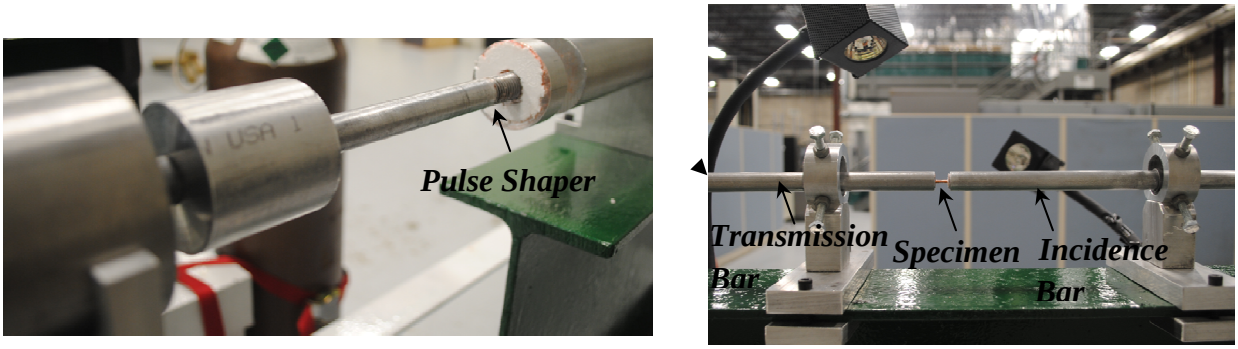

(e) (f)

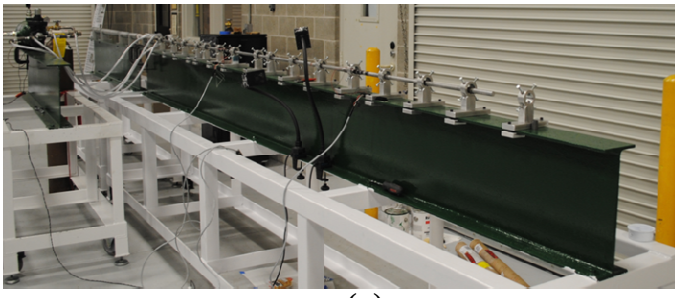

(g)

Figure 4.10 (a)-(g) Various views of the Tensile Hopkinson Bar

4.5 Calibration of the Tensile Hopkinson Bar

This section of the chapter aims to explore the general design characteristics of the Tensile Hopkinson Bar, i.e. to show the effect of threading the incidence bar for specimen grip, and to show the effect of coupling a flange, which in general does not have the same cross-sectional area as the striker – the former being one with a solid cross-section and the latter being one with

an annular cross-section. At this point, the reader is reminded that in the current design, two alternatives were explored with respect to the flange; one flange (length 50.8 mm) was shorter than the striker (length 127 mm), designated hereby as the short flange and the other where the length of the flange was 1.8 m, hereby referred to as the long flange.

(i) The first calibration of the tensile Hopkinson bar involves the determination of the length of the pulse. From the theory of elastodynamics, if the projectile and the bar where the projectile impacts are of the same cross-sectional area, then the length of the pulse generated is twice the length of the projectile. Here, however, this is not the case, as the projectile is of an annular cross-section, while the transfer flange has a circular cross-section. In case of the long flange, the entire pulse is allowed to attain its full length, while in case of the short flange, even before the whole pulse is generated, there will be reflections from the free end of the flange. Thus, the length of the pulse is not equal to twice the striker length. In addition to this, for a striker of a given length, the pulse generated by coupling the incidence bar with the short flange be expected to be equal to that generated by coupling the incidence bar with the striker. Figure 4.11 shows a typical incidence pulse for a striker of length 127 mm, which in a case where the cross-sectional areas of the striker and the flange are same would give a pulse of duration approximately 51 μs. In Figure 4.11, however, the duration of the pulse is 150 μs for the long flange and approximately 220 μs for the short flange.

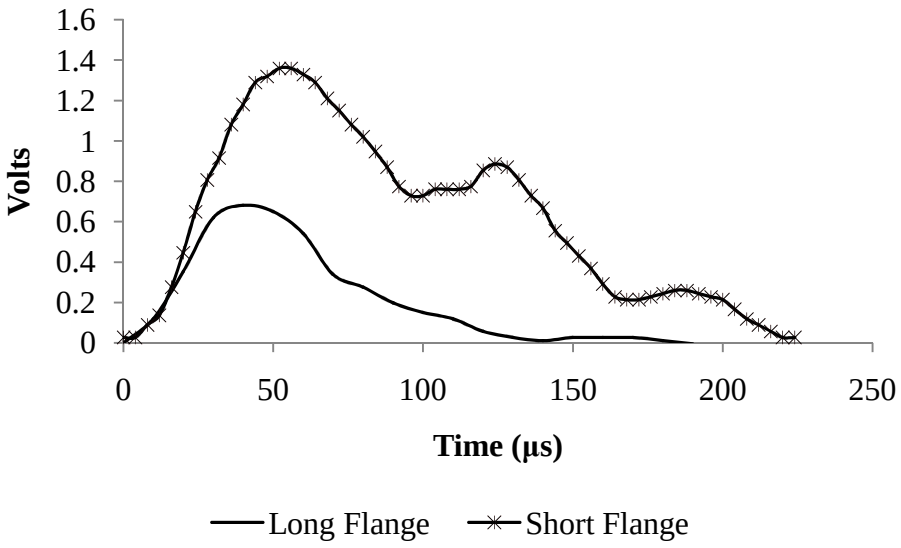

Figure 4.11. Incident pulse for a striker of length 127 mm

(ii) The second step in calibrating the Tensile Hopkinson Bar involves the task of ensuring that the incidence and the reflected pulses are the reflections of each other along the time-axis in the absence of a specimen. This is independent of the loading mechanism (i.e. the choice of flange); this check is crucial to ensure that the thread distorts the incidence pulse to a minimum. For this, the specimen was detached from the incidence bar, a striker of known length (127 mm) was fired from the gas gun and the incidence and reflected pulses, so generated, were measured from the strain-gage readings. A typical incidence and reflected pulse is shown in figure 4.12.

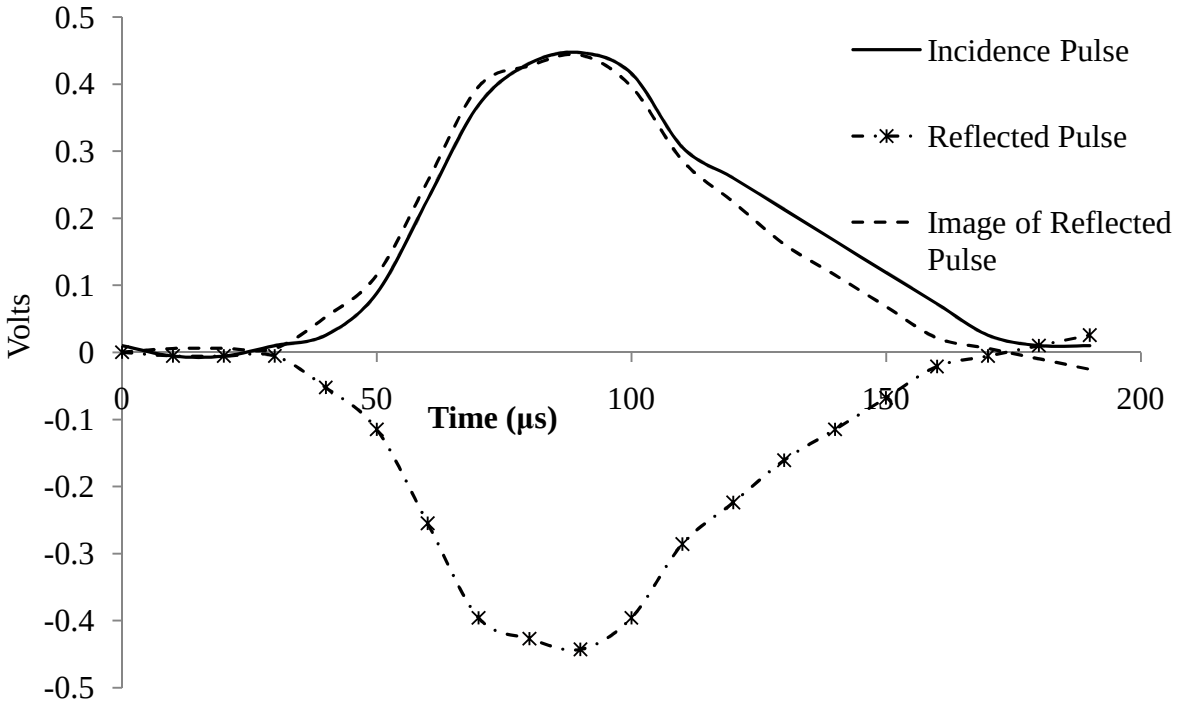

4.12 (a)

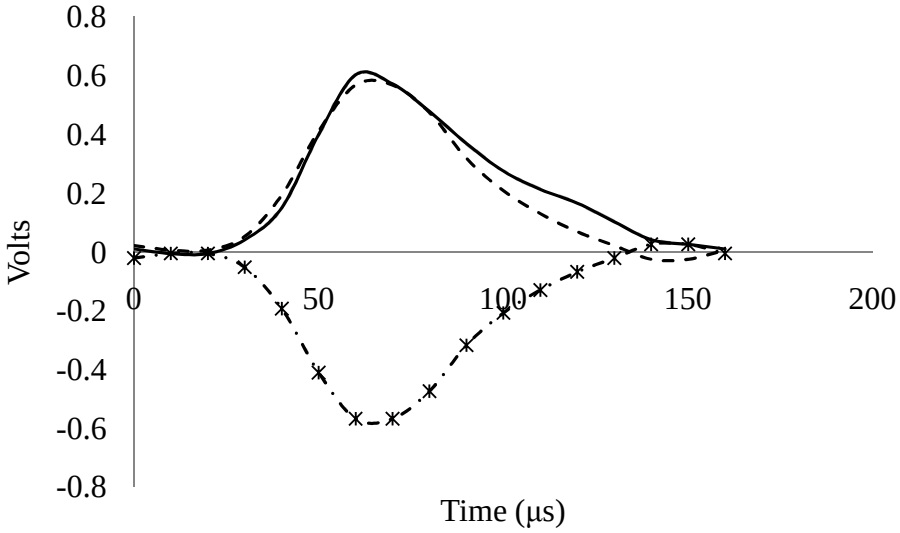

4.12 (b)

Figure 4.12. Comparison of the Incidence and Reflected Pulses

From Figure 4.12, it can be seen that the incidence and reflected pulse, though not exact mirror images of each other, are very similar in profile, i.e. their amplitude are almost exactly the same and the duration of both of them are also almost the same. The small mismatch in the

profile is due to the threads on the downstream end of the incidence bar, which causes some pulse distortion; however, as the threaded length (12.6 mm) is less than the bar-diameter (15.9 mm), this distortion is negligibly small and can be conveniently ignored.

(iii)The final calibration involved determination of the dynamic stress-strain properties of a known material using the tensile Hopkinson Bar. For this, OFHC Copper was selected as the material. The copper specimen had a diameter of 2.5 mm and a length of 7.62 mm at the gage section, while the ends of the specimen were threaded using a standard thread size of ½”-20 threads. The length of the threaded portion of the copper was 12.7 mm. Figure 4.13 shows the copper specimens that were adopted for the current calibration.

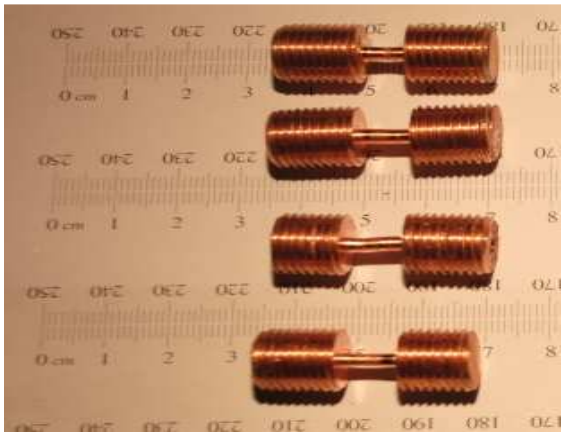

Figure 4.13 Copper Specimens

For the determination of the dynamic properties of copper, experiments were conducted in two configurations, once using the short flange and then using the short flange. Figure 4.14 shows the typical response obtained in the experiment.

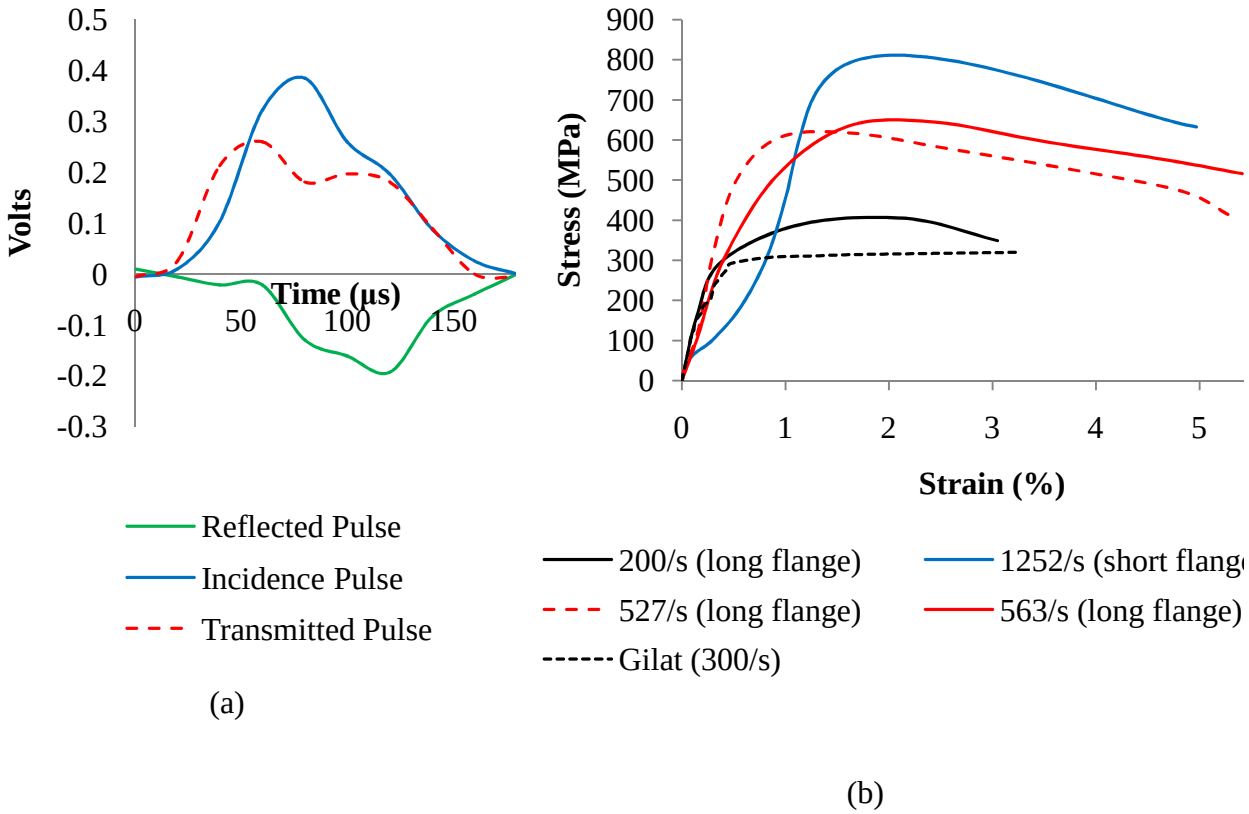

Figure 4.14 (a) Representative Pulses generated in determination of the dynamic properties of OFHC Copper (b) Stress-strain curve for OFHC copper

Compared to the stress-strain curve obtained by Gilat [**4.18**], the stress-strain curve obtained in the current SHTB shows an over-estimation of stress values by approximately 10%. This is because of the use of point-wise measurement (strain-gages) to calculate the stress-values and arises due to the negligence of the threaded length of the specimen. Nonetheless, the current SHTB is found to give a reasonably good stress-strain characteristic of the material whose dynamic properties are to be determined.

(iv)Based on Figure 4.11 and 4.14 some immediate conclusions can be drawn from the two variants of the SHTB developed at CVRC, viz. SHTB with a short flange and SHTB with a long flange. They are as summarized below

Table 4.1 Comparison of the Features of an SHTB with the long flange and short flange

Feature	**SHTB with Short Flange**	**SHTB with Long Flange**
Post-Impact Analysis	The SHTB, when used with a momentum-trap prevents successive train of pulses from impinging on the specimen. The specimen is thus amenable to post-impact analysis of its micro-structure.	The SHTB with the long flange causes successive train of pulses to impinge on the specimen. Post-impact analysis of the microstructural details of the specimen is thus not relevant to the first set of pulses that impinge on the specimen, unless the specimen is loaded till failure by the first set of pulses.
Amplitude of Pulses	Given a striker length and striker velocity, the SHTB with short flange generates higher amplitude of pulses compared to the one with long flange. Thus, higher strain-rate investigation is facilitated by this configuration of the design. The maximum stress developed in the material is also higher and this configuration is more suitable for materials with higher yield/ultimate stress like ductile materials, ceramics etc.	Given a striker length and striker velocity, the SHTB with long flange generates lower amplitude of pulses compared to an SHTB with a flange shorter than the length of the pulse. This configuration is thus suitable for investigating the material characteristics at relatively lower strain-rates. The maximum stress developed in the specimen is also lower and thus, this configuration is more suitable for

Table 4.1 Continued

		experiments with materials of lower yield/ultimate stress like composite fibers, biological materials like tissues etc.
Length of the pulse	Given a striker and a striker velocity, this configuration generally facilitates the generation of pulses of larger length. This is because the length of the flange is shorter than the width of the pulse generated in a semi-infinite flange (i.e. a very long flange), which results in successive internal reflections of the pulse generated by the first impact of the projectile.	The flange in this configuration may be considered semi-infinite with respect to the length of the projectile. This allows for the development of the full pulse length and there is no successive overlap resulting from internal reflections. The resultant pulse generated is thus of shorter magnitude as compared to the configuration with the flange being lesser than the striker length.
Shape of the pulses	With a given striker length and velocity, this generates a relatively less "cleaner" pulse shape as compared to the configuration with a long flange. Nonetheless, the shape of the pulse starts distorting only in the falling section of the pulse.	This configuration of the SHTB generates a cleaner tensile pulse. The pulse is smooth throughout its length.

It may thus be said that the choice of an SHTB with long flange v/s an SHTB with short flange depends on the discretion and requirements of the engineer. This is case specific and the requirements of final yield/ultimate stress of the material, desired strain-rate and the need for post-impact microstructural investigations govern the choice for selection of the appropriate experimental configuration of the SHTB developed at CVRC.

As a final remark, it may also be pointed out that the experimental determination of dynamic stress-strain properties of a material requires judicious design of the specimen in order to get a smooth reflected pulse and ensure that threading the specimen distorts the reflected pulse to a minimum. Like a Split Hopkinson Pressure Bar experiment, the tensile Hopkisnon Bar experiment also involves a series of trial specimen designs, before final determination of appropriate specimen dimensions for obtaining the stress-strain curve of the material. It must be ensured that the deformation is limited to the gage section and does not occur at the edges. At this point, it is worthy to note that apart from the above-mentioned copper specimens, another set of copper specimens, with a gage length of 5 mm was also machined. However, in such specimens, the deformation was found to occur at the edges rather than at the gage-section.

4.6 Conclusion

In this chapter, a newly developed Split Hopkinson Tensile Bar was described. Different existing designs were evaluated and the design adopted a principle of transfer flange used for generation of tensile wave by reflecting a compressive wave from the free end. Copper was selected as the model material and its dynamic properties were determined.

CHAPTER 5

Conclusion

5.1 Conclusion

The research work showed the effects of specimen size and shape in case of non-cylindrical specimens in a Kolsky Bar. A simple model for radial inertia was proposed and a design criterion for the judicious choice of non-cylindrical specimen was proposed and found to work reasonably well for the determination of the dynamic stress-strain properties of materials. The need for lubricating the specimen-bar interfaces appropriately was also emphasized and the need for maintaining proper test-conditions to avoid spurious results in a Kolsky Bar experiment was shown. The second part of the research comprised of studying the drastic effect of overlap area on the strength of adhesive bonded single lap joints. A combined experimental-numerical technique was employed to predict the strain distribution in the adhesive at the time of failure. This showed that there were significant stresses at the edges, while a large part of the adhesive layer was strain-free. The *prima facie* effect of overlap area on Kolsky bar prediction of the joint strength was found to arise as an effect of averaging the strain in the adhesive. Overall, the Kolsky Bar was found to give a conservative estimate of the joint strength under high loading rates. In addition to this, a Tensile Split Hopkinson Pressure bar was also developed and calibrated in the current thesis.

5.2 Scope for Future Work

In the study on non-circular specimens, the material was assumed to be a homogenous and isotropic material. As a future work, an estimate for inertia in anisotropic composites can be made by extending the proposed model for the same. As another extension of the current work, a design criterion can be established for foam-like materials as the design criterion suggested in the current research may be found to be impractical for testing of non-metallic foams. This is

because, testing of foam with larger void size requires a longer length of the sample to be tested in order for continuum assumptions to hold good. The second part of the research comprised of addressing the factor of determination of the dynamic strength of adhesive bonded single lap joints. While the development of precise mathematical models taking into account the rate-sensitive plasticity of the adhesive may has already been pointed out as a scope for future work, similar models can be developed taking into account the viscoelasticity or viscoplasticity of the adhesive, while simultaneously retaining the strain-acceleration term.

APPENDIX

Appendix A

Radial Inertia for Non-Cylindrical Specimens

In this section, a derivation for the inertial stresses in a non-cylindrical specimen is shown. The analysis follows that for cylindrical specimens from Samanta **[2.15]**.

If the rate of deformation tensor, d_{ij}, is a function of time only, then using the Eulerian frame of reference defined by $[x_1, x_2, x_3]$ as the independent spatial coordinates, with x_3 giving the axial direction of the specimen,

$$\frac{1}{2}\left(v_{i,j} + v_{j,i}\right) = d_{ij}(t) \tag{A.1}$$

If the material is incompressible,

$$v_{i,i} = 0 \tag{A.2}$$

In the cylindrical coordinates,

$$\frac{\partial v_z}{\partial z} = d_{zz}(t) \tag{A.3}$$

and following (A.2)

$$2\frac{\partial v_r}{\partial r} = -d_{zz}(t) \tag{A.4}$$

If h be the current height of the specimen and $-u(t)$ is the axial velocity acting on the specimen's end, then following Samanta **[2.15]** it can be shown that

$$v_z = -\frac{u}{h} z \tag{A.5}$$

$$v_r = \frac{u}{2h} r \tag{A.6}$$

Observing that $v_\theta = 0$, the following relations hold:

$$v_x = v_r \cos(\theta); v_y = v_r \sin(\theta) \tag{A.7}$$

$$\tan(\theta) = \frac{y}{x}; r = \sqrt{x^2 + y^2} \tag{A.8}$$

From (A.6), (A.7) & (A.8),

$$v_x = \frac{u}{2h} x \tag{A.9}$$

$$v_y = \frac{u}{2h} y \tag{A.10}$$

From the first-law of thermodynamics, denoting the kinetic energy by *K*, the internal-energy by *W*, and the surface traction by F_j acting over the surface S,

$$\frac{D}{Dt}(K + W) = \int_S F_j v_j dS \tag{A.11}$$

where $\frac{D}{Dt}$ denotes the material derivative.

If *A* be the cross-sectional area of the material, σ_{ij} the Cauchy stress-tensor, *V* the volume of the specimen, σ_D the average yield-stress then

$$\frac{D}{Dt}(W) = \int_V \sigma_{ij} d_{ij} dV = -uA\sigma_D \tag{A.12}$$

Again, as the tractions act only on the cross-section of the specimens at the end,

$$\int_S F_j v_j dS = uAp_{inc} \tag{A.13}$$

where p_{inc} is the mean traction acting at the face of the specimen in contact with the incidence bar, where the velocity is u.

The kinetic energy of the specimen is

$$K = \frac{1}{2}\rho \int_V \left({v_x}^2 + {v_y}^2 + {v_z}^2 \right) dV \tag{A.14}$$

$$\therefore \frac{D}{Dt}(K) = \frac{1}{2}\rho \int_V \left(2v_x \frac{D}{Dt} v_x + 2v_y \frac{D}{Dt} v_y + 2v_z \frac{D}{Dt} v_z \right) dV$$

$$= \rho \int_V \left\{ \frac{\left(x^2 + y^2\right)}{4h^2} u \frac{du}{dt} + \frac{3}{8} \frac{\left(x^2 + y^2\right)}{h^3} u^3 + \frac{z^2}{h^2} \frac{du}{dt} \right\} dV \tag{A.15}$$

The polar moment of inertia of a body is defined as

$$J = \int_A \left(x^2 + y^2 \right) dA \tag{A.16}$$

Further,

$$\int_V \left(x^2 + y^2 \right) dV = \int_z \int_A \left(x^2 + y^2 \right) dA dz = Jh \tag{A.17}$$

$$\int_V z^2 dV = \int_A \int_z z^2 dz dA = \frac{Ah^3}{3} \tag{A.18}$$

Combining (A.15), (A.17) and (A.18)

$$\frac{D}{Dt}(K) = \rho \left\{ \frac{J}{4h} u \frac{du}{dt} + \frac{3}{8} \frac{J}{h^2} u^3 + \frac{Ah}{3} u \frac{du}{dt} \right\} \tag{A.19}$$

Substituting (A.12), (A.13), (A.19) into (A.11),

$$\sigma_D = -p_{mu} + \rho \left\{ \frac{J}{4Ah} \frac{du}{dt} + \frac{3}{8} \frac{J}{Ah^2} u^2 + \frac{h}{3} \frac{du}{dt} \right\} \tag{A.20}$$

Due to the absence of shear-forces, the equation of motion in the axial direction is given by

$$\frac{\partial \sigma_z}{\partial z} = \rho \frac{D}{Dt}(v_z) \tag{A.21}$$

$$\therefore \sigma_z = -p_{mu} + p_{ml} = -\frac{\rho h}{2} \frac{du}{dt} \tag{A.22}$$

where p_{ml} is the surface traction at the transmission bar-specimen interface.

Combining (A.20) and (A.22),

$$\sigma_D = -p_{ml} + \rho \left\{ \frac{J}{4Ah} \frac{du}{dt} + \frac{3}{8} \frac{J}{Ah^2} u^2 - \frac{h}{6} \frac{du}{dt} \right\} \tag{A.23}$$

From the definition of natural axial strain,

$$\dot{\varepsilon} = -\frac{u}{h} \tag{A.24}$$

(A.20) and (A.23) can be written as

$$\sigma_D = -p_{mu} - \rho\left(\frac{J}{4A} + \frac{h^2}{3}\right)\ddot{\varepsilon} + \rho\left(\frac{J}{8A} - \frac{h^2}{3}\right)\dot{\varepsilon}^2 \tag{A.25}$$

$$\sigma_D = -p_{ml} - \rho\left(\frac{J}{4A} - \frac{h^2}{6}\right)\ddot{\varepsilon} + \rho\left(\frac{J}{8A} + \frac{h^2}{6}\right)\dot{\varepsilon}^2 \tag{A.26}$$

Thus,

$$\sigma_D = -\frac{1}{2}\left(p_{mu} + p_{ml}\right) - \rho\left(\frac{J}{4A} + \frac{h^2}{12}\right)\ddot{\varepsilon} + \rho\left(\frac{J}{8A} - \frac{h^2}{12}\right)\dot{\varepsilon}^2 \tag{A.27}$$

(A.25) through (A.27) are the model for stresses in a non-cylindrical specimen including the effects of inertia. For a cylindrical specimen of radius *a*,

$$\frac{J}{A} = \frac{a^2}{2} \tag{A.28}$$

(A.25) through (A.27) reduce to

$$\sigma_D = -p_{mu} - \rho\left(\frac{a^2}{8} + \frac{h^2}{3}\right)\ddot{\varepsilon} + \rho\left(\frac{a^2}{16} - \frac{h^2}{3}\right)\dot{\varepsilon}^2 \tag{A.29}$$

$$\sigma_D = -p_{ml} - \rho\left(\frac{a^2}{8} - \frac{h^2}{6}\right)\ddot{\varepsilon} + \rho\left(\frac{a^2}{16} + \frac{h^2}{6}\right)\dot{\varepsilon}^2 \tag{A.30}$$

$$\sigma_D = -\frac{1}{2}\left(p_{mu} + p_{ml}\right) - \rho\left(\frac{a^2}{8} + \frac{h^2}{12}\right)\ddot{\varepsilon} + \rho\left(\frac{a^2}{16} - \frac{h^2}{12}\right)\dot{\varepsilon}^2 \tag{A.31}$$

It can be seen that the inertial stresses in (A.26) comprise two terms; an extra axial stress occurring due to the effects of strain-acceleration and the other which occurs due to the effects of strain-rate. For a sample calculation of inertial stresses, consider an aluminum sample ($\rho = 2700 kgm^{-3}$), with a rectangular cross-section of dimensions 6 mm by 6 mm, and length 3.5 mm. The strain-rate as obtained from experiments using (2) is shown in Figure A.1 (a). The inertial stresses arising due to the strain-acceleration term and due to the strain-rate terms are shown in Figure A.1 (b) and Figure A.1 (c) respectively. The net inertial stress as calculated from (A.26) is then plotted in Figure A.1 (d).

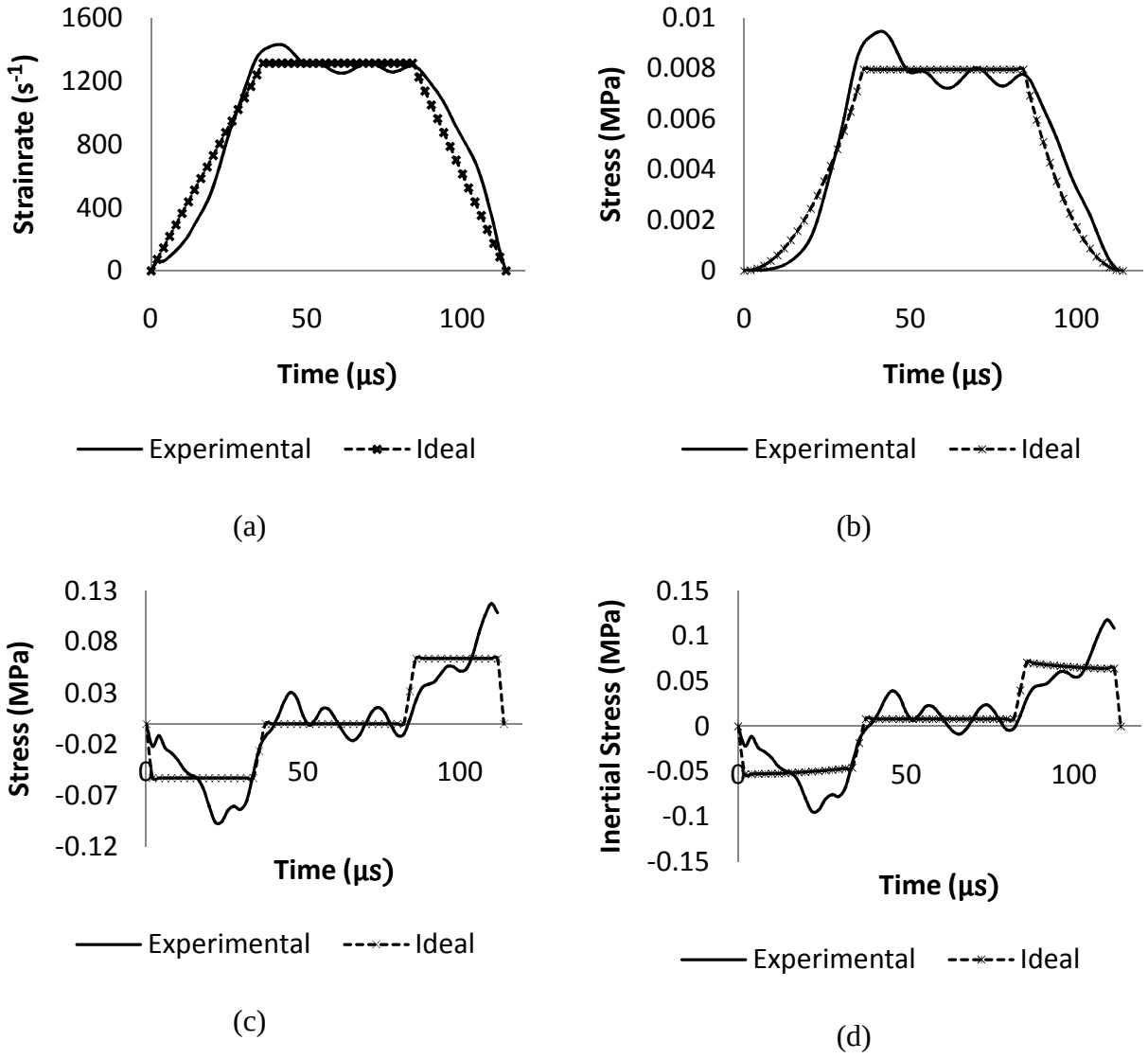

Figure A.1 Sample Calculation of Inertial Stresses (a) Strain-rate v/s time as obtained from experiments (b) Inertial Stress arising due to Strain-rate term (c) Inertial Stress arising due to the Strain-acceleration term (d) Total Inertial Stress

It can thus be seen from (A.1) that the inertial stresses during the period of constant strain-rate is extremely small, while the inertial stresses during the period if strain-acceleration is larger than during the constant strain-rate phase.

Appendix B

Solution of the Governing Equation for the Adhesive Strength of Lap Joints

For the problem of the adhesive strength of split-cylinder samples in a Kolsky Bar, the governing differential equation, from Equation (3.19), is as follows

$$\frac{\partial^2 \gamma_a(x,t)}{\partial x^2} - \frac{1}{c^2}\frac{\partial^2 \gamma_a(x,t)}{\partial t^2} = \frac{1}{\alpha}\gamma_a(x,t) \tag{B.1}$$

where γ_a is the shear strain of the adhesive, c is the wave-velocity of the adherend, and α is a parameter, depending on the mechanical properties of the adherends, adhesive as well as the diameter of the split-cylinder sample and the adhesive thickness. For a finite element defined by $x_a \le x \le x_b$, the weighted residual statement is given by

$$\int_{x_a}^{x_b} W\left\{\frac{\partial^2 \gamma_a(x,t)}{\partial x^2} - \frac{1}{c^2}\frac{\partial^2 \gamma_a(x,t)}{\partial t^2} - \frac{1}{\alpha}\gamma_a(x,t)\right\}\partial x = 0 \tag{B.2}$$

where W is a suitable weighting function. The weak-form is obtained by integrating (B.2) by parts to obtain

$$\int_{x_a}^{x_b}\left\{-\frac{\partial W}{\partial x}\frac{\partial \gamma_a(x,t)}{\partial x} - \frac{1}{\alpha}W\gamma_a(x,t) - \frac{1}{c^2}W\frac{\partial^2 \gamma_a(x,t)}{\partial t^2}\right\}\partial x + W\frac{\partial \gamma_a(x,t)}{\partial x}\bigg|_{x=x_b} - W\frac{\partial \gamma_a(x,t)}{\partial x}\bigg|_{x=x_a} = 0 \tag{B.3}$$

The exact shear strain is replaced by an approximate shear strain, $\hat{\gamma}_a$, defined by

$$\hat{\gamma}_a = \sum_{j=1}^{2} \gamma_j^e(t) N_j^e(x) \tag{B.4}$$

where γ_j^e is the shear strain at the j-th node and N_j^e is the first order Lagrange Interpolation Function for the e-th element. For a Galerkin weighted residual approach, the weighting function is selected the same as the interpolation function, i.e.

$$W = N_i, i = 1,2 \tag{B.5}$$

On substituting (B.4) and (B.5) into (B.3) the semi-discretized set of equations for each finite element is written as

$$\left[\mathbf{K}^e\right]\left\{\hat{\gamma}^e\right\} + \left[\mathbf{M}^e\right]\left\{\ddot{\hat{\gamma}}^e\right\} = \left\{\mathbf{f}^e\right\} \tag{B.6}$$

where

$$K_{ij}^e = \frac{\partial N_i}{\partial x}\frac{\partial N_j}{\partial x} + \frac{1}{\alpha} N_i N_j \tag{B.7a}$$

$$M_{ij}{}^e = \frac{1}{c^2} N_i N_j \tag{B.7 b}$$

$$\left\{\mathbf{f}^e\right\} = \lfloor f_1 \quad f_2 \rfloor^T = \left\lfloor -\left.\frac{\partial \gamma_a}{\partial x}\right|_{x=x_a} \quad \left.\frac{\partial \gamma_a}{\partial x}\right|_{x=x_b} \right\rfloor^T \tag{B.7c}$$

The elemental systems are then assembled together to obtain the global set of semi-discretized equations given by

$$[\mathbf{K}]\{\hat{\gamma}\} + [\mathbf{M}]\left\{\ddot{\hat{\gamma}}\right\} = \{\mathbf{f}\} \tag{B.8}$$

For time-integration, a half-step central difference scheme was adopted. The details can be found in Cook *et. al.* **[3.48]**. Here however, only the key steps are summarized.

$$\frac{1}{\Delta t^2}[\mathbf{M}]\{\hat{\gamma}\}^{n+1} = \{\mathbf{f}\}^n - \left[[\mathbf{K}] - \frac{2}{\Delta t^2}[\mathbf{M}]\right]\{\hat{\gamma}\}^n - \frac{1}{\Delta t^2}[\mathbf{M}]\{\hat{\gamma}\}^{n-1} \tag{B.9}$$

$$\{\ddot{\hat{\gamma}}\}^0 = [\mathbf{M}]^{-1}\left(\{\mathbf{f}\}^0 - [\mathbf{K}]\{\ddot{\hat{\gamma}}\}^0\right) \tag{B.10}$$

$$\{\hat{\gamma}\}^{-1} = \{\hat{\gamma}\}^{0} - \Delta t\left\{\dot{\hat{\gamma}}\right\}^{0} + \frac{\Delta t^{2}}{2}\{\ddot{\hat{\gamma}}\}^{0} \tag{B.11}$$

In the above, the superscript *n* denotes the time-step at which the value of the nodal shear strain vector, $\{\hat{\gamma}\}$ is evaluated. A convergence study, with respect to the shear strain at the mid-point of the adhesive layer was conducted for each case by varying the element size for a time-increment of 1μs. It was found that by choosing an element size between 0.0375-0.05 mm in resulted in converged solution for the given time-stepping.

REFERENCES

REFERENCES

[1.1] **Shukla, A., and Dally, J.W.** Experimental Solid Mechanics. Chapter 17, College House Enterprises, L.L.C, 5713 Glen Cove Drive. Knoxville, TN 37919, 2010, U.S.A.

[1.2] **Ramesh KT.,** High strain rate and impact experiments. In: Sharp WN (ed) Handbook of experimental solid mechanics, chapter 33, Springer, 101 Philip Drive, Norwell MA 02061, 2009, USA

[1.3] **Al-Mousawi, M.M., Reid S.R., and Deans, W.F.** The use of the split Hopkinson pressure bar techniques in high strain rate materials testing. *Proc. Instn. Mech. Engrs.*, 1997, **211-C**, 273-292.

[1.4] **Field, J.E., Walley, S.M., Proud, W.G., Goldrein, H.T., and Siviour, C.R.** Review of experimental techniques for high rate deformation and shock studies. *International Journal of Impact Engineering*, 2004, **30**, 725–775

[1.5] **Chen, W.W., and Song, Bo.** Kolsky Bar (SHPB) Experiments. *SEM preconference Short course 103*, 2009

[1.6] **Graff, K.F.** Wave Motion in Elastic Solids, *Dover Publications, Inc, New York*, 1991

[1.7] **Frew, D.J., Forrestal, M.J., and Chen, W.** Pulse Shaping Techniques for Testing Elastic-plastic Materials with a Split Hopkinson Pressure Bar. *Experimental Mechanics*, 2005, **45-2,** 186-195.

[1.8] **Song, B., and Chen, W.** Loading and Unloading Split Hopkinson Pressure Bar Pulse-shapingTechniques for Dynamic Hysteretic Loops. *Experimental Mechanics*, 2004, **44-6,** 622-627.

[1.9] **Vecchio, Kenneth S. and Jiang, Fengchun.** Improved Pulse Shaping to Achieve Constant Strain Rate and Stress Equilibrium in Split-Hopkinson Pressure Bar Testing. *Metallurgical and Materials Transactions A.* 2007, **38A,** 2655-2665.

[1.10] **Frew, D.J., Forrestal, M.J., and Chen, W.** Pulse Shaping Techniques for Testing Brittle Materials with a Split Hopkinson Pressure Bar. *Experimental Mechanics*, 2002, **42-1,** 93-106.

[1.11] **Nemat-Nasser, Sia., Choi, Jeom Yong., Guo, Wei-Guo., Isaacs, Jon B., and Taya, Minoru.** High Strain-Rate, Small Strain Response of a NiTi Shape-Memory Alloy. *Journal of Engineering Materials and Technology*, 2005, **127,** 83-89

[1.12] **Srivastava, V., Shukla, A., and Parameswaran, V.** Experimental Evaluation of the Dynamic Shear Strength of Adhesive-Bonded Lap Joints. *Journal of Testing and Evaluation,* 2000, **28,** 6, 438-442

[1.13] **Davies, E. D.H. and Hunter, S.C.** The dynamic compression testing of solids of the method of split Hopkinson pressure bar. *J. Mech. Phys. Solids*, 1963, **11**, 155–181

[1.14] **Frantz, C.E., Follansbee, P.S., Wright W.J.** New Experimental Techniques with the Split Hopkinson Pressure Bar. *8th International Conference on High Energy Rate Fabrication*, 1984

[1.15] **Song, B. and Chen, W.** Dynamic Stress Equilibration in Split Hopkinson Pressure Bar Tests on Soft Materials, *Experimental Mechanics*, 2004, **44-3,** 300-312.

[1.16] **Ravichandran, G., and Subhash, G.,** Critical appraisal of limiting strain rates for compression testing of ceramics in a split Hopkinson pressure bar. *J. Am. Ceram. Soc.* 1994, **77**, 263–267

[1.17] **Yang L.M., and Shim V.P.W.,** An analysis of stress uniformity in split Hopkinson bar test specimens, *International Journal of Impact Engineering*, 2005, **31**, 129-150.

[1.18] **Wu, X.J., and Gorham D.A.,** Stress equilibrium in the Split Hopkinson Pressure Bar Test, *J. Phys,*. 1997, **IV**, C391-C396

[1.19] **Davies, E. D. H.** A critical study of the Hopkinson pressure bar. *Phil. Trans. Ser.*, 1948, **A240**, 375–475.

[1.20] **Yew, E. H. and Chen, C. S.** Experimental study of dispersive waves in beam and rod using FFT. *J. Appl. Mech.*, 1978, **45**, 940–942.

[1.21] **Frantz, C.E., Follansbee, P.S., Wright W.J.** New Experimental Techniques with the Split Hopkinson Pressure Bar. *8th International Conference on High Energy Rate Fabrication*, 1984

[1.22] **Govender, R.A., Cloete, T.J.and Nurick, G.N.** A numerical investigation of dispersion in Hopkinson Pressure Bar experiments. *J. Phys. IV France*, 2006,**134** 521–526

[1.23] **Bertholf, L.D. and Karnes, C.H.** Two-dimensional analysis of the split-Hopkinson pressure bar system. *J. Mech. Phys. Solids*, 1975, **23**, 1–19.

[1.24] **Trautmann, A., Siviour, C.R., Walley, S.M., and Field, J.E.** Lubrication of polycarbonate at cryogenic temperatures in the split Hopkinson pressure bar. *International Journal of Impact Engineering* 2005, **3**,1 523–544

[1.25] **Hall, I.W., and Guden, M.** Split Hopkinson Pressure Bar compression testing of an aluminum alloy: Effect of lubricant type, *Journal of Materials Science Letters*, 2003, **22** , 1533-1535.

[1.26] **Hartley, R.S., Cloete, T.J., and Nurick, G.N.** An experimental assessment of friction effects in the split Hopkinson pressure bar using the ring compression test, *International Journal of Impact Engineering*, 2007, **34**,1705–1728.

[1.27] **Subhash, G., and Ravichandran, G.**, Split Hopkinson Pressure Bar Testing of Ceramics, *Materials Park, OH: ASM International*, 2000, 497-504.

[1.28] **Frew, D.J., Forrestal, M.J., and Chen, W.** A split Hopkinson bar technique to determine compressive stress-strain data for rock materials. *Experimental Mechanics*, 2001, **41-1**, 40-46.

[1.29] **Forrestal, M.J., Frew, D.J., and Chen, W.** The Effect of Sabot Mass on the Striker Bar for Split Hopkinson Pressure Bar Experiments. *Experimental Mechanics*, 2002, **42-2**, 129-131.

[1.30] **Luo, H. and Chen, W.** Dynamic Compressive Responses of Intact and Damaged AD995 Alumina. *International Journal of Applied Ceramic Technology*, 2004, **1-3**, 254-260.

[1.31] **Chen, W., Zhang, B., and Forrestal, M. J.**, A split Hopkinson bar technique for low-impedance materials. *Experimental Mechanics*, 1999, **39-2**, 81-85.

[1.32] **Chen, W., Lu, F. and Zhou, B.** A quartz crystal imbedded split Hopkinson bar for soft materials. *Experimental Mechanics*, 2000, **40-1,** 1-6

[1.33] **Casem, D., Weerasooriya, T. and Moy, P**. Inertial Effects of Quartz Force Transducers Embedded in a Split Hopkinson Pressure Bar. *Experimental Mechanics*, 2005, **45-4,** 368-376.

[1.34] **Hiermaier, S. and Meenken, T.** Characterization of low-impedance materials at elevated strain rates. *Journal of Strain Analysis for Engineering Design*, 2010, **45- 6**, 401-409.

[1.35] **Zhao, H., Gary, G. and Klepaczko, J. R.** On the use of a viscoelastic split hopkinson pressure bar. *International Journal of Impact Engineering*, 1997, **19-4**, 319-330.

[1.36]**Zhao, Han and Gary, Gerard.** A three dimensional analytical solution of the longitudinal wave propagation in an infinite linear viscoelastic cylindrical bar. Application to experimental techniques. *J. Mech. Phys. Solids*, 1995, **43-8**, 1335-1348.

[1.37] **Bacon, Christophe.** Separation of waves propagating in an elastic or viscoelastic Hopkinson pressure bar with three-dimensional effects. *International Journal of Impact Engineering*, 1999, **22,** 55-69.

[1.38] **Bacon, Christophe and Brun, Arnaud.** Methodology for a Hopkinson test with a non-uniform viscoelastic bar. *International Journal of Impact Engineering*, 2000, **24**, 219-230.

[1.39] **Casem, D.T., Fourney, W.L. and Chang, P.** A Polymeric Split Hopkinson Pressure Bar Instrumented with Velocity Gages. *Experimental Mechanics*, 2003, **43-4,** 420-427.

[1.40] **Johnson, T.P.M., Sarva, S.S. and Socrate S.** Comparison of Low Impedance Split-Hopkinson Pressure Bar Techniques in the Characterization of Polyurea. *Experimental Mechanics*, 2010, **50**,931–940

[2.1] **Kolsky, H.** An investigation of the mechanical properties of materials at very high rates of loading. *Proc. Phys. Soc.*,1949, **B-62**, 676-700

[2.2] **Song, Bo., Chen, Weinong., Ge, Yun., and Weerasooriya, Tusit.** Dynamic and quasi-static compressive response of porcine muscle. *Journal of Biomechanics*, 2007, **40**, 2999–3005

[2.3]**Ferreira, F., Vaz, M.A., and Simoes, J.A.** Mechanical properties of bovine cortical bone at high strain rate. *Materials Characterization*, 2006, **57**, 71–79

[2.4]**Woldesenbet, Eyassu., and Vinson, Jack R.** Specimen geometry effects on high-strain-rate testing of graphite/epoxy composites. *AIAA journal*, 1999, **v 37, n 9**, 1102-1106.

[2.5]**Koerber, H., Xavier, J., and Camanho, P.P.** High strain rate characterisation of unidirectional carbon-epoxy IM7-8552 in transverse compression and in-plane shear using digital image correlation. *Mechanics of Materials*, 2010, **42**, 1004-1019.

[2.6]**Pintado, P., Pedraza, C., Castillo, J.M. del., and Benitez, F.G.** Experimental investigation of the dynamic response of response of graphite-epoxy composite laminates under compression. *Composite Structures,* 2001, **53**, 493-497.

[2.7]**Dannemann, Kathryn A., Chocron, Sidney., Walker, James D., and Nicholls, Arthur E.** High strain rate compression testing of RCC materials. *Proceedings of the SEM Annual Conference and Exposition on Experimental and Applied Mechanics 2007,* 2007, **2**, 959-960

[2.8] **Schmidt, Tim., Gilat, Amos., Walker, Andrew., Seidt, Jeremy., and Tyson, John. 3D** Image correlation studies of geometry and material property effects during split Hopkinson bar experiments. *Society for Experimental Mechanics - 11th International Congress and Exhibition on Experimental and Applied Mechanics 2008,* 2008, **3**, 1624-1635.

[2.9] **Gilat, A., Schmidt, T.E., and Walker, A.L.** Full field strain measurement in compression and tensile split Hopkinson bar experiments. *Experimental Mechanics,* 2009, **49 [2]**, 291-302.

[2.10] **Schmidt, Tim., and Tyson, John.** 3D and 2D high speed image correlation for dynamic testing. *Society for Experimental Mechanics - SEM Annual Conference and Exposition on Experimental and Applied Mechanics 2009,* 2009, **3**, 1676-1687.

[2.11]**Siviour, C.R.** A measurement of wave propagation in the split Hopkinson pressure bar. Meas. Sci. Technol. 2009, **20,** 065702, 1-5.

[2.12] **Ramesh KT.,** High strain rate and impact experiments. In: Sharp WN (ed) Handbook of experimental solid mechanics, chapter 33, Springer, 101 Philip Drive, Norwell MA 02061, 2009, USA

[2.13] **Bertholf, L.D. and Karnes, C.H.** Two-dimensional analysis of the split-Hopkinson pressure bar system. *J. Mech. Phys. Solids,* 1975, **23**, 1–19

[2.14] **Pankow, M., Attard, C., and Waas, A.M.** Specimen size and shape effect in split Hopkinson pressure bar testing, J. Strain Analysis, 2009, **44**, 689-697

[2.15] **Samanta, S.K.** Dynamic deformation of aluminum and copper at elevated temperatures. *J Mech Phys Solids*, 1971, **19**, 117-135

[2.16] **Davies, E. D.H. and Hunter, S.C.** The dynamic compression testing of solids of the method of split Hopkinson pressure bar. *J. Mech. Phys. Solids*, 1963, **11**, 155–181

[2.17] **Gorham, D.A.** Specimen inertia in high strain-rate compression. *J. Phys. D: Appl. Phys.*, 1989, **22**, 1888–1893

[2.18]**Gorham, D.A.** The effect of specimen dimensions on high strain rate compression measurements of copper. *J. Phys. D: Appl. Phys.*, 1991, **24**, 1489–1492

[2.19] **Forrestal, M.J., Wright, T.W., and Chen, W.** The effect of radial inertia on brittle samples during the split Hopkinson pressure bar test. *International Journal of Impact Engineering*, 2007, **34**, 405-411

[2.20] **Song, B., Ge, Y., Chen, W.W., and Weerasooriya, T.** Radial Inertia Effects in Kolsky Bar Testing of Extra-soft Specimens. *Experimental Mechanics*, 2007, **47**, 659-670

[2.21]**Warren, T.L., and Forrestal, M.J.** Comments on the Effect of Radial Inertia in the Kolsky Bar Test for an Incompressible Material. *Experimental Mechanics*, 2010, 50, 1253–1255

[2.22] **Parry, D.J., Dixon, P.R., Hodson, S., and Al-Maliky N.,** Stress equilibrium effects within Hopkinson bar specimens, *Journal De Physique IV*, 1994,**4**, C8107-C8112

[2.23] **Ravichandran, G., and Subhash, G.,** Critical appraisal of limiting strain rates for compression testing of ceramics in a split Hopkinson pressure bar. *J. Am. Ceram. Soc.* 1994, **77**, 263–267

[2.24] **Subhash, G., and Ravichandran, G.**, Split Hopkinson Pressure Bar Testing of Ceramics, *Materials Park, OH: ASM International*, 2000, 497-504

[2.25] **Wu, X.J., and Gorham D.A.,** Stress equilibrium in the Split Hopkinson Pressure Bar Test, *J. Phys,*. 1997, **IV**, C391-C396

[2.26] **Yang, L.M., and Shim, V.P.W.,** An analysis of stress uniformity in split Hopkinson bar test specimens, *International Journal of Impact Engineering*, 2005, **31**, 129-150

[2.27] **Espinosa, H.D., Patanella, A., and Fischer, M. A.** Novel dynamic friction experiment using a modified Kolsky bar apparatus. *Experimental Mechanics*, 2000;**40(2)**,138–53

[2.28] **Trautmann, A., Siviour, C.R., Walley, S.M., and Field, J.E.** Lubrication of polycarbonate at cryogenic temperatures in the split Hopkinson pressure bar. *International Journal of Impact Engineering* 2005, **3**,1 523–544

[2.29] **Hall, I.W., and Guden, M.** Split Hopkinson Pressure Bar compression testing of an aluminum alloy: Effect of lubricant type, *Journal of Materials Science Letters*, 2003, **22** , 1533-1535.

[2.30] **Hartley, R.S., Cloete, T.J., and Nurick, G.N.** An experimental assessment of friction effects in the split Hopkinson pressure bar using the ring compression test, *International Journal of Impact Engineering*, 2007, **34**,1705–1728.

[3.1] **Osnes, Harald., and McGeorge, Dag.** Experimental and analytical strength analysis of double-lap joints for marine applications. *Composites: Part B*, 2009, **40,** 29–40

[3.2] **Zachary, L.W., and Burger, C.P.** Dynamic Wave Propagation in a Single Lap Joint. *Experimental Mechanics*, 1980, 162-166

[3.3]**Park, Hwun., and Kim, Hyonny.** Damage resistance of single lap adhesive composite joints by transverse ice impact. *International Journal of Impact Engineering*, 2010, **37**, 177–184

[3.4] **Vaidyaa, U.K., Gautam, A.R.S., Hosur, M., and Dutta, P.** Experimental–numerical studies of transverse impact response of adhesively bonded lap joints in composite structures. *International Journal of Adhesion & Adhesives*, 2006, **26**, 184–198

[3.5] **Higuchi, Izumi., Sawa, Toshiyuki., and Suga, Hidekazu.** Three-dimensional finite element analysis of single-lap adhesive joints subjected to impact bending moments. *J. Adhesion Sci. Technol.*, 2002, **16,** 10, 1327–1342

[3.6] **Higuchi, Izumi., Sawa, Toshiyuki., and Suga, Hidekazu.** Three-dimensional finite element analysis of single-lap adhesive joints under impact loads. *J. Adhesion Sci. Technol.*, 2002, **16**, 12, 1585–1601.

[3.7] **Rao, Yang., Lu, Daoqiang., and Wong, C.P.** A study of impact performance of conductive adhesives. *International Journal of Adhesion & Adhesives*, 2004, **24,** 449–453

[3.8] **Goglio, L., and Rossetto, M.** Impact rupture of structural adhesive joints under different stress combinations. *International Journal of Impact Engineering*, 2008, **35,** 635-643.

[3.9] **Sato, C., and Ikegami, K.** Dynamic deformation of lap joints and scarf joints under impact loads. *International Journal of Adhesion & Adhesives*, 2000, **20**, 17-25.

[3.10] **ASTM D950-03,** Standard test method for impact strength of adhesive bonds. ASTM Int, 2003.

[3.11] **Adams, R.D., and Harris, J.A.** A critical assessment of the block impact test for measuring the impact strength of adhesive bonds. *International Journal of Adhesion and Adhesives*, 1996, **16**, 61-71

[3.12] **Srivastava, V., Shukla, A., and Parameswaran, V.** Experimental Evaluation of the Dynamic Shear Strength of Adhesive-Bonded Lap Joints. *Journal of Testing and Evaluation*, 2000, **28,** 6, 438-442

[3.13] **Yokoyama, Takashi.**, **and Shimizu, Hiroshi.** Evaluation of Impact Shear Strength of Adhesive Joints with the Split Hopkinson Bar. *JSME International Journal*, 1998, **A-41,** 4, 503-509

[3.14] **Yokoyama, T., and Nakai, K.** Determination of impact tensile properties of structural epoxy adhesive butt joints using a hat-shaped specimen. *J. Phys. IV France,* 2006, **134,** 789–795

[3.15] **Adamvalli, M., and Parameswaran, V.** Dynamic strength of adhesive lap joints at high temperature. *International Journal of Adhesion and Adhesive,* 2008, 28,321–327.

[3.16] **Chen, Xuan., and Li, Yulong.** An Experimental Technique on the Dynamic Strength of Adhesively Bonded Single Lap Joints. *Journal of Adhesion Science and Technology*, 2010, **24**, 291–304

[3.17] **Raykhere, Sohan Lal., Kumar, Prashant., Singh, R.K., and Parameswaran, Venkitanarayanan.** Dynamic shear strength of adhesive joints made of metallic and composite adherents. *Materials and Design*, 2010, **31,** 2102–2109

[3.18] **Volkersen, O.** Die Niektraftverteilung in Zugbeanspruchten mit Konstanten Laschenquerschritten. *Luftfahrtforschung,* 1938**, 15,** 41–47.

[3.19] **Goland, M., and Reissner, E.** The stresses in cemented joints. *Journal of Applied Mechanics*, 1944, **11,** A17–27.

[3.20] **de Bruyne, N.A.,** The strength of glued joints. *Aircraft Eng,* 1944, **16,115**–118.

[3.21] **Hart-Smith, L.J.** Adhesive bonded single lap joints. NASA CR-112236, 1973, 1-114.

[3.22] **Tsai, M.Y., Oplinger, D.W., and Matthews, F.L.** Improved theoretical solutions for adhesive lap joints. *International Journal of Solids and Structures,* 1998, **35(12),** 1163–85.

[3.23] **Chataigner, Sylvain., Caron, Jean-Francois., Diaz, Alberto Diaz., Aubagnac, Christophe., and Benzarti, Karim.** Non-linear failure criteria for a double lap bonded joint. *International Journal of Adhesion & Adhesives*, 2010, **30**, 10–20.

[3.24] **Chen, D., and Cheng, S.** Torsional Stresses in tubular lap joints. *Int. J. Solids Structures*, 1992, **29-7**, 845-853.

[3.25] **Srinivas S.** Analysis of bonded joints. NASA TN D-7855, 1975.

[3.26] **Allman, D.J.** Theory for elastic stresses in adhesive bonded lap joints. *Quarterly Journal of Mechanics and Applied Mathematics*, 1977, **30-4**, 415-436.

[3.27]**Mortensen, F., and Thomsen, O.T.** Analysis of Adhesive Bonded Joints. *Composite Science and Technology*, 2002,**62,** 1011-1031

[3.28] **Cheng, S., Chen, D., and Shi, Y.** Analysis of adhesive bonded joints with nonidentical adherends. *Journal of Engineering Mechanics*, 1991,117, 605–623.

[3.29] **McGeorge, Dag.** Inelastic Fracture of Adhesively Bonded Overlap Joints. *Engineering Fracture Mechanics,* 2010, **77**, 1-21

[3.30] **Crocombe, A.D, and Adams, R.D.** Influence of the spew fillet and others parameters on the stress distribution in the single lap joint. *Journal of Adhesion*, 1981, **13,141**–155.

[3.31] **Oplinger, D.W.** Effect of adherend deflections in single lap joints. *International Journal of Solids and Structures,* 1994, **31,** 2565–2587.

[3.32] **Yadagiri, S., Reddy, C.P., and Reddy, T.S.** Viscoelastic analysis of adhesively bonded joints. *Computers and Structures*, 1987, **27-4,** 445-454.

[3.33] **Barker, R.M., and Hatt, F.** Analysis of bonded joints in vehicular structures. *AIAA J,* 1973, **11,** 1650–1654.

[3.34] **Adams, R.D., and Peppiatt, N.A.** Stress analysis of adhesively bonded lap joints. *Journal of Strain Analysis for Engineering Design,* **1974,** 9,185–196.

[3.35] **Harris, J.A., and Adams, R.D.** Strength prediction of bonded single lap joints by nonlinear finite element methods. *International Journal of Adhesion and Adhesives* 1984, **4**, 65-78.

[3.36] **Reddy, J.N., and Roy, S.** Nonlinear analysis of adhesively bonded joints. *International Journal of Nonlinear Mechanics,* 1988, **23**, 97-112.

[3.37] **Roy, S., and Reddy, J.N.** A finite element analysis of adhesively bonded composite joints with moisture diffusion and delayed failure. *Composites and Structures*, 1988, **29-6**, 1011-1031

[3.38] **Long, R.S.** Static strength of adhesively bonded joints. *Journal of Composite Material,* 1991, **25,391**–415.

[3.39] **Lin, C., and Lin, Y.** Finite element model of single lap adhesive joints. *International Journal of Solids and Structures,* 1993, **30, 1669**–1972

[3.40] **Carpenter, W.C.** Viscoelastic analysis of bonded connections. *Computers and Structures,* 1990, **36-6,** 1141-1152

[3.41] **Carpenter, W., and Barsoum R.** Two finite element for modeling the adhesive in bonded configurations. *Journal of Adhesion,* 1989, **30, 25**–46.

[3.42] **Pandey, P.C., Shankaragouda, H., and Singh, Arbind Kr.** Nonlinear analysis of adhesively bonded lap joints considering viscoplasticity in adhesives. *Computers and Structures.* 1999, **70,** 387–413

[3.43] **Lataillade, J. L., and Cayssials, F.** Viscoelastic Relaxations in Polyepoxide Joints Related to the Strength of Bonded Structures at Impact Rate Shear Loading. *Polymer Engineering and Science.* 1997, **37-10,** 1655-1663

[3.44] **Hadj-Ahmed, R., Foret, G., and Ehrlacher, A.** Stress analysis in adhesive joints with a multiparticle model of multilayered materials (M4). *International Journal of Adhesion & Adhesives.* 2001, **21**, 297-307

[3.45] **Challita, Georges., and Othman, Ramzi.** Finite-element analysis of SHPB tests on double-lap adhesive joints. *International Journal of Adhesion and Adhesives*. 2010, **30**, 236–244

[3.46] **Malyshev, B. M., and Salganik, R.L.** The strength of adhesive joints using the theory of cracks. *International Journal of Fracture*. 1984, **26**, 261-275.

[3.47] **Srivastava, V., Parameswaran, V., Shukla, A. and Morgan, D.** Evaluation of the dynamic strength of adhesive joints using split hopkinson pressure bar. *Recent Advances in Experimental Mechanics*, 2002, Special Technical Publication, 769-780.

[3.48] **Cook, R.D., Malkus D.S., Plesha M.E., and Witt, J.R.** Concepts and Applications of Finite Element Analysis. *Wiley India*, 2007, Fourth Edition.

[4.1]**Kolsky, H.** An investigation of the mechanical properties of materials at very high rates of loading. *Proc. Phys. Soc.*, 1949, **B-62**, 676–700.

[4.2]**Eskandari H. and Nemes J.A.**, Dynamic Testing of Composite Laminates with a Tensile Split Hopkinson Bar, *Journal of Composite Materials*, 2000, **34-24**, 260-273

[4.3]**Staab G.H. and Gilat A.,** A Direct-tension Split Hopkinson Bar for High Strain-rate Testing, *Exp Mech*, September 1991, 232-235

[4.4]**Harding, J., Wood, E. O. and Campbell, J. D.** Tensile testing of materials at impact rates of strain. *J. Mech. Engng Sci.*, 1960, **2**, 88–96

[4.5]**Harding, J. and Welsh, L. M.** A tensile testing technique for fiber-reinforced composites at impact rates of strain, *J. Mater. Sci.*, 1983, **18**, 1810–1826.

[4.6]**Hauser, F. E.** Techniques for measuring stress–strain relations at high strain rates. *Exp Mechanics*, 1966, **6**,395–402.

[4.7]**Nicholas, T.** Tensile testing of materials at high rates of strain. *Exp. Mechanics*, 1981, **21**, 177–185.

[4.8]**Lee O.S. and Kim M.S**, Dynamic material property characterization by using split Hopkinson pressure bar (SHPB) technique, *Nuclear Engineering and Design*, 2003, **226**, 119–125.

[4.9]**Al-Mouwasi M.M, Reid S.R., Deans W.F.**, The use of the split Hopkinson pressure bar techniques in high strain rate materials testing, *Proc Instn Mech Engrs* ,**211-C**, 273-292

[4.10]**Lee O.S., Kim G.H., Kim M.S., Hwang J.S.**, Dynamic Deformation Behavior of Aluminum Alloys Under High Strain Rate Compressive/Tensile Loading, *KSME International Journal*, 2003, **17 -6**, 787—795.

[4.11]**Acosta J.F., Raju K.S.**, Dispersion Effects on High Speed Tension Testing – SHPB, *Proceedings of the 3rd Annual GRASP Symposium, Wichita State University*, 2007, 39-40.

[4.12]**Lindholm, U. S. and Yeakley, L.M**. High strain-rate testing: tension and compression. *Exp Mechanics*, 1968, **8**, 1–9.

[4.13]**Mohr D, and Gray G**, M-shaped Specimen for the High-strain Rate Tensile Testing Using a Split Hopkinson Pressure Bar Apparatus, *Exp Mech* ,2007, **47**,681–692.

[4.14]**Ramesh KT.,** High strain rate and impact experiments. In: Sharp WN (ed) Handbook of experimental solid mechanics, chapter 33, Springer, 101 Philip Drive, Norwell MA 02061, 2009, USA

[4.15]**Subhash G, Ravichandran G**, Split-Hopkinson Pressure Bar Testing of Ceramics, ASM Handbook, Vol 8, *Mechanical Testing and Evaluation*, ASM Int, Materials Park OH, 2000,488–496.

[4.16]**Ravichandran G and Subhash G**; Critical appraisal of limiting strain rates for compression testing of ceramics in a split-Hopkinson pressure bar, *J. Am. Ceram. Soc.* **77**, 1994, 263–267.

[4.17]**Vecchio Kenneth S., Jiang Fengchun**, Improved Pulse Shaping to Achieve Constant Strain Rate and Stress Equilibrium in Split-Hopkinson Pressure Bar Testing, *Metallurgical and Materials Transactions A*, 2007, **38A**, 2655-2665

[4.18]**Gilat A, Schmidt T.E., Walker A.L.,** Full Field Strain Measurement in Compression and Tensile Split Hopkinson Bar Experiments, *Experimental Mechanics*, 2009, **49**,291–302